ARL-TR-7743 ● AUG 2016

US Army Research Laboratory

Adaptive Seat Energy Absorbers for Enhanced Crash Safety: Technology Demonstration

by Gregory J Hiemenz, Muthuvel Murugan, Wei Hu, Norman M Wereley, and JinHyeong Yoo

Approved for public release; distribution is unlimited.

NOTICES

Disclaimers

The findings in this report are not to be construed as an official Department of the Army position unless so designated by other authorized documents.

Citation of manufacturer's or trade names does not constitute an official endorsement or approval of the use thereof.

Destroy this report when it is no longer needed. Do not return it to the originator.

ARL-TR-7743 ● AUG 2016

US Army Research Laboratory

Adaptive Seat Energy Absorbers for Enhanced Crash Safety: Technology Demonstration

by Muthuvel Murugan and JinHyeong Yoo
Vehicle Technology Directorate, ARL

Gregory J Hiemenz
InnoVital Systems Inc., Beltsville, MD

Wei Hu and Norman M Wereley
University of Maryland, College Park, MD

Approved for public release; distribution is unlimited.

REPORT DOCUMENTATION PAGE

Form Approved
OMB No. 0704-0188

Public reporting burden for this collection of information is estimated to average 1 hour per response, including the time for reviewing instructions, searching existing data sources, gathering and maintaining the data needed, and completing and reviewing the collection information. Send comments regarding this burden estimate or any other aspect of this collection of information, including suggestions for reducing the burden, to Department of Defense, Washington Headquarters Services, Directorate for Information Operations and Reports (0704-0188), 1215 Jefferson Davis Highway, Suite 1204, Arlington, VA 22202-4302. Respondents should be aware that notwithstanding any other provision of law, no person shall be subject to any penalty for failing to comply with a collection of information if it does not display a currently valid OMB control number.
PLEASE DO NOT RETURN YOUR FORM TO THE ABOVE ADDRESS.

1. REPORT DATE *(DD-MM-YYYY)*	2. REPORT TYPE	3. DATES COVERED (From - To)
August 2016	Technical Report	10 January 2012–29 February 2016

4. TITLE AND SUBTITLE
Adaptive Seat Energy Absorbers for Enhanced Crash Safety: Technology Demonstration

5a. CONTRACT NUMBER

5b. GRANT NUMBER

5c. PROGRAM ELEMENT NUMBER

6. AUTHOR(S)
Gregory J Hiemenz, Muthuvel Murugan, Wei Hu, Norman M Wereley, and JinHyeong Yoo

5d. PROJECT NUMBER
JASPO-V-13-02

5e. TASK NUMBER

5f. WORK UNIT NUMBER

7. PERFORMING ORGANIZATION NAME(S) AND ADDRESS(ES)
US Army Research Laboratory
ATTN: RDRL VTM
Aberdeen Proving Ground, MD 21005-5066

8. PERFORMING ORGANIZATION REPORT NUMBER
ARL-TR-7743

9. SPONSORING/MONITORING AGENCY NAME(S) AND ADDRESS(ES)
Joint Aircraft Survivability Program Office
735 S Courthouse Road, Suite 1100
Arlington, VA 22204-2489

10. SPONSOR/MONITOR'S ACRONYM(S)

11. SPONSOR/MONITOR'S REPORT NUMBER(S)

12. DISTRIBUTION/AVAILABILITY STATEMENT
Approved for public release; distribution is unlimited.

13. SUPPLEMENTARY NOTES

14. ABSTRACT
This research program is intended to design, assemble, and test, both at a component and assembly level, adaptive seat energy absorber (ASEA) technology to retrofit a rotorcraft crew seat. Two adaptive energy absorber (EA) technologies were developed in this research program: 1) rotary magnetorheological EA with magnetic bias and 2) magnetostrictive friction EA. The results of the evaluation of these adaptive seat EA technologies for rotorcraft crashworthiness and safety enhancement are summarized in this report. The low speed crash dynamic sled tests conducted showed great promise for the ASEA technology, with occupant compressive lumbar loads measured to be more than 32% lower than published data for the baseline MH-60R seat with conventional EAs. Moreover, the ASEA used substantially less stroke than the baseline seat, showing that the ASEA can be much more efficient.

15. SUBJECT TERMS
adaptive seat damper, magnetorheological damper, crash safety, rotorcraft, energy absorber, occupant protection

16. SECURITY CLASSIFICATION OF:			17. LIMITATION OF ABSTRACT	18. NUMBER OF PAGES	19a. NAME OF RESPONSIBLE PERSON
a. REPORT	b. ABSTRACT	c. THIS PAGE			Muthuvel Murugan
Unclassified	Unclassified	Unclassified	UU	126	19b. TELEPHONE NUMBER (Include area code) 410-278-7903

Standard Form 298 (Rev. 8/98)
Prescribed by ANSI Std. Z39.18

Contents

List of Figures v

List of Tables ix

Acknowledgments x

Executive Summary xi

1. Introduction 1

2. FY2013 Accomplishments 1

2.1 Objective 1: Design, Fabricate, and Demonstrate MREA Device in Component-Level Testing 1

2.1.1 Task (a): MREA Simulation, Design, and Fabrication 2

2.1.2 Task (b): Component Level Testing and Refinement 22

2.2 Objective 2: Design, Fabricate, and Demonstrate MFEA Device in Component-Level Testing 28

2.2.1 Task (a): MFEA Simulation, Design, and Fabrication 28

2.2.2 Task (b): Component-Level Testing and Refinements 31

3. FY2014 Accomplishments 34

3.1 Objective 1: Conduct Seat-Occupant System-Level Modeling and Simulation to Evaluate Biodynamic Response Using Novel EAs 34

3.1.1 Task (a): System-Level Model Development 35

3.1.2 Task (b): Adaptive Control Algorithm and System-Level Simulations and Refinements 39

3.2 Objective 2: Design and Fabricate a Test Seat for Integrating Novel EAs 43

3.2.1 Task (a): Seat Design 43

3.2.2 Task (b): Seat Fabrication 51

4 FY2015 Accomplishments 54

4.1 Objective 1: Integration of Adaptive Control 54

4.1.1 Task (a): Performance Predictions from System-Level Modeling and Simulation 54
4.1.2 Task (b): Control Electronics Development 65
4.2 Objective 2: Full-Scale Dynamic Testing 68
4.3 Objective 3: Final Report Preparation and Completion 78

5. Conclusions and Recommendations 78

6. References 80

Appendix A. Test Plan 83

Appendix B. Floor Mounting Detail 95

Appendix C. Sensor, Data Type, and Corresponding Injury Assessment Criteria 99

Appendix D. Anthropomorphic Test Device Total Weight Requirements 101

Appendix E. High-Speed Sled Test Checklist 103

Appendix F. Crash Pulse Validation Table 107

List of Symbols, Abbreviations, and Acronyms 109

Distribution List 111

List of Figures

Fig. 1 SDOF MR seat suspension system 4

Fig. 2 Fail-safe MREA performance, 50th male, F_{BY} = 6.1 kN, C = 500 N-s/m, G_L = 51 g's 5

Fig. 3 Fail-safe MREA performance, 50th male, F_{BY} = 4.0 kN, C = 1,100 N-s/m, G_L = 51 g's 5

Fig. 4 Controllable MREA performance, 95th male, F_{TY} = 9.1 kN, C = 1,100 N-s/m, G_L = 51 g's 6

Fig. 5 Controllable MREA performance, 5th female, F_{TY} = 4.8 kN, C = 500 N-s/m, G_L = 51 g's 7

Fig. 6 Low-acceleration impact performance of MREA: 95th male, G_L = 25 g's, C = 500 N-s/m, F_{Ty} = 3.5 kN (left); 5th female, G_L = 35 g's, C = 1,100 N-s/m, F_{Ty} = 0.78 kN (right) 7

Fig. 7 Schematics of fail-safe MREA 9

Fig. 8 Magnetic field analysis using ANSYS 11

Fig. 9 Schematic of a multivane MREA design; 4-vane, 8-flow-gap configuration 12

Fig. 10 MREA weight as a function of number of vanes and pinion diameter for a single MREA configuration 13

Fig. 11 Magnetic field results (A/m) using ANSYS for a 4-vane MREA 14

Fig. 12 Magnetic field strength at flow gaps 15

Fig. 13 Performance comparison between analytical and FEM analysis for a 4-vane MREA 15

Fig. 14 Single-MREA configuration 17

Fig. 15 Two-MREA configuration 17

Fig. 16 Lightweight rotary-vane MREA design 20

Fig 17 Complete MREA with rack and pinion system 21

Fig. 18 MREA and motion conversion components 21

Fig. 19 Fully assembled MREA 22

Fig. 20 MREA coupled to DC motor for pure rotation testing 23

Fig. 21 MREA system in MTS system for testing with motion conversion 23

Fig. 22 Torque vs. time as a function of applied current to the MREA from rotation tests 24

Fig. 23 MREA yield force as a function of applied current from rotation tests 24

Fig. 24 Force vs. displacement from MTS tests as a function of applied current 25
Fig. 25 Force vs. velocity from MTS tests as a function of applied current 25
Fig. 26 MREA yield force as a function of applied current for both rotation and MTS tests 25
Fig. 27 MREA viscous damping as a function of applied current for both rotation and MTS tests 26
Fig. 28 SDOF dynamic simulations showing that lower MREA yield force increases stroke by less than 1.0 inch for the 95th male 26
Fig. 29 SDOF dynamic simulations showing that the lower MREA yield force increases stroke by 1.9 inches for the 50th male in fail-safe mode 27
Fig. 30 Effect of modifying permanent magnet dimensions: increasing thickness from 0.07 to 0.09 inch yields modest increase in yield force; decreasing ID from 2.5 to 2.25 inches yields less than 1-kN increase in yield force 27
Fig. 31 Friction damper schematic diagram for normal force calculation 30
Fig. 32 Simulation result of the normal force vs. Terfenol-D diameter 30
Fig. 33 Friction test rig for MFEA development 32
Fig. 34 Friction test results for aluminum-to-aluminum friction material 33
Fig. 35 Friction test results for steel-to-steel friction material 33
Fig. 36 Friction coefficients for aluminum-to-aluminum and steel-to-steel friction material along the rotation speed of measurement 33
Fig. 37 Adams-MatLab/Simulink co-simulation control flow diagram for end-stop control and a control simulation result 34
Fig. 38 Occupant kinematics from finite element analysis (LS-DYNA) 35
Fig. 39 Lumped-parameter human body model 36
Fig. 40 Coupling between rotorcraft floor structure and seat-occupant model 37
Fig. 41 Comparison of the vertical STH vibration TR characteristics computed from the proposed human body model with those upper and lower limits of experimental data from Boileau and Rakheja 38
Fig. 42 Comparison of the vertical DPM IM characteristics computed from the proposed human body model with those upper and lower limits of experimental data from Boileau and Rakheja 39
Fig. 43 Simulink control flow diagram for end-stop control 40
Fig. 44 A lumped-parameter seat-occupant model 41
Fig. 45 Baseline vs. MREA with control: 5th percentile 42
Fig. 46 Baseline vs. MREA with control: 50th percentile 42
Fig. 47 Baseline vs. MREA with control: 95th percentile 43

Fig. 48 MH-60R seat manufactured by BAE Protection Systems (formerly Simula, Inc.), front isometric view 45
Fig. 49 MH-60R seat rear view, highlighting EA load path 46
Fig. 50 MH-60R seat showing preliminary MREA integration....47
Fig. 51 Detailed design for integrating MREA into MH-60R seat 48
Fig. 52 FEM analysis of EA supporting structures 49
Fig. 53 FEM analysis of gear rack and its support....49
Fig. 54 Simplified JASP seat structure for FEM evaluation....50
Fig. 55 FEM analysis of JASP seat structure....51
Fig. 56 Manufactured seat components for integration MREA....52
Fig. 57 Iron bird test seat with MREA: lower position....53
Fig. 58 Iron bird test seat with MREA: high position....53
Fig. 59 Model of passive seat damper....55
Fig. 60 Impulse response of seat: 1) before optimization (k_s = 53 kN/m, b_s =1.1 kNm/s) (blue curve) and 2) after optimization (k_s =4.98 kN/m, b_s =0.846 kNm/s) (red curve)....55
Fig. 61 Adams-MatLab/Simulink co-simulation result comparison for end-stop control and optimal control....56
Fig. 62 Schematic drawing of hybrid actuator-based energy....57
Fig. 63 Piston displacement of output shaft driven by 2-inch-long Terfenol rod at 200 Hz....59
Fig. 64 Behavior of electrohydraulic EA using 200-Hz pumping frequency and 50-psi accumulator pressure....60
Fig. 65 Block force variation as a function of applied field....61
Fig. 66 Calculated block force with actuation piston of 3 inches in diameter....61
Fig. 67 Effect of pumping frequency on block force 61
Fig. 68 Effect of accumulator pressure on block force 62
Fig. 69 Adams-MatLab/Simulink co-simulation control flow diagram for optimal control and a control simulation result 63
Fig. 70 Finite element seat-occupant model....64
Fig. 71 Adaptive EA load-stroke profile for modeling (for 50th percentile male, the fixed-load level EA is adjusted using permanent magnet design in the rotary FSMREA developed for this project) 64
Fig. 72 Dynamic seat stroke and lumbar force profiles during crash simulation (for passive and adaptive EA cases) 65
Fig. 73 PCB for integrated control electronics....66

Fig. 74 Exploded view of integrated control electronics mechanical packaging 66
Fig. 75 PCB integrated into mechanical packaging 67
Fig. 76 Control algorithm flowchart 67
Fig. 77 Pretest photo for test no. 1, 50th percentile male occupant and 21 ft/s crash velocity 69
Fig. 78 Posttest photo for test no. 1, 50th percentile male occupant and 21 ft/s crash velocity 69
Fig. 79 Lumbar compressive load for test no. 1, 50th percentile male and 21 ft/s crash velocity 70
Fig. 80 Seat stroke for test no. 1, 50th percentile male and 21 ft/s crash velocity 70
Fig. 81 Pretest photo for test no. 2, 50th percentile male occupant and 34 ft/s crash velocity 71
Fig. 82 Posttest photo for test no. 2, 50th percentile male occupant and 34 ft/s crash velocity 72
Fig. 83 Lumbar compressive load for test no. 2, 50th percentile male and 34 ft/s crash velocity 72
Fig. 84 Seat stroke for test no. 2, 50th percentile male and 34 ft/s crash velocity 73
Fig. 85 Pretest photo for test no. 3, 50th percentile male occupant and 42 ft/s crash velocity 74
Fig. 86 Posttest photo for test no. 3, 50th percentile male occupant and 42 ft/s crash velocity 74
Fig. 87 Posttest photo for test no. 3 showing top crossbar broken off of seat back 75
Fig. 88 Posttest photo for test no. 3 showing top crossbar and headrest completely free from seat back 75
Fig. 89 Pretest photo for test no. 4, 50th percentile male occupant and 42 ft/s crash velocity 76
Fig. 90 Posttest photo for test no.4, 50th percentile male occupant and 42 ft/s crash velocity 77
Fig. 91 Posttest photo for test no. 4 showing broken seat pan 77
Fig. 92 Posttest photo for test no. 4 showing close-up of broken seat pan 78

Fig. A-1 FSMREA with integrated pinion 85
Fig. A-2 Linear-to-rotary gearing assembly 85
Fig. A-3 JASP seat configuration 86
Fig. A-4 FSMREA control electronics box 87
Fig. A-5 Seat attachment to mounting tracks 88
Fig. A-6 High-speed testing sensor configuration 89
Fig. A-7 Dynamic test parameters 91
Fig. B-1 T-rail tracks (units in inches): Quantity 2 96
Fig. B-2 U-brackets (units in inches): Quantity 4 97

List of Tables

Table 1 Occupant weight information 3
Table 2 Total, F_{Ty}, bias, F_{By}, and controllable, F_y, yield force requirements per MREA 5
Table 3 Total, F_{Ty}, bias, F_{By}, and controllable, F_y, yield force requirements per MREA at low-acceleration impacts 8
Table 4 Initial MREA design parameters 10
Table 5 Pinion gear design results. Material: 17-4PH stainless steel (σ_y = 183 ksi) 18
Table 6 Rack gear design results. Material: titanium (σ_y = 120 ksi) 18
Table 7 Total estimated MREA design weights 19
Table 8 Terfenol-D physical properties 29
Table 9 Candidates of friction materials 31
Table 10 Estimated segment mass and inertial properties 36
Table 11 Stiffness and damping coefficients of the human body segments 37
Table 12 Control parameters 40
Table A-1 Dynamic test matrix and requirements 91

Acknowledgments

This work was performed under a research funding awarded by the Joint Aircraft Survivability Program Office (Project Number: JASP# V-13-02). The authors thank Capt Ken Branham, Deputy Program Manager, for supporting this project. The authors also thank Dr Al Tabiei, University of Cincinnati, for providing guidance on the finite-element-based seat-occupant model development.

Executive Summary

This final report documents the technical progress on the Adaptive Seat Energy Absorbers for Enhanced Crash Safety program sponsored by the Joint Aircraft Survivability Program Office, project number V-13-02. The period of performance of this effort was from 1 October 2012 through 29 February 2016.

This research program is intended to design, assemble, and test, both at a component and assembly level, adaptive seat energy absorber (ASEA) technology to retrofit a rotorcraft crew seat. The final product of this program was intended to be a prototype ASEA system that has been evaluated for enhanced crash safety performance. In the first year of the program, 2 ASEA technologies, a magnetorheological energy absorber (MREA) and magnetostrictive friction energy absorber were designed and evaluated at a component level. Only the MREA was found to meet program objectives and was therefore down-selected for the remainder of the program. In the second year of the program, the MREA was successfully retrofitted into an MH-60R seat. In parallel with this, modeling and simulation was conducted to evaluate adaptive control algorithms. Then, in the third year of the program, the MREA was integrated with control electronics for enacting adaptive control algorithms and further simulations were conducted. Full-scale dynamic crash testing was planned to evaluate the ASEA technology across a range of crash velocities and occupant weights. The first 2 tests conducted showed great promise for the ASEA technology, with compressive lumbar loads measured to be more than 32% lower than published data for the baseline MH-60R seat with conventional energy absorbers. Moreover, the ASEA used substantially less stroke than the baseline seat, showing that the ASEA can be much more efficient. Unfortunately, however, structural failures on the seat prevented the full matrix of dynamic tests from being conducted.

Given the promise shown in these initial dynamic tests and the fact that further tuning of the adaptive control algorithm will likely further improve performance, the project team recommends continuation of investment into the ASEA technology. Seat integration and structural issues can be addressed and new seat hardware can be purchased such that the testing series can be completed. As an alternative, a simplified single-degree-of-freedom test setup may be constructed to evaluate the ASEA technology in a more cost-effective manner.

INTENTIONALLY LEFT BLANK.

1. Introduction

This final report documents the technical progress on the Adaptive Seat Energy Absorbers for Enhanced Crash Safety program sponsored by the Joint Aircraft Survivability Program Office (JASPO), project number V-13-02. The period of performance of this effort was from 1 October 2012 through 29 February 2016.

This research program intended to design, assemble, and test, both at a component and assembly level, adaptive seat energy absorber (ASEA) technology to retrofit a rotorcraft crew seat. The final product of this program was intended to be a prototype ASEA system that has been evaluated for enhanced crash safety performance.

Sections 1–3 document technical accomplishments against objectives and technical tasking within the statement of work (SOW) for each fiscal year (FY) of the program.

2. FY2013 Accomplishments

The objective of the FY13 SOW was to evaluate and demonstrate 2 "smart" energy absorber (EA) technologies for enhanced crash safety:

1) Rotary magnetorheological energy absorber (MREA) with magnetic bias
2) Magnetostrictive friction energy absorber (MFEA).

Metrics for success for both devices were to achieve adjustable force levels in the target range of 2,000–3,500 lb. Techno-Sciences, Inc. (now InnoVital Systems, Inc.), was responsible for the design of the MREA (Objective 1), while the US Army Research Laboratory's Vehicle Technology Directorate (ARL-VTD) was responsible for the design in MFEA (Objective 2). As is discussed later, target metrics for Objective 1 were successfully met with an MREA device that was 58% lighter than previous MREA designs, but Objective 2 was unsuccessful.

2.1 Objective 1: Design, Fabricate, and Demonstrate MREA Device in Component-Level Testing

Under this first objective, the project team conducted 1) preliminary design analysis, 2) detailed MREA design analysis including trade studies for various MREA configurations, and 3) rotary-to-linear-motion convertors. The project team has selected and developed a final MREA design based on its merits. The selected

MREA design development was completed and details parts drawings were generated. All parts for the complete MREA design were manufactured. The details of these accomplishments are discussed in the next sections.

2.1.1 Task (a): MREA Simulation, Design, and Fabrication

2.1.1.1 MREA Preliminary Design

This task focused on determination of MREA design parameters required to meet crash safety performance goals. These include force levels for off- and on-state as well as geometric constraints. In addition, the MREA design incorporates one or more permanent magnets to create a bias magnetic field to provide a baseline fail-safe operating condition for the 50th male occupant in case of power failure. The project team conducted preliminary design and analyses to evaluate MREA design options.

The 2 key goals of the MREA system design are to provide 1) a fail-safe capability to protect the 50th male occupant in case of power failure (off-state condition) and 2) the required protection for the full range of occupants at normal operating condition for a triangular input deceleration pulse of 51 g's representing an impact velocity of 42 ft/s.[1] A third goal of the MREA design is to provide optimal protection to the occupant (i.e., using full stroke and minimizing load transmitted to occupant) in less severe crashes. The stroking load of current passive EAs is tuned for the maximum expected shock level, and thus can only stroke and provide occupant protection when this tuned threshold is reached. However, MREAs can automatically adapt the stroking load to the input shock level and minimize or eliminate possible occupant injuries at all crash impact velocities.

To begin, the project team evaluated the occupant weights to determine the maximum and minimum limit loads required for an acceptable seat energy absorption system. Earlier studies relating helicopter crew seat performance to tolerance data and cadaveric testing have shown that a seat/occupant system deceleration limit, G_L, of 14.5 g's was found to keep the load duration in the humanly tolerable range.[2] This means that to provide sufficient protection to the occupant, the energy absorbing system would stroke at 14.5 times the occupied effective seat weight for a typical triangular input pulse with a peak deceleration G_M. Further, per MIL-S-58095A,[1] the acceleration measured at the occupied seat should not exceed 23 g's for more than 25 ms for a minimum acceptable stroking seat design. These 2 conditions were used as the basis for designing the current MREA. The occupant weights used for this analysis are shown in Table 1.

Table 1 Occupant weight information

Occupant	Occupant weight (lb)	Equipment weight (lb)	Iron-bird seat weight (lb)	Available stroke (inches)
5th female	113	. . .	85	15
50th male	180	40	85	14
95th male	230	40	85	12

The project team planned to provide the fail-safe operational requirement by incorporating one or more permanent magnets into the MREA design. The permanent magnets create a baseline-fixed bias magnetic field to provide a baseline level of performance for a fail-safe operating condition in an event of power interruption to the MREA. The controllable magnetic field is provided by an electromagnetic circuit incorporated in the MREA. This circuit generates a controllable magnetic field, which, depending on the polarity of the field generated, can either boost or reduce the baseline magnetic field as required. This design approach has 2 main advantages:

1) The stroking load can be both decreased and increased from the baseline level to handle lower-weight occupants and lower-energy impacts when the coil is polarized to negate the effect of the permanent magnet, and handle higher-weight occupants and higher-energy impact energies when polarized to increase its effect;

2) Due to the presence of a baseline magnetic bias that provides a majority of the energy attenuation requirement, weight savings can be achieved due to a smaller electromagnetic coil and bobbin design, which accounts for a significant portion of weight in the current MREA designs.

The first step in designing the new MREA was establishing the baseline bias force required for the fail-safe operating mode. This analysis involves designing a fail-safe MREA system that would stroke at 14.5 times the effective occupied seat weight to attenuate peak floor deceleration pulse per the standard crash design guidelines[3] and use the available stroke as well. To establish MREA design criteria, a single-degree-of-freedom (SDOF) magnetorheological (MR) seat suspension model was constructed (Fig. 1). The equation of motion for this SDOF system can be expressed as

$$m\ddot{x} + C\dot{x} + F_{MR} = -m\ddot{z}, \tag{1}$$

where m is the effective occupied seat mass, C is internal damping such as friction (assumed zero in this investigation), x is the relative motion between seat and floor (or piston motion), and z is the absolute motion of the cockpit floor. F_{MR} is the total dissipated force contribution by the MREA and is given by

$$F_{MR} = C_p\dot{x} + F_{Ty}sign(\dot{x})$$
$$= C_p\dot{x} + (F_{BY} + F_y)sign(\dot{x}) \,, \quad (2)$$

where F_{Ty} is the total yield force, F_{By} is the bias yield force, F_y is the controllable yield force, and C_p is the postyield viscous damping. This behavior resembles a combination of a viscous and Coulomb friction damping.

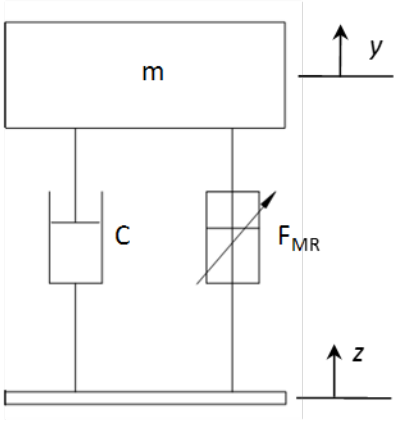

Fig. 1 SDOF MR seat suspension system

The total bias MREA force, F_{BMR}, at off-state condition is a combination of the bias yield force, F_{By}, and the viscous component given by rewriting Eq. 2 as follows:

$$F_{BMR} = C_p\dot{x} + F_{By} \,. \quad (3)$$

The fail-safe analysis was conducted for varying damping coefficients, C_p, ranging from 500 to 1,100 N-s/m. The simulation was performed for a high-speed seat qualification test requirement (42 ft/s vertical sink rate, G_L = 51 g's, t_m = 0.051 s).[2] In addition, this and all subsequent analyses were conducted for a pair of MREAs to be used to provide optimal shock mitigation. Typical examples are shown in Figs. 2 and 3. The limit loads in the figures represent the stroking load at 14.5 g's. The figures show that, at lower damping coefficients, the required bias yield force is higher than that with higher damping coefficient. This is due to the high viscous force contribution present as the damping coefficient is increased. Table 2 shows the tabulated bias force requirements for various damping coefficients.

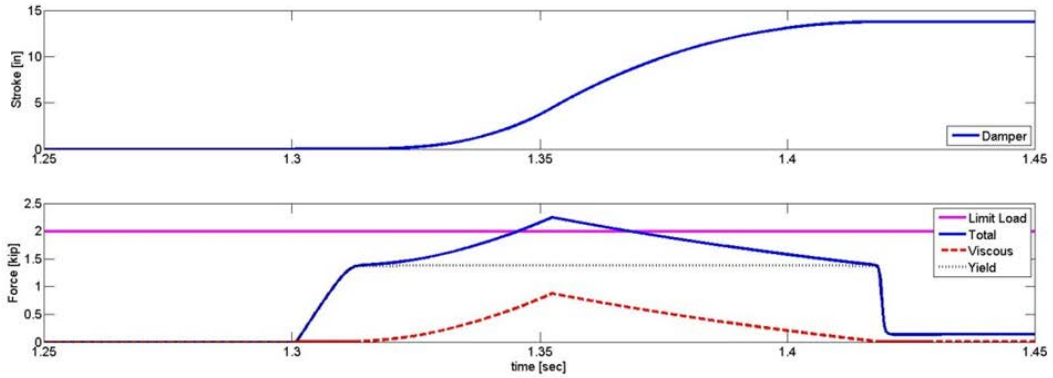

Fig. 2 Fail-safe MREA performance, 50th male, F_{BY} = 6.1 kN, C = 500 N-s/m, G_L = 51 g's

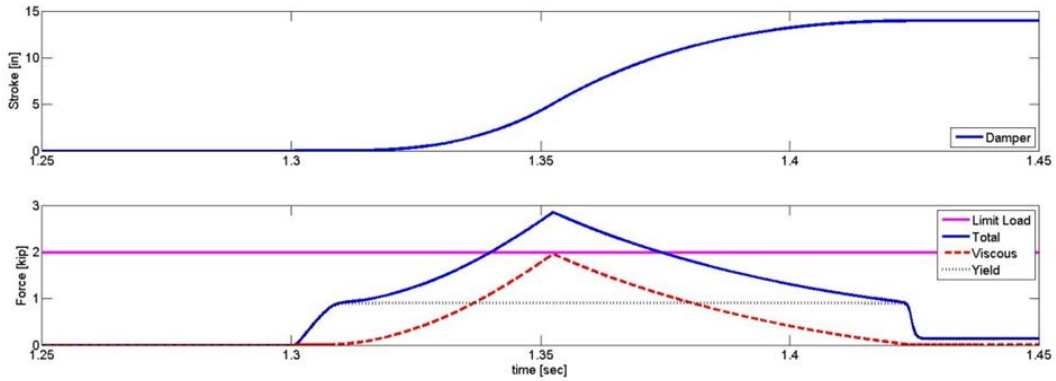

Fig. 3 Fail-safe MREA performance, 50th male, F_{BY} = 4.0 kN, C = 1,100 N-s/m, G_L = 51 g's

Table 2 Total, F_{Ty}, bias, F_{By}, and controllable, F_y, yield force requirements per MREA

C (N-s/m)	50th male			95th male	
	Bias, F_{By} (kN)	F_{Ty} (kN)	F_y (kN)	F_{Ty} (kN)	F_y (kN)
500	6.1	9.4	+3.3	4.8	–1.3
700	5.4	9.3	+3.9	4.5	–0.9
900	4.7	9.2	+4.5	4.0	–0.7
1,100	4.0	9.1	+5.1	3.0	–1.0

Once the bias yield force was established for the fail-safe operation, the next task was to determine the controllable yield force requirements for the 5th female (lightest) and 95th male (heaviest) occupants. The MREA is designed to adapt to ranging occupant weights. Depending of the occupant effective mass, the total yield force, F_{Ty}, can be calculated as follows:

$$F_{Ty} = F_{By} + F_y = F_L - F_v, \quad such\ that, \quad F_T \leq F_L, \tag{4}$$

where F_v is the contribution from viscous effect. In Eq. 4, F_L is the limit load or maximum desired stroking load for the occupant weight. Using Eq. 4, the controller modulates the MREA yield force such that the total transmitted force, F_T, does not exceed the limit load, F_L.

The design analysis was conducted for the lightest and heaviest occupants, and typical examples are shown in Figs. 4 and 5. The plots show that the MREA can provide optimal crash attenuation for both lightest and heaviest occupants, and for those in between. All tabulated results for the various damping coefficients considered for the MREA design are shown in Table 2. In the table, a positive (+) controllable yield force represents the additional yield force generated by the electromagnetic coil on top of the bias, and a negative (–) controllable yield force represents the reduction in the yield force obtained by negating the effects of the permanent magnet using the electromagnetic coil

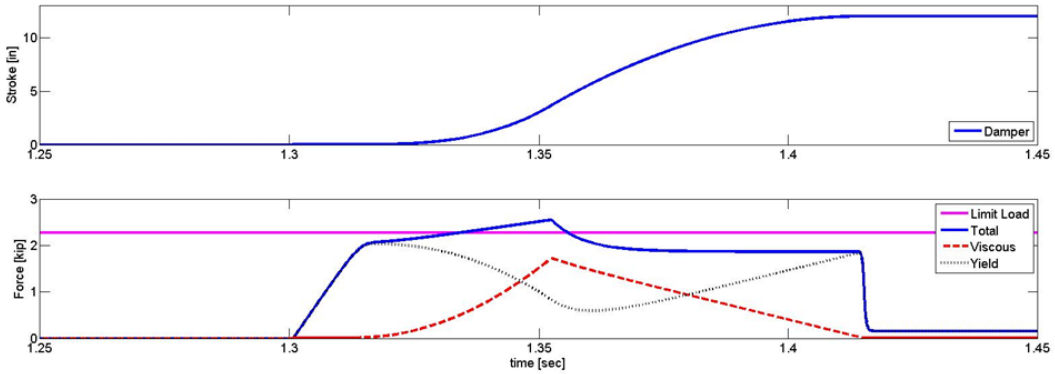

Fig. 4 Controllable MREA performance, 95th male, F_{TY} = 9.1 kN, C = 1,100 N-s/m, G_L = 51 g's

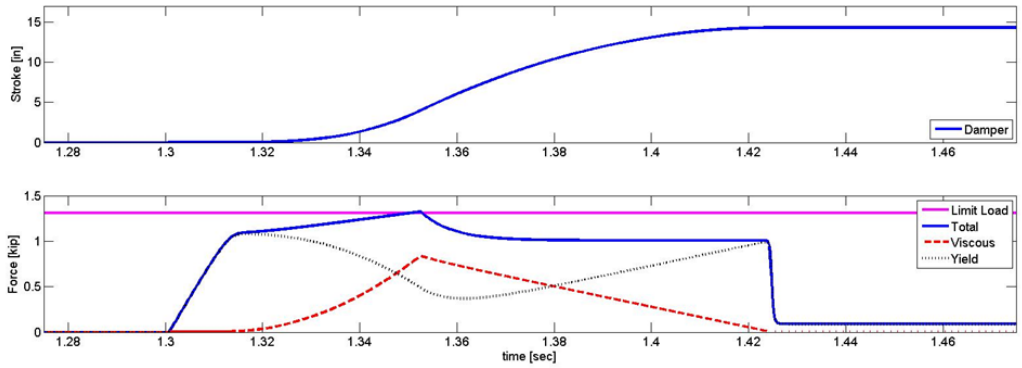

Fig. 5 Controllable MREA performance, 5th female, F_{TY} = 4.8 kN, C = 500 N-s/m, G_L = 51 g's

Once the bias and controllable yield forces were established for the range of occupants considered, the next step was determining yield force requirements for shock levels for lower-impact velocities. To that effect, 2 low-impact velocities of 20 and 29 ft/s, corresponding to peak deceleration values of 25 and 35 g's, respectively, were selected for consideration. Typical simulation results are shown in Fig. 6. The plots show that the MREA was able to significantly reduce crash severity of low-acceleration impacts, which in contrast would not have been possible with a passive EA. The tabulated results for the range of damping coefficients considered are shown in Table 3. The figures and table show that by adjusting the controllable yield force to strengthen or weaken the bias yield force based on occupant weight and crash severity, the MREA would be capable of attenuating crash severity and providing optimum protection.

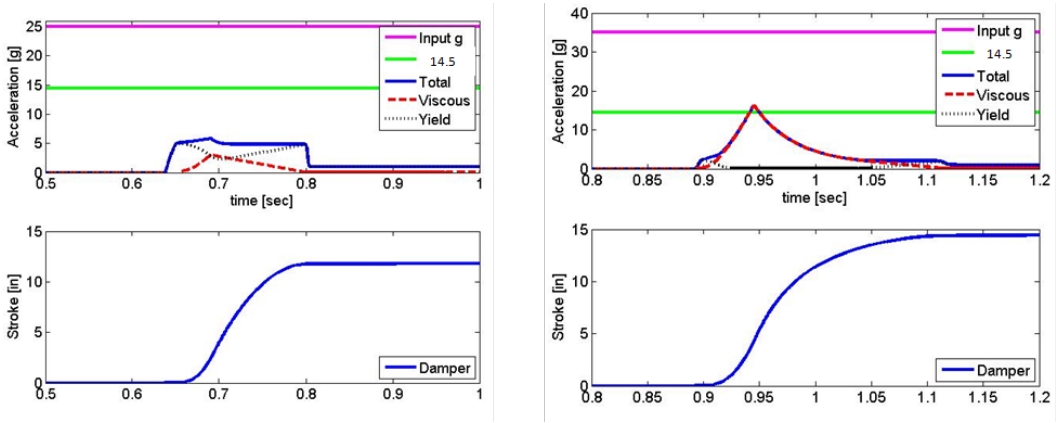

Fig. 6 Low-acceleration impact performance of MREA: 95th male, G_L = 25 g's, C = 500 N-s/m, F_{Ty} = 3.5 kN (left); 5th female, G_L = 35 g's, C = 1,100 N-s/m, F_{Ty} = 0.78 kN (right)

Table 3 Total, F_{Ty}, bias, F_{By}, and controllable, F_y, yield force requirements per MREA at low-acceleration impacts

C (N-s/m)	F_{By} (kN)	Input-g's	95th male		5th female	
			F_{Ty} (kN)	F_y (kN)	F_{Ty} (kN)	F_y (kN)
500	6.1	25	3.5	–2.6	1.7	–4.4
		35	5.2	–0.9	2.8	–3.3
700	5.4	25	3.5	–1.9	1.3	–4.1
		35	5.4	0.0	2.5	–2.9
900	4.7	25	3.4	–1.3	0.8	–3.9
		35	5.4	+0.7	1.6	–3.1
1,100	4.0	25	3.2	-0.8	0.4	–3.6
		35	5.3	+1.3	0.9	–3.1

From these simulation results, the MREA design with a damping coefficient of 900 N-s/m was selected for further evaluation. This selection was based on 2 main reasons: 1) lower-damping coefficient requires high-yield force, which will need a larger magnetic circuit design, which leads to a heavier MREA; and 2) even though higher damping requires a lower-yield force, it will negatively affect the MREA performance, especially in fail-safe mode, due to the high viscous force component present, which might result in a more-than-desired impact load transmitted to the occupant.

2.1.1.2 MREA Design Analysis

The MREA design incorporates a number of permanent magnets to generate a bias magnetic field to provide a baseline level of performance for a fail-safe operating condition where no power is supplied to the MREA. This MREA design serves 3 purposes: 1) it automatically adapts to occupant weight and crash severity and minimizes occupant injury during a crash event, 2) it incorporates a fail-safe mechanism that provides required baseline crash protection to a 50th percentile male occupant to current full-scale crash design requirements (MIL-S-58095A[1]), and 3) the presence of a bias magnetic field helps reduce the MREA design weight due to smaller electromagnetic coil and bobbin design, which accounts for a significant portion of MREA weight.

The basic design of the rotary-vane MREA design consists of a magnetic coil bobbin that is seated in the center of a cylindrical fluid chamber. Between the bobbin and cylinder wall is a cup-shaped rotary vane. As the rotary vane rotates due to applied torque, the MR fluid in the double-faced gap between the vane and the cylinder wall and bobbin, respectively, is sheared and flow is induced. Since the shear stress of the MR fluid is dependent of a magnetic field, the output torque of the rotary-vane MREA can be controlled by energizing coils in the bobbin. To initially create the baseline energy attenuation required one or more permanent

magnets are incorporated into the MREA bobbin design (Fig. 7). These permanent magnets will generate a constant baseline (fail-safe) magnetic field that can be strengthened or weakened as needed using a relatively smaller electromagnetic coil design.

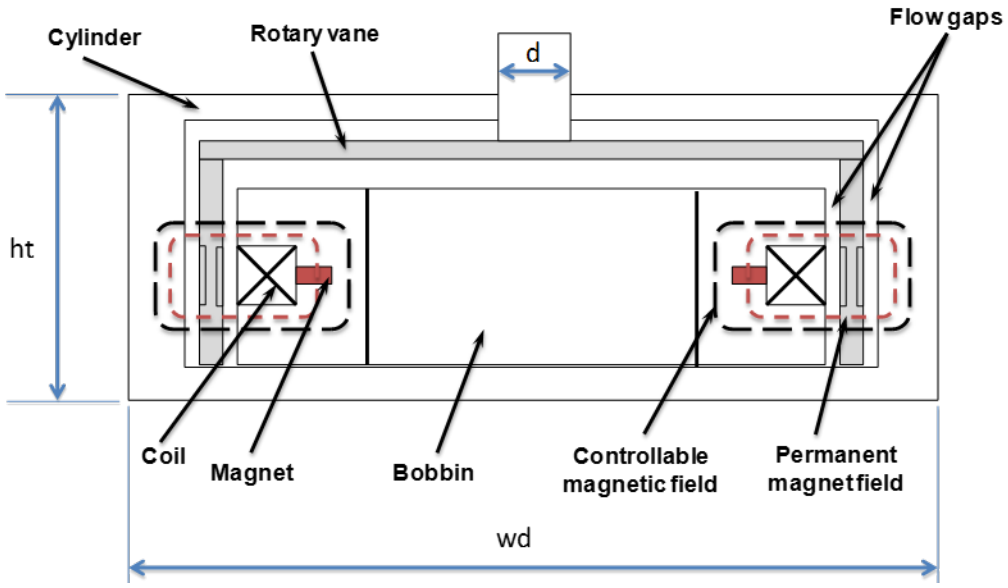

Fig. 7 Schematics of fail-safe MREA

The project team initially considered a single rotary-vane, double flow-gap MREA as shown in Fig. 7. For this design, 2 options were considered: a single MREA per seat option and a 2-MREA per seat option. For a solely MR (nonhybrid) system, the maximum total yield force of the MREA device would need to be approximately 9.2 kN (2,070 lb), for 2 MREAs per seat, and 18.4 kN (4,140 lb) for a single MREA per seat. This corresponds roughly to 14.5G times the effective maximum occupied seat mass, as discussed previously. The seat is assumed to stroke 305 mm (12 inches) in the lowest position (for the tallest occupant) and 381 mm (15 inches) in the highest position (for the shortest occupant). As such, the MREA should be able to account for 16 inches of seat stroke without reaching end-stop. The MR fluid used in this evaluation was MRF-140 manufactured by Lord Corp, due to its high-yield stress. Using design analyses, the project team estimated the MREA size and weight for each design configuration as a function of the maximum yield force (Table 4). These estimates do not include associated accessories, such as motion converters. The table data show that in terms of both size and weight, the single MREA per seat option avails a better option. The total estimated weight for a pair of MREAs is around 8 kg (18 lb), while for single MREA configuration, the total MREA weight is 6 kg (13 lb), a 25% weight savings. Further, a 2-MREA system would require 2 sets of motion converter mechanism, which could further add to the weight penalty.

Table 4 Initial MREA design parameters

Option	Diameter	Height	Approx. weight
Single MREA	203 mm (8 inches)	38 mm (1.5 inches)	4 kg (9 lb)
Two MREAs	305 mm (12 inches)	38 mm (1.5 inches)	6 kg (13 lb)

Preliminary magnetic field analysis was also conducted using ANSYS software and the design variables are iteratively modified based on the finite element method (FEM) results. The magnetic flux distribution obtained from the FEM analysis is shown in Fig. 8. The analyses were conducted at 3 operating conditions: baseline (or power-off), boosted or strengthened field, and reduced or weakened field conditions. Recall that the MREA contains a static bobbin, which consists of the magnetic circuit with a coil and a permanent magnet. In the baseline or power-off condition, only the permanent magnet generates a magnetic field, which creates an MR effect that provides the fail-safe energy absorption (Fig. 8a). When current is applied to the magnetic coil, the resulting magnetic field, depending on the polarity of the applied current in the coil, will strengthen (Fig. 8b) or weaken (Fig. 8c) the magnetic field of the permanent magnets in the active MR flow gap as required, thus respectively increasing or decreasing the energy absorption force. Figure 8 clearly illustrates how the magnetic field in the flow gaps changes depending on the applied field.

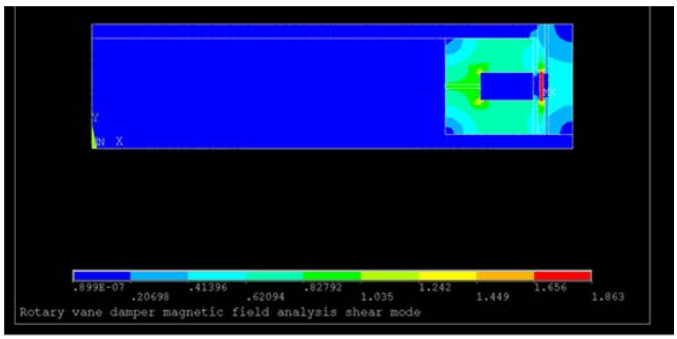

a) Baseline

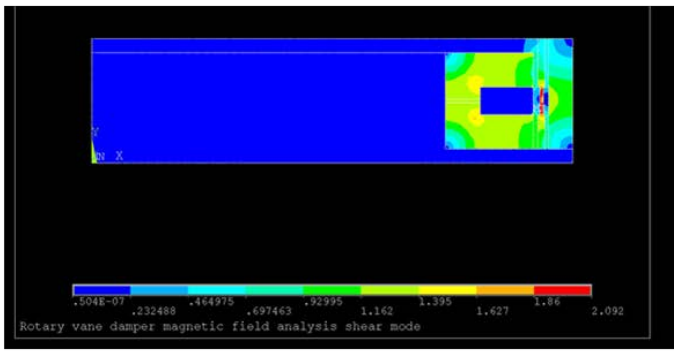

b) Strengthened field

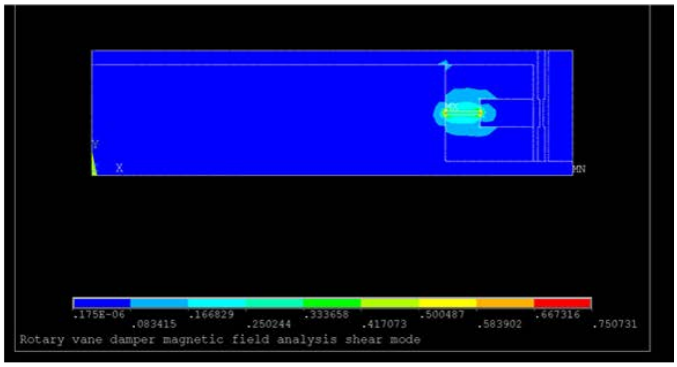

c) Weakened field

Fig. 8 Magnetic field analysis using ANSYS

The project team conducted a more detailed weight analysis and investigated ways to potentially further reduce the weight of the MREA. In this task, the effects of having a multiple-concentric rotary vane structure is investigated for weight optimization without jeopardizing expected MREA performance. A schematic of a multivane MREA is shown in Fig. 9. The figure shows an MREA with 4 rotary vanes, which are made up of 4 concentric cylinders that are all attached to the drive shaft or pinion. At the same time, there are 3 stator vanes that are fixed to the lower plate, each placed between the rotary valves, thus dividing the space between consecutive rotary vanes into 2 flow gaps. There are 2 additional flow gaps created;

one is between the cylindrical body and the outermost rotary vane, and the second one is between the bobbin and the innermost rotary vane. Thus, the total number of flow gaps equals twice the number of the rotary vanes. For the multivane MREA shown in Fig. 9, there are 4 rotary vanes, thus 8 flow gaps. Further, the effects of varying the diameter of the pinion and number of MREAs (single or double) were also investigated.

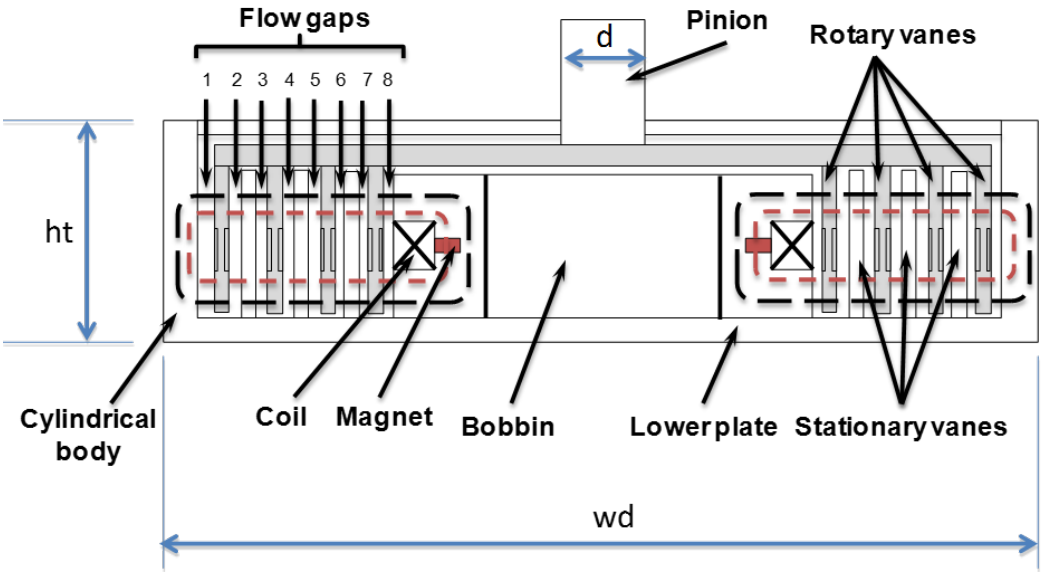

Fig. 9 Schematic of a multivane MREA design; 4-vane, 8-flow-gap configuration

The weight optimization results for a single MREA configuration with pinion diameters of 38 mm (1.5 inches), 35 mm (1.375 inches), and 25 mm (1 inches) are shown in Fig. 10. The figure shows that for a fixed pinion diameter, the weight, as well as the overall size of the MREA, shows a significant reduction as the number of vanes incorporated increases. For instance, for a pinion diameter of 35 mm (1.375 inches), the calculated minimum weight of the MREA for a single-vane MREA is about 9 kg (20 lb) with a diameter of 279 mm (11 inches), while for a 4-vane MREA, its weight would be 5.2 kg (11.5 lb) with a diameter of about 152 mm (6 inches). This shows there is a 42% weight reduction as the design changes from a single-vane to a 4-vane MREA design. As the diameter of the pinion is decreased, the overall weight of the MREA tends to decrease as well. For a 4-vane design, the minimum calculated weight of the MREA for the 3 selected pinion diameters of 38 mm (1.5 inches), 35 mm (1.375 inches), and 25 mm (1 inch) are expected to be 5.5 kg (12 lb), 5.2 kg (11.5 kg), and 4.5 kg (10 lb), respectively. This result shows that the design with a 25-mm (1-inch) pinion diameter gives the lightest MREA configuration.

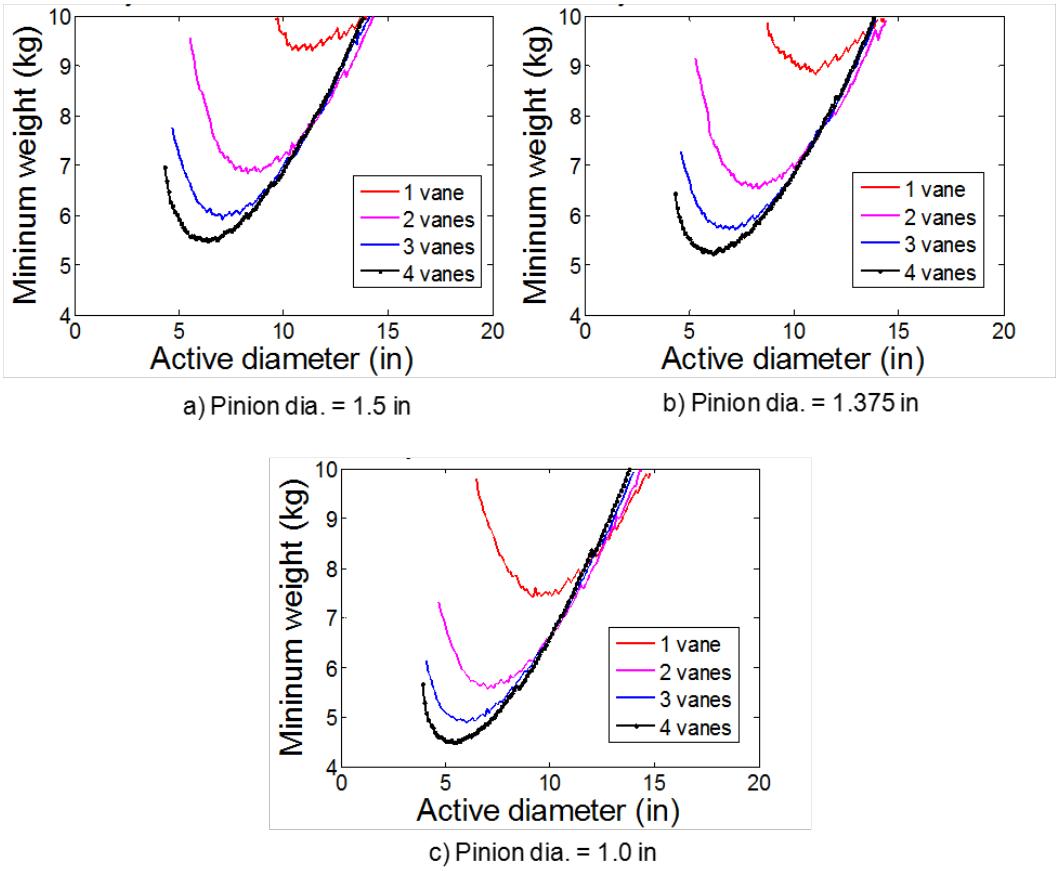

Fig. 10 MREA weight as a function of number of vanes and pinion diameter for a single MREA configuration

Magnetic field analysis was also conducted using ANSYS software for the selected MREA design. The magnetic flux distribution obtained from the FEM analysis is shown in Fig. 11. As before, these analyses were done at 3 operating conditions: baseline (or power-off), boosted or strengthened field, and reduced or weakened field conditions. The magnetic field distribution and the magnetic field strength in each of the flow gaps are shown in Fig. 11.

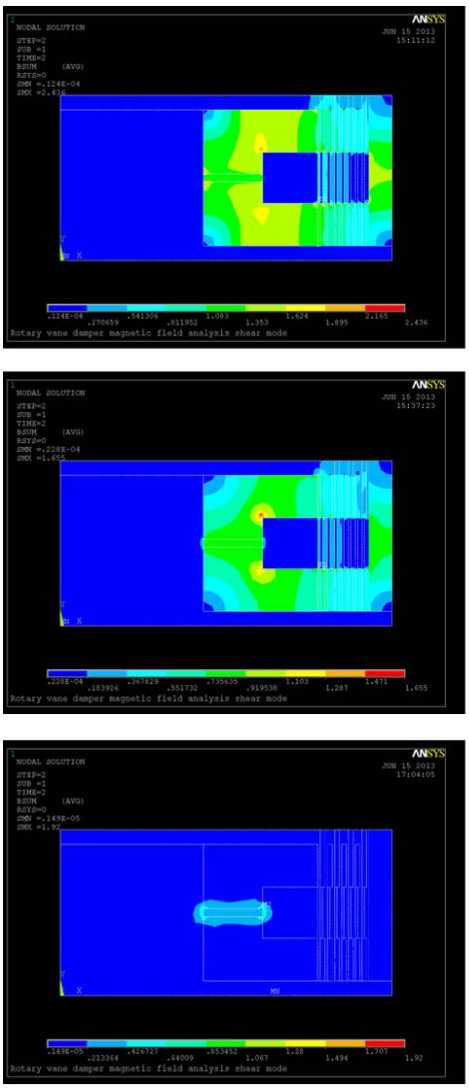

Fig. 11 Magnetic field results (A/m) using ANSYS for a 4-vane MREA

Figure 12 shows the magnetic field distribution at baseline (no external field applied), maximum and minimum applied field conditions. The maximum magnetic field occurs when the maximum design current (5 A) is applied to the solenoid and has same polarity as the permanent magnetic field lines. In contrast, the minimum magnetic field occurs when the minimum design current (–4 A) is applied to the solenoid where the negative sign indicates opposite polarity to permanent magnetic field lines. Figure 12 shows the calculated maximum magnetic field in the 8 flow gaps (see Fig. 9). The plots clearly show that depending on the polarity of the applied current in the electromagnetic circuit (solenoid), the multivane MREA can generate a magnetic field in the flow gaps that boosts or reduces the baseline magnetic field as required. Figure 12 also shows that as the radial distance between the bobbin and the flow gap increases, the magnetic field

strength tends to decrease. However, the aggregate magnetic field generated, thus the total MREA force from all flow gaps, does attain the required design criteria of the MREA (Fig. 13). The figure shows the calculated yield force based on analytical and ANSYS FEM analysis. The plots show that the results from FEM analysis tend to be lower than that of the analytical approach; however, the MREA performance goals are still achieved.

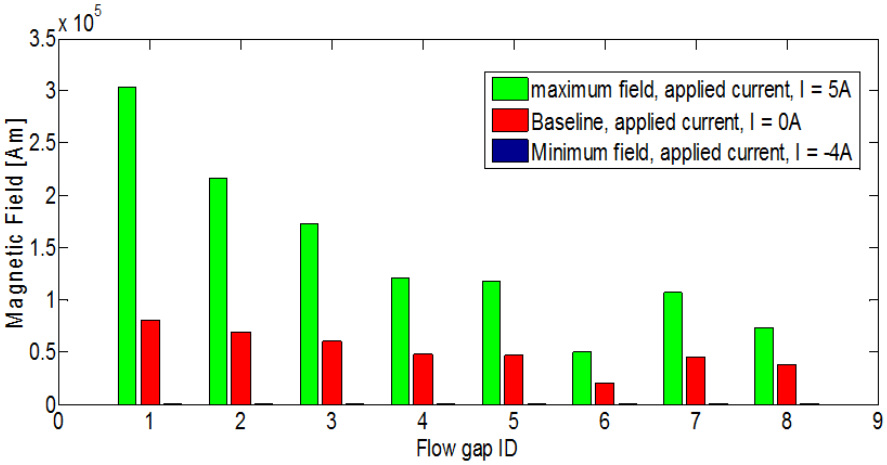

Fig. 12 Magnetic field strength at flow gaps

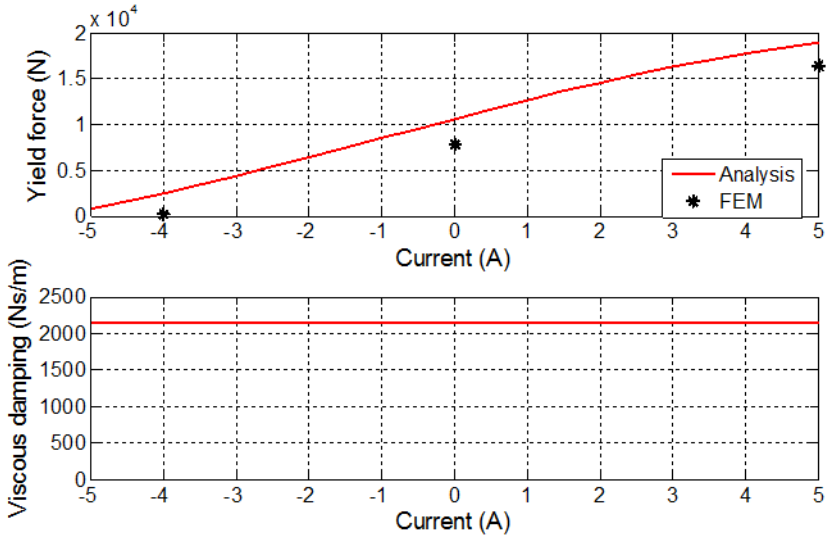

Fig. 13 Performance comparison between analytical and FEM analysis for a 4-vane MREA

2.1.1.3 Motion Convertor Design Analysis

Concurrently with the MREA design analysis, the project team analyzed motion conversion system configurations to convert linear motion of the platform seat assembly into rotational motion of the MREA during a crash event. The project team initially considered 2 approaches: 1) a rope and reel system and 2) a geared rack and pinion system. The rope and reel solution had potential to be the lightest, but did not provide ability to transmit MREA forces in both directions due to the unidirectional nature of a rope. In addition, the project team's experience from a preceding US Army Aviation Applied Technology Directorate (AATD) program has shown that cable dynamics, arising from elasticity and slackness, need to be considered for an effective and optimal performance. The geared rack and pinion approach has been successfully used by the project team in several preceding programs and provided a more reliable rotary-to-linear conversion; however, the weight penalty needs to be minimized. Based on previous experience conducting MREA component level testing and refinement, the project team used a geared rack and pinion system to ensure that desired force levels are met.

Gear Rack and Pinion Approach

The project team began designing the gear rack and pinion solution assuming a gear load of 22,250 N (5,000 lb), which is the sum of the expected viscous force at 8 m/s stroking velocity and maximum yield force. The project team considered the 4 configurations discussed previously for evaluation:

1) Single-MREA configuration with pinion diameter of
    a. 38 mm (1.5 inches): configuration 1
    b. 35 mm (1.375 inches): configuration 2
    c. 25 mm (1 inch): configuration 3
2) Two-MREA configuration with pinion diameter of 25 mm (1 inch): configuration 4

Single-MREA Configuration: This configuration involves the drive pinion and follower gear that engage with the gear rack to transmit torque (Fig. 14). The idler gear is used to reverse and transmit the pinion rotation to the follower gear. In this design, the total gear force, F_T , is 2,500 lb (half of the total gear load, since the total load is divided between the pinion and follower), the radial force, F_N, is 910 lb (resulting from a gear pressure angle of 18°), and the transmitted torque, T_P, is $2{*}F_T{*}r_p$, where r_p is the radius of the pinion. The radial forces, F_N, are counteracted using support rollers.

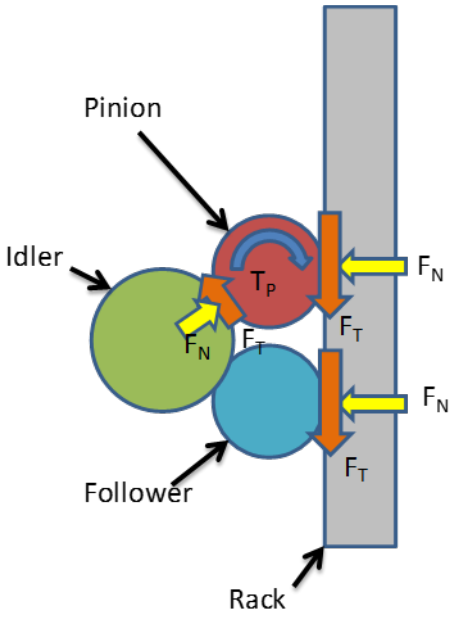

Fig. 14 Single-MREA configuration

Two-MREA Configuration: In this configuration, the drive pinion of each MREA directly engages on the opposite sides of the gear rack (Fig. 15). In this design, the total gear force, F_T, is again 2,500 lb (half of the total gear load), the radial force, F_N, is again 910 lb (with a pressure angle of 18°), and the transmitted torque, T_P, is $F_T * r_p$, where r_p is the radius of the pinion.

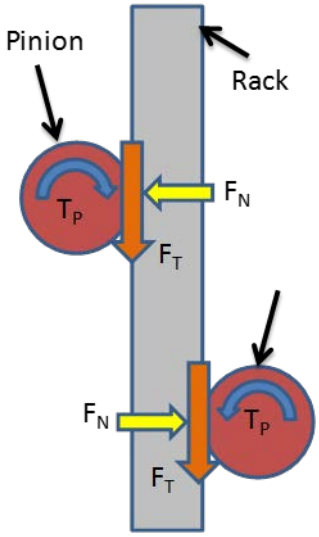

Fig. 15 Two-MREA configuration

The gear design analysis was conducted based on maximum tooth load. There are 2 primary modes of failure for gears: tooth breakage, which is caused from excessive bending stresses, and surface pitting or wear from excessive contact stresses fatiguing the surface by compression. However, since in our application

there is no gear rotation, thus no continuous cyclic gear load, until an impending crash occurs (i.e., single use), priority was given to design the gears based on maximum bending stresses. The maximum bending stress in a gear can be calculated using the Lewis bending stress equation for gears, given by

$$\sigma_y = \frac{F_T p}{C\,Y} K_v = \frac{F_N p}{C\,Y} \frac{1200+V}{1200}, \tag{5}$$

where p is the pitch, C is the face width, V is the velocity at the pitch diameter, in feet per minute, and Y is the form factor, which is a function of the number of teeth, pressure angle, and involute depth of the gear. It accounts for the geometry of the tooth. Since higher-velocity gear operation results in increased stresses due to impacts at initial contact, a velocity-based factor, K_v, is commonly included in tooth bending stress. High-strength material, such as 17-4PH stainless steel material, was selected for all gear components except the rack gear, which is designed to be made of titanium. The rack is the largest component of the gear system design, and the high-strength low-weight property of titanium was used to minimize the weight of the rack while design requirements are met. The results of the gear design (Tables 5 and 6) show that all configurations can accommodate the gear design with an adequate safety factor.

Table 5 Pinion gear design results. Material: 17-4PH stainless steel (σ_y = 183 ksi)

	Variable	Config 1	Config 2	Config 3	Config 4
c	Face width, (mm/inch)	34/1.33	34/1.33	25/1	41/1.6
Y	Form factor	0.308	0.295	0.245	0.245
P	Pitch (mm/inch)	18/0.7	16/0.63	12/0.5	12/0.5
V	Velocity, fpm	1,575	1,575	1,575	1,575
SF	Safety factor	2.04	1.94	2.45	1.84

Table 6 Rack gear design results. Material: titanium (σ_y = 120 ksi)

	Variable	Config 1	Config 2	Config 3	Config 4
c	Face width, (mm/inch)	34/1.33	34/1.33	25/1	41/1.6
Y	Form factor	0.484	0.484	0.484	0.484
P	Pitch (mm/inch)	18/0.7	16/0.63	12/0.5	12/0.5
V	Velocity, fpm	1,575	1,575	1,575	1,575
SF	Safety factor	2.1	2.1	3.15	2.36

To select the configuration with the minimum total system weight, the total weight (MREA plus gear system) was calculated, and the results are tabulated in Table 7. From the table, configuration 3, a single MREA with pinion diameter of 25 mm (1 inch), has the minimum system weight. In the previous section discussion, this configuration is the MREA design that was selected for further development in this project. While this weight is in addition to the MREA weight, much of this structure can be built into the seat design to replace structural components, thus minimizing the effect on overall seat weight.

Table 7 Total estimated MREA design weights

Parameter	Config 1	Config 2	Config 3	Config 4
No of MREA	1	1	1	2
MREA weight (kg/lb)	5.5/12	5.25/11.5	4.5/9.9	2.6/5.7
Total gear weight (kg/lb)	5/11	4.4/9.7	4.2/9.3	3.9/8.6
Total weight (kg/lb)	10.5/23	9.65/21.2	8.7/19.2	9.1/20

2.1.1.4 MREA Detail Design

Based on the total estimated design weight, the project team selected configuration 3 for the final design. The project team completed a detailed design of the weight and performance optimized MREA, including a rack and pinion motion conversion system. The selected MREA design is shown in Fig. 16. This MREA configuration has 4 rotary vanes, an overall length of 48 mm (1.88 inches), and diameter of 147 mm (5.8 inches).

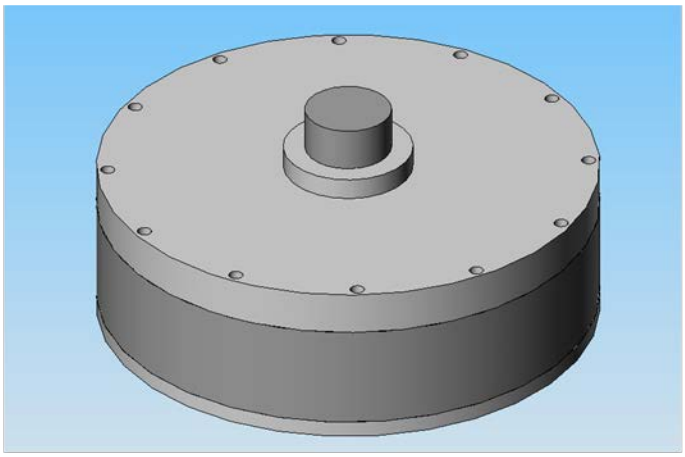

a) Isometric view of MREA

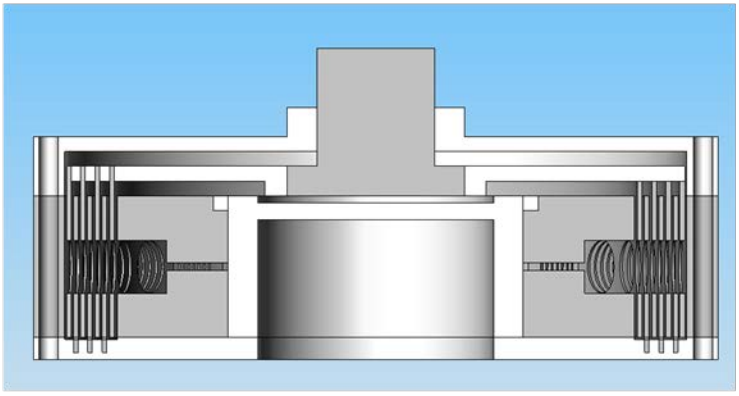

b) Section view of MREA

Fig. 16 Lightweight rotary-vane MREA design

An overview of the single MREA rack and pinion motion conversion system detail design is shown in Fig. 17. While the motion conversion system design analysis included a number of high-strength, lightweight features, the prototype motion conversion system design was instead optimized for cost and ease of manufacture to fit within the project budget. Rather than using a single follower/idler pair custom manufactured in high-strength stainless steel, 2 follower/idler pairs were included using off-the-shelf gears. The gear rack was also an off-the-shelf steel component rather than a custom titanium rack, once again to lower manufacturing costs. This prototype motion conversion system was used to demonstrate MREA performance, with the option to pursue a lightweight motion conversion system at a future point in this effort.

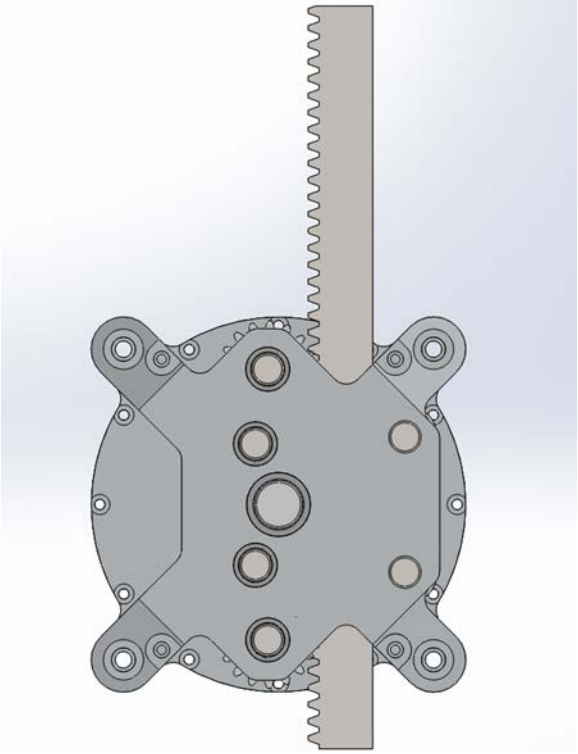

Fig 17 Complete MREA with rack and pinion system

2.1.1.5 Device Fabrication

All MREA components and motion conversion components were manufactured to specification and are shown in Fig. 18. The MREA device was then assembled as shown in Fig. 19.

Fig. 18 MREA and motion conversion components

Fig. 19 Fully assembled MREA

2.1.2 Task (b): Component Level Testing and Refinement

The project team evaluated the prototype MREA system at full-scale loads to demonstrate system performance. Evaluation was conducted in 2 ways: 1) in pure rotation coupled to a high-power DC motor (Fig. 20) and 2) with a motion conversion system using MTS 810 Test System (Fig. 21). The purpose of these 2 testing methods was to determine if there is any significant force contribution by the motion conversion system.

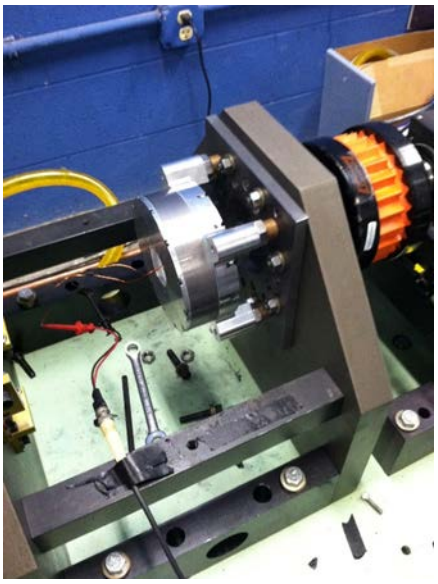

Fig. 20 MREA coupled to DC motor for pure rotation testing

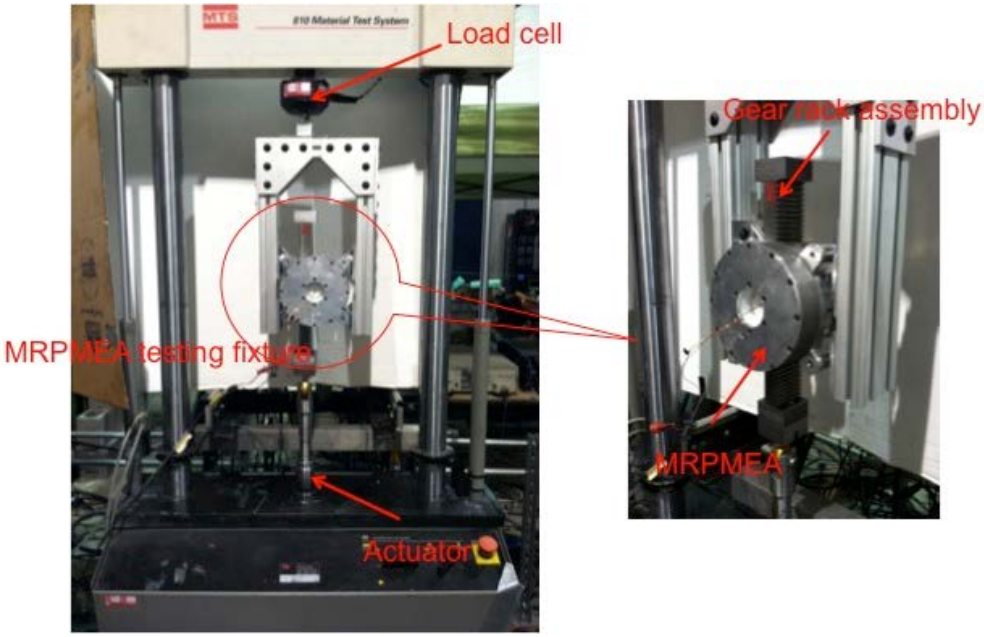

Fig. 21 MREA system in MTS system for testing with motion conversion

Results from the pure rotation tests are shown in Figs. 22 and 23. These results show that the MREA controllable yield force nearly matched the predictions using FEM magnetic field analysis (as discussed in Section 2.1.1) but were slightly lower than expected via in-house analyses. Figures 24 and 25 show raw force versus displacement and force versus velocity data from the linear stroking MTS tests as functions of applied electrical current. Using these data, MREA yield force and

viscous damping were calculated and plotted along with rotation test results as shown in Figs. 26 and 27. The rotation test results match well with MTS test results, suggesting that the motion conversion system has minimal effect on force levels.

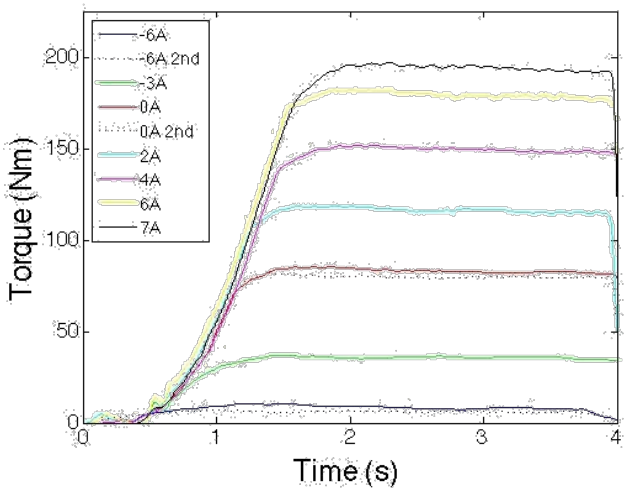

Fig. 22 Torque vs. time as a function of applied current to the MREA from rotation tests

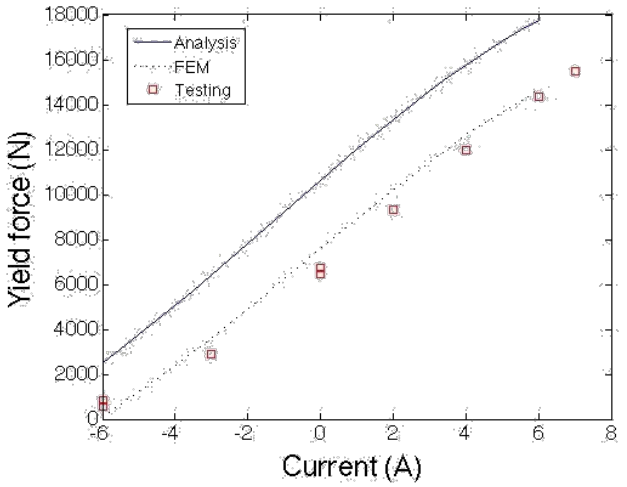

Fig. 23 MREA yield force as a function of applied current from rotation tests

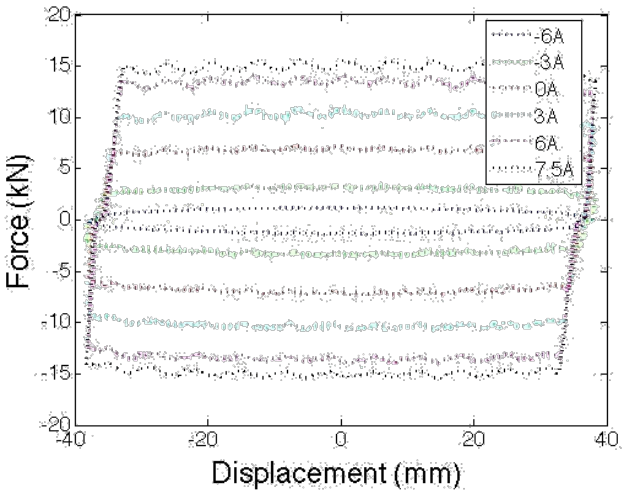

Fig. 24 Force vs. displacement from MTS tests as a function of applied current

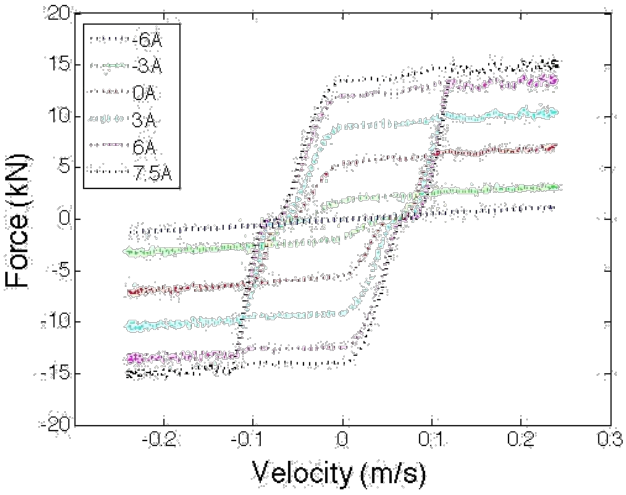

Fig. 25 Force vs. velocity from MTS tests as a function of applied current

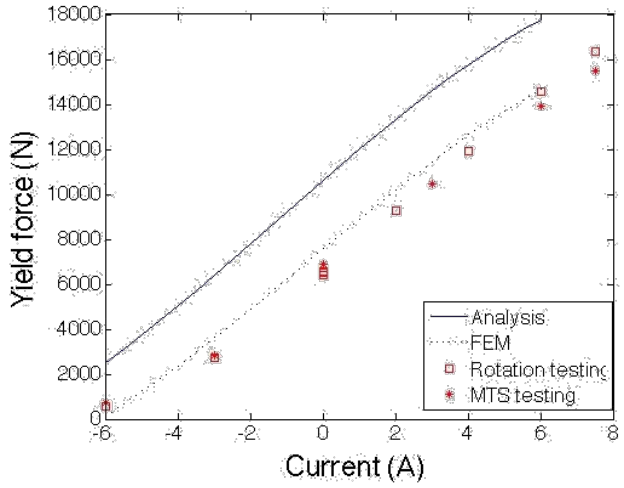

Fig. 26 MREA yield force as a function of applied current for both rotation and MTS tests

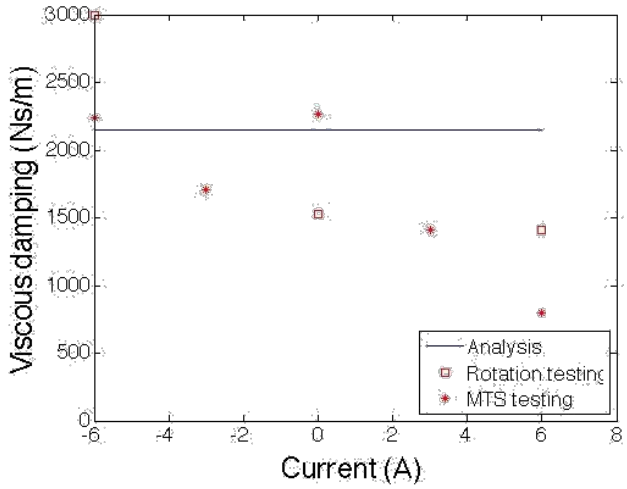

Fig. 27 MREA viscous damping as a function of applied current for both rotation and MTS tests

Given that the controllable yield force of the MREA was slightly lower than anticipated, the SDOF simulations discussed in Section 2.1.1 were conducted again considering these results to see the effect on the seat/occupant system. The project team found that there was insignificant effect on the 5th female occupant, while for the 95th male and 50th male (in fail-safe mode), the result showed a minor increase in stroke as shown in Figs. 28 and 29, respectively. Given that these increases in required stroke are modest, there is no pressing need for MREA refinement. However, should an increase in MREA yield force be desired, the project team explored 2 simple refinements: 1) increasing the thickness of the permanent magnet from 0.07 to 0.09 inch, and 2) decreasing the inner diameter (ID) from 2.5 to 2.25 inches. Figure 30 shows the effect of both of these refinements. The increased permanent magnet thickness has only a modest effect, while the decreased ID increases the yield force by more than 1,000 N.

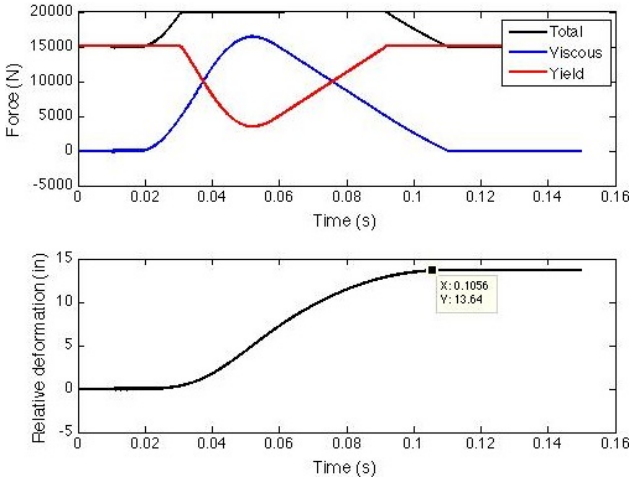

Fig. 28 SDOF dynamic simulations showing that lower MREA yield force increases stroke by less than 1.0 inch for the 95th male

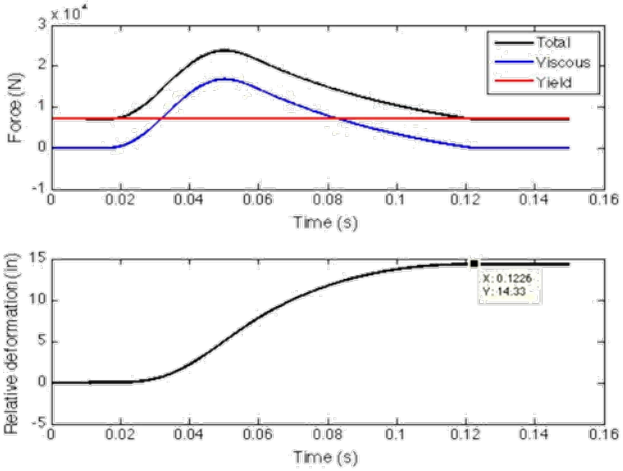

Fig. 29 SDOF dynamic simulations showing that the lower MREA yield force increases stroke by 1.9 inches for the 50th male in fail-safe mode

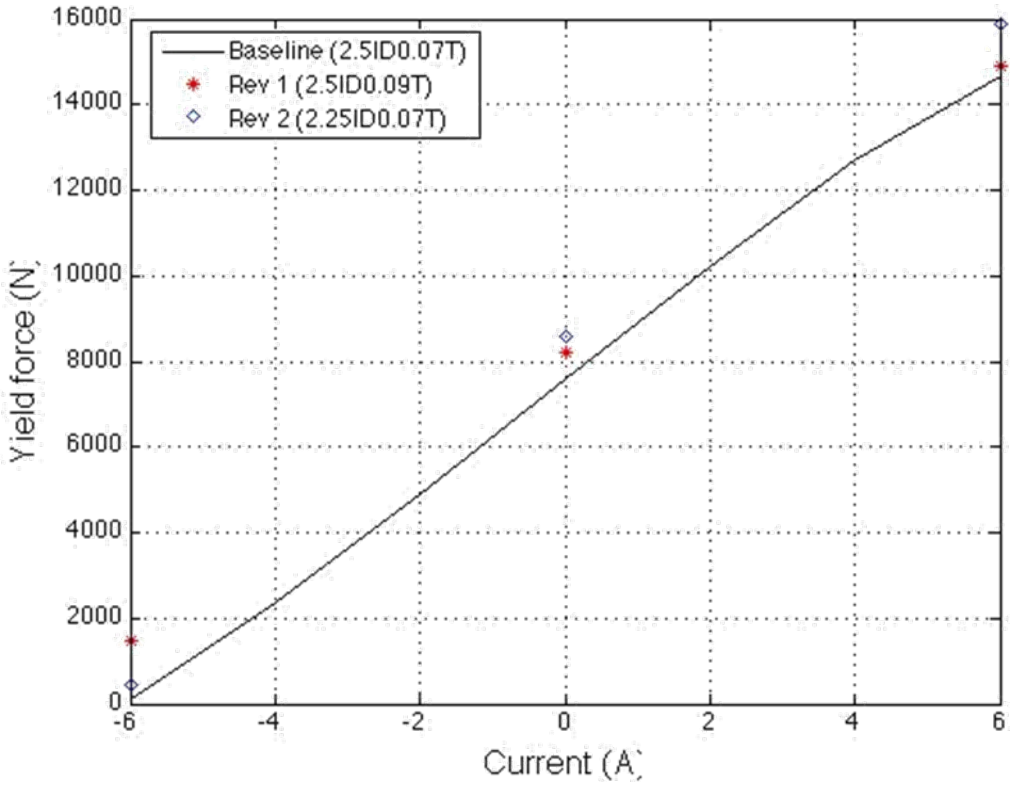

Fig. 30 Effect of modifying permanent magnet dimensions: increasing thickness from 0.07 to 0.09 inch yields modest increase in yield force; decreasing ID from 2.5 to 2.25 inches yields less than 1-kN increase in yield force

2.2 Objective 2: Design, Fabricate, and Demonstrate MFEA Device in Component-Level Testing

As a preliminary performance prediction, the maximum normal force with a magnetostrictive (MS) material (Terfenol-D) was analyzed. In the model, the MS material was treated as a stiffness element and stroke was applied externally for emulating a magnetostriction effect. Based on the model simulations, we found that diameter and length of the MS material are the main design parameters. With a 3/4-inch-diameter and 6-inch-long Terfenol-D actuator, a normal force of more than 1,500 lb was predicted. Considering a decent friction coefficient (0.6~0.8), we just needed to stack 4 of the friction mechanisms to meet the seat damper design criteria. However, the friction coefficient announced in public literature is usually measured by force control condition using enough strokes to maintain the normal force. To measure the friction coefficient with a small stroke variation, a friction test rig was designed and fabricated using a commercially available Terfenol-D actuator. The friction test setup was assembled and preliminary friction measurements were conducted using 2 different Terfenol-D actuators (Etrema Product Inc., LLAS-250 and HLAS-150). The project team developed a servo motor controller and data acquisition program using dSPACE real-time system. From the preliminary test, the preloaded Terfenol-D actuator stroke was less than predicted, and the results showed a low normal force increase from the static test for the case of contact between aluminum-to-aluminum specimens. The friction measurement test was conducted for aluminum-to-aluminum friction material case. The experiments were conducted for constant current driving for Terfenol-D actuator with various prestress settings using a coil spring. The maximum friction coefficient measured was 0.75 with aluminum friction material with the preload value of 100 lbf and rotational speed of 400 rpm. The project team fabricated steel-to-steel test specimens for comparison of the friction tests. For this specimen the surface was heat treated for surface hardening. For the heat-treated plate, the initial friction factor was only 0.17; however, after high-speed test, the factor increased up to 0.5 for 200-rpm rotational speed.

2.2.1 Task (a): MFEA Simulation, Design, and Fabrication

Terfenol-D is an alloy of terbium, dysprosium, and iron metals and has the largest room temperature magnetostriction. Magnetostriction is the change in shape exhibited by some materials when subjected to changes in the magnetization state. Terfenol-D has large strain, high force, wide bandwidth, and high-energy density as shown by physical properties in Table 8.[4] The relatively large strain and force output of MS Terfenol-D has led many researchers to focus on its uses for actuation.

Table 8 Terfenol-D physical properties[a]

Property type	Property	Nominal composition $Tb_{0.3}Dy_{0.7}Fe_{1.92}$
Mechanical	Young's modulus	25–35 GPa
	Sound speed	1,640–1,940 m/s
	Tensile strength	28 MPa
	Compressive strength	700 MPa
Thermal	Coefficient of thermal expansion	12 ppm/°C
	Specific heat	0.35 kJ/kg-K
	Thermal conductivity	13.5 W/m-k
Electrical	Resistivity	58×10^{-8} O-m
	Curie temperature	380 °C
Magnetostrictive	Strain (estimated linear)	800–1,200 ppm
	Energy density	14–25 kJ/m^3
Magnetomechanical	Relative permeability	3–10
	Coupling factor	0.75

[a] Adapted from Etrema Products, Inc. Terfenol-D physical properties. Ames (IA): Etrema Products, Inc. http://www.etrema.com/terfenol-d/.

Friction forces arising from the relative motion of 2 contacting surfaces are a well-known source of energy dissipation. Sometimes this is an unwanted effect of the design, but it can also be intentionally used to increase the damping of a certain system in a simple and cost-effective way. Because the actuator only needs to change the normal force exerted onto the vibrating element, it requires very little actuating displacement and mechanical power. The active element, Terfenol-D in this study, is not required to generate a displacement having the same order of motion as the mounts. Therefore, the amount of work done by the control actuator is significantly smaller than that required of a purely active control actuator. Also, since the friction actuator only dissipates energy from the system, it cannot cause instabilities to occur. Because of their high force and bandwidth capability, Terfenol-D actuators appear to be a natural candidate as friction dampers. However, the maximum mechanical strain of these devices is only about 1,000 ppm, which can be a big challenge for the application.

In this study, as a preliminary performance prediction, the maximum normal force from Terfenol-D (an MS material) actuator is calculated. The basic configuration of the friction damper for normal force calculation is shown in Fig. 31. Each element is considered a spring element, and the spring constant is calculated using[5]

$$k_e = \frac{E_e A_e}{L_e}, \tag{6}$$

where E denotes Young's modulus, A is the cross-sectional area, and L indicates length of the material for each element (e).

Figure 32 shows the preliminary simulation result of normal force of Terfenol-D with aluminum at 60 μm of effective strain as a function of Terfenol-D diameter. Table 9 summarizes the friction coefficient from metal-based friction materials.

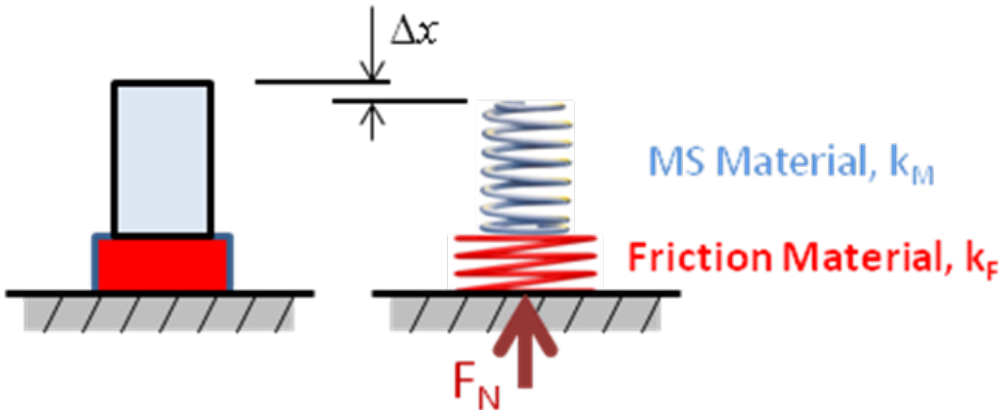

Fig. 31 Friction damper schematic diagram for normal force calculation

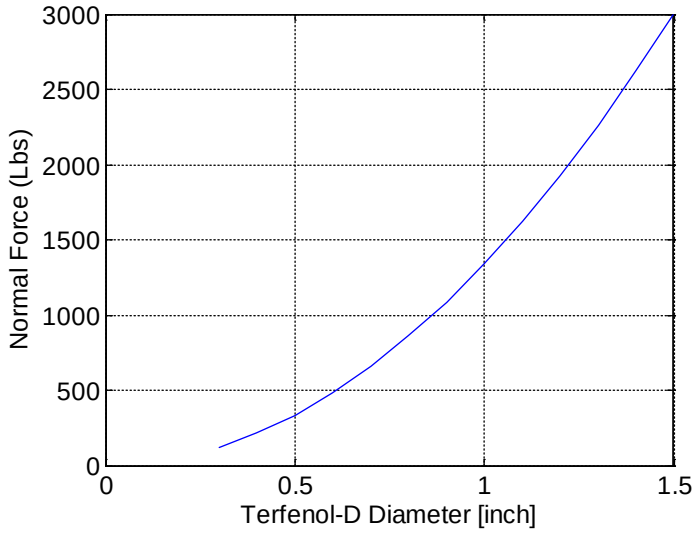

Fig. 32 Simulation result of the normal force vs. Terfenol-D diameter

Table 9 Candidates of friction materials

Material 1	Material 2	Coefficient of friction			
		Dry		Greasy	
		Static	Sliding	Static	Sliding
Aluminum	Aluminum	1.05[a]–1.35[b,c]	1.4[d]	0.3[b,c]	. . .
Aluminum	Mild steel	0.61[e]	0.47[d]	. . .	. . .
Steel (mild)	Steel (mild)	0.74[f]	0.57[d]	. . .	0.09[d]–0.19[g]
Steel (mild)	Steel (mild)	. . .	0.57[g]	. . .	. . .

Notes:
[a] Ernst H, Merchant ME Proceedings of the Special Summer Conferences on Friction and Surface Finish; 1940 Jun 5–7; Cambridge, MA. Cambridge (MA): Massachusetts Institute of Technology; 1940.
[b] Oberg E, editor. Machinery's handbook: eighteenth edition. Norwalk (CT): Industrial Press; 1968.
[c] Quayle JP, editor. Kempe's engineers year-book 1980 (85th edition). London (England): Morgan-Grampian Book Publishing Co. Ltd; 1980.
[d] Beare WG, Bowden FP. Physical properties of surfaces. I. Kinetic friction. Phil Trans Roy Soc A; 1935;234(741):329–354.
[e] Tomlinson GA. A molecular theory of friction. Phil Mag. 1929;7:905–939.
[f] Hardy WB, Hardy JK. Note on static friction and on the lubricating properties of certain chemical substances. Phil Mag. 1919;38(223):32–48.
[g] EngineersHandbook.com. Coefficient of friction reference table. [accessed 3 June 2016]. http://www.engineershandbook.com/Tables/frictioncoefficients.htm.

2.2.2 Task (b): Component-Level Testing and Refinements

To measure the friction coefficient with a small stroke variation, a friction test rig was designed and fabricated using commercially available Terfenol-D actuator as shown in Fig. 33. For the MS actuation, we purchased 2 variations of Terfenol-D actuator: LLAS-250 (250-μm stroke, 250-lb block force) and HLAS-150 (150-μm stroke, 500-lb block force). The measuring devices included a load cell, torque sensor, and displacement laser sensor. The proper sensor ranges were investigated and purchased for the friction measurement testing. The friction test setup was assembled and the friction measurements were conducted. The project team developed a servo motor controller and data acquisition program using dSPACE real-time system.

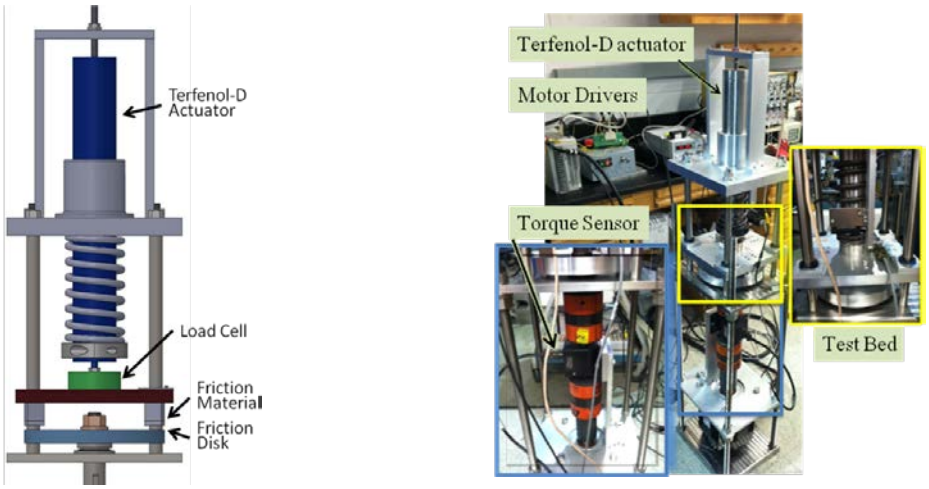

Fig. 33 Friction test rig for MFEA development

The friction measurement test was conducted for aluminum-to-aluminum and steel-to-steel friction material cases. Figures 34 and 35 show the experimental results, respectively. The experiments were conducted for constant current driving for the Terfenol-D actuator with various prestress settings using a coil spring (Fig. 33). The maximum friction coefficient, as shown in Fig. 36, measured 0.75 with aluminum-to-aluminum friction material with the preload value of 100 lb and rotational speed of 400 rpm. The friction coefficient from this experiment shows about half of the value in Table 9. The results in Table 9 are based on force control mode experiment; however, the Terfenol-D actuator has limited stroke and therefore should have a limitation of normal force increase. The result in this study includes only the variation component of the friction measurement, which is not including the static friction component. During the test we observed apparent wear signature of the surface, and it can be a factor for showing lower friction factor. For the steel-to-steel friction material specimen fabrication, the surface was heat treated for surface hardening. For the heat-treated plate, the initial friction factor was only 0.17; however, after the high-speed test, the factor increased up to 0.5 for 200-rpm rotational speed. Due to the surface hardening heat treatment, the friction factor at the low-speed test was low, but as the speed increased, the surface layer wore out and the friction factor came up to the normal. However, the wear from steel material showed much less than aluminum material.

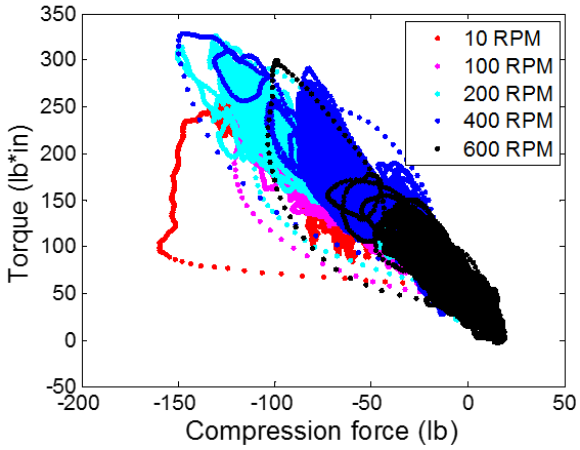

Fig. 34 Friction test results for aluminum-to-aluminum friction material

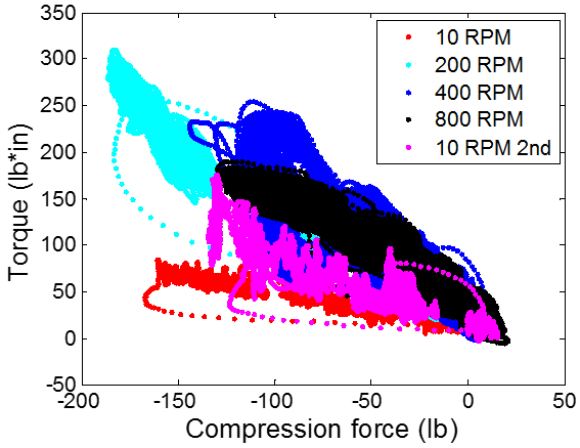

Fig. 35 Friction test results for steel-to-steel friction material

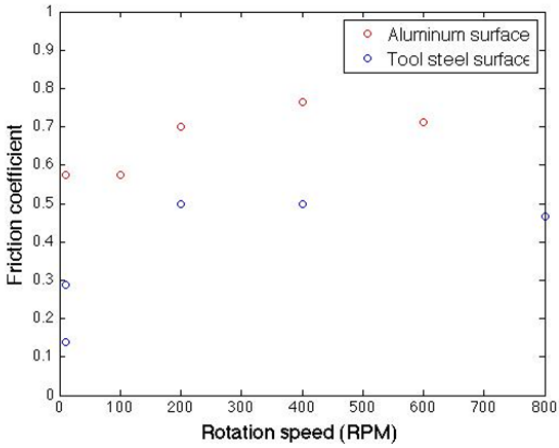

Fig. 36 Friction coefficients for aluminum-to-aluminum and steel-to-steel friction material along the rotation speed of measurement

3. FY2014 Accomplishments

The objectives for FY14 were to

1) Conduct seat-occupant system-level modeling and simulation to evaluate biodynamic response using novel EAs (MREA and MFEA devices).

2) Design and fabricate a ruggedized test seat for integrating novel EAs.

Techno-Sciences, Inc. (now InnoVital Systems, Inc.), was responsible for design and fabrication of the test seats integrated with ASEA technologies (Objective 2). ARL-VTD was responsible for system-level model development and simulation (Objective 1).

3.1 Objective 1: Conduct Seat-Occupant System-Level Modeling and Simulation to Evaluate Biodynamic Response Using Novel EAs

The project team pursued an advanced semi-active end-stop control algorithm development during the fourth quarter of FY14. Figure 37 shows the new control algorithm flowchart for MatLab/Simulink program. This control flow implements the multibody dynamic model block ("adams_sub" block) of MSC Adams software for running co-simulation with the control scheme software plugin. The input to the "adams_sub" block is damping force, and the 3 outputs from the block are the seat displacement, x , floor-pan absolute velocity, $\dot{x}_0$, and the seat absolute velocity, $\dot{x}$.

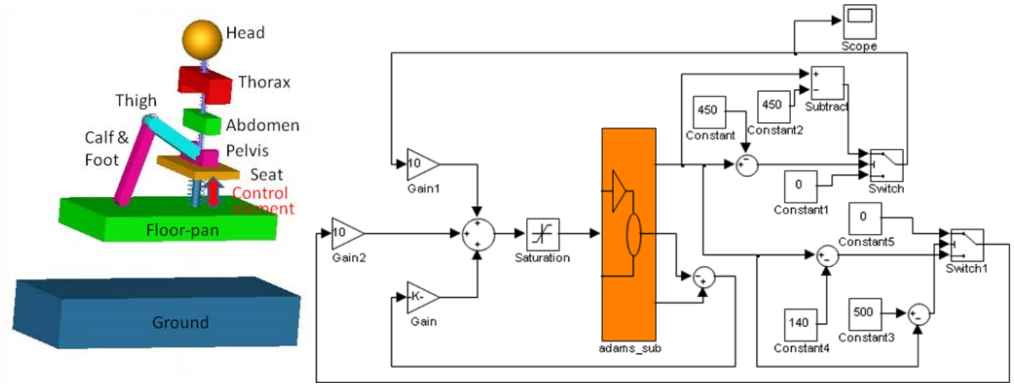

Fig. 37 Adams-MatLab/Simulink co-simulation control flow diagram for end-stop control and a control simulation result

To better understand occupant kinematics during vertical helicopter crashes, the project team developed a detailed finite element model of the occupant-seat system. The system-level model consists of Hybrid III Anthropomorphic Test Device

(ATD) models representing 5th percentile, 50th percentile, and 95th percentile occupants seated on a helicopter crew seat with a 5-point belt restraint (Fig. 38). The system-level finite element model was run using LS-DYNA crash/impact analysis software. Figure 38 shows the end kinematic states of different types of occupants for the case of passive EA with a symmetrical triangular vertical crash pulse of maximum 51 g's, as specified in MIL-S-58095A[1]. These finite element simulations were used to support crash dynamic sled testing during FY15.

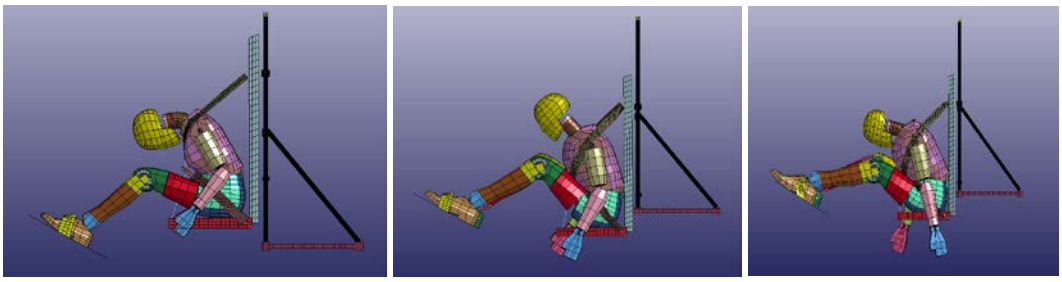

(i) 5th percentile female (ii) 50th percentile male (iii) 95th percentile male

Fig. 38 Occupant kinematics from finite element analysis (LS-DYNA)

3.1.1 Task (a): System-Level Model Development

3.1.1.1 Seated Human Model

Consider a human sitting upright in a rotorcraft crew seat. A variety of mathematical models has been proposed to describe the human body's response to vertical disturbances. In this study, Boileau's model[6] is used as a basic parameter model. However, Boileau's model was developed for "average" passenger comfort evaluation and it has no lower leg consideration, which may be important for overall human body kinematics under an extreme environment. To resolve this problem, the body segment mass was extracted from anthropometric specifications for dummy family[7] for the 5th percentile female (small female), 50th percentile male (average male), and 95th percentile male (large male). The proposed lumped parameter human body model, shown in Fig. 39, comprises 6 masses for the respective 6 body segments, coupled by linear/nonlinear elastic and damping elements. The 6 masses represent the following 6 body segments: the head and neck (m_1); the thorax (m_2); the abdomen (m_3); the pelvis (m_4); the thighs (m_5); and the calf and foot (m_6). The estimated segment mass and mass moments of inertia properties are summarized in Table 10. The hand and arm masses (upper extremity) are not incorporated in the model assuming its negligible contributions to the whole-body biodynamic response. The stiffness and damping properties of the cervical spine are represented by k_1 and c_1, those of the thoracic spine by k_2 and c_2, those of the lumbar spine by k_3 and c_3, while those of the buttocks and thighs on a seat by k_4 and c_4 (Fig. 39). Also, there are 2 torsion stiffness and damping

parameters for hip (k_5, c_5) and knee (k_6, c_6) joints.[8] Manseau and Keown[9] reported that the military boot has a significant effect on the complex lower leg injury severity. To take into account this boot effect, stiffness and damping parameters (k_b and c_b) were also implemented in the model as shown in Fig. 39. These stiffness and damping parameters[10] are summarized in Table 11 with the source of the data. Overall, this multibody human model was developed at ARL primarily for vertical impact injury assessment simulations in vehicular extreme environment scenarios such as crash or mine blast.[11]

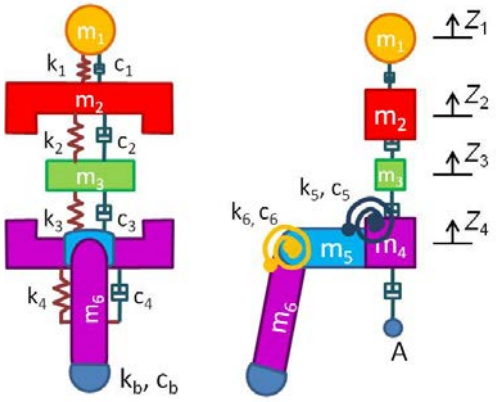

Fig. 39 Lumped-parameter human body model

Table 10 Estimated segment mass and inertial properties[7]

Body segment	Small (5th percentile) female	Medium (50th percentile) male	Large (95th percentile) male
	Mass (kg)	Mass (kg)	Mass (kg)
Head (m_1)	4.30	5.10	5.68
Thorax (m_2)	12.98	23.76	32.42
Abdomen (m_3)	1.61	2.37	2.95
Pelvis (m_4)	6.98	11.41	16.04
Thigh (m_5)	11.83	17.23	11.34
Calf and foot (m_6)	6.00	9.14	6.61
Total	48.22	76.56	102.46

Table 11 Stiffness and damping coefficients of the human body segments

Body segment	Stiffness	Damping	Source
Cervical spine (k_1, c_1)	310.0 [*kN/m*]	400.0 [*N·s/m*]	[Ref. 7]
Thoracic spine (k_2, c_2)	183.0 [*kN/m*]	4750.0 [*N·s/m*]	
Lumbar spine (k_3, c_3)	162.8 [*kN/m*]	4585.0 [*N·s/m*]	
Buttocks (k_4, c_4)	90.0[*kN/m*]	2064.0 [*N·s/m*]	
Hip joint (k_5, c_5)	Extension [*N·m/rad*]: 68.8 Flexion [*N·m/rad*]: $53.2 \cdot \text{Exp}(0.98 \times \theta_2)$-53.2	100.0 [*N·m·s/rad*]	
Knee joint (k_6, c_6)	Extension [*N·m/rad*]: $90.5 \cdot \text{Exp}(2.0 \times \theta_3)$–90.5 Flexion [*N·m/rad*]: $95.0 \cdot \text{Exp}(4.32 \times \theta_3)$-95.0	500.0 [*N·m·s/rad*]	[Ref. 9]
Boot (k_b, c_b)	300.47 [*kN/m*]	200.0 [*N·s/m*]	[Ref. 11]

The conceptual model of the rotorcraft floor structure with a crew seat used in this study is shown in Fig. 40. The point "A" in Fig. 40 shows the coupling between the seat-occupant model and the rotorcraft floor structure.

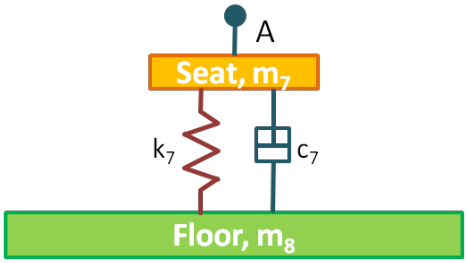

Fig. 40 Coupling between rotorcraft floor structure and seat-occupant model

3.1.1.2 Biodynamic Evaluation of Seated Human Model

The biodynamic responses of a seated human subjected to vertical vibration or shock exposure have widely been assessed in terms of seat-to-head (STH) transmissibility (TR) and driving-point mechanical (DPM) impedance (IM).[12] To evaluate these performance indices, the whole human body model, shown in Fig. 39, was implemented in the multibody dynamic simulation software, MSC Adams and each segment responses were simulated using the Vibration module in the software. The frequency step and frequency range of 0.5 Hz and up to 100 Hz were selected, respectively.

STH TR

This function, STH TR, is defined as the ratio of output head response to input seat excitation. It can be defined by the acceleration or displacement ratio. Therefore, TR can be expressed as shown in the cited reference[12]

$$TR = \frac{Z_1(j\omega)}{Z_A(\omega)}, \tag{7}$$

where ω is frequency, $Z_A(\omega)$ is input displacement amplitude from seat, and $Z_1(j\omega)$ is output displacement amplitude from head and neck m_1. Figure 41 presents a comparison of the TR magnitude characteristics calculated from the model with the mean and envelope of the experimental data from the cited reference.[6]

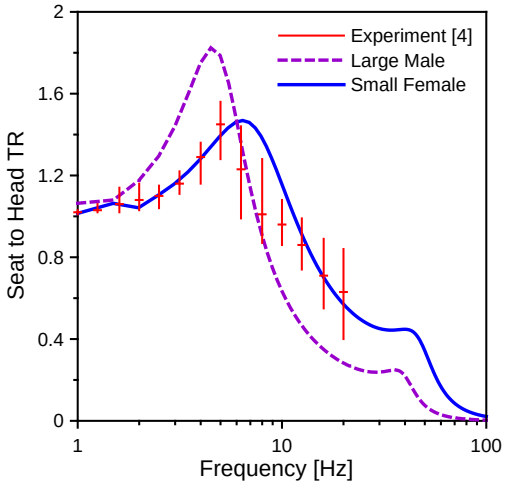

Fig. 41 Comparison of the vertical STH vibration TR characteristics computed from the proposed human body model with those upper and lower limits of experimental data from Boileau and Rakheja[6]

DPM IM

This function, DPM IM, is defined as the ratio of driving force between pelvis and seat to the input velocity of the seat. Accordingly, IM can be represented as follows[12]:

$$IM = \left| \frac{(k_4 + j\omega c_4)[Z_A(\omega) - Z_4(j\omega)]}{j\omega Z_A(\omega)} \right|, \tag{8}$$

where ω is frequency, $Z_A(\omega)$ is input displacement amplitude from seat, and $Z_4(j\omega)$ is output displacement amplitude from pelvis m_4. Fig. 42 presents a comparison of the IM magnitude characteristics calculated from the model with the mean and envelope of the experimental data from the reference.[6]

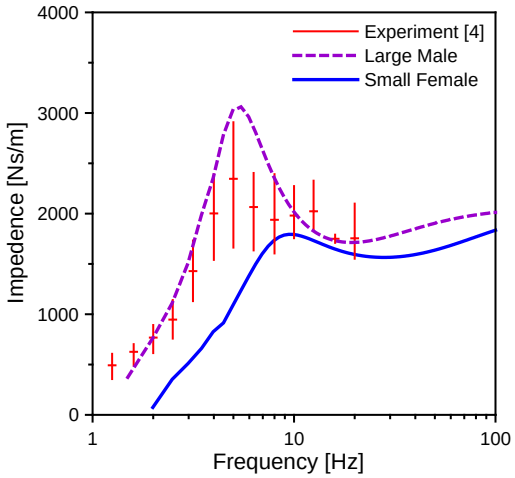

Fig. 42 Comparison of the vertical DPM IM characteristics computed from the proposed human body model with those upper and lower limits of experimental data from Boileau and Rakheja[6]

3.1.2 Task (b): Adaptive Control Algorithm and System-Level Simulations and Refinements

For vibration isolation of seat damper, high damping will suppress the amplitude response, but worsen the vibration TR. Low damping will improve the TR, but the relative displacement between the seat and floor may be large enough to cause end-stop impacts especially for high shock input from the crash event. If the shock input force does not cause the suspension mechanism to hit the end-stop buffers, a lower suspension damping may provide greater vibration isolation performance. However, for the input force from the crash event, an adjustable damper, which can be switched manually or automatically between a high damping and low damping according to the passenger's weight or damper deflection, might be used. If the damper is generally set to soft mode to provide low TR, and adjusted to the hard mode only when end-stop impacts are likely to occur, the optimum performance might be achieved.[13] End-stop impacts will occur whenever the relative displacement between the seat and floor exceeds certain value. If the damper is switched on whenever the relative displacement exceeds a preset displacement threshold, d_L, severe end-stop impacts might be prevented.

Figure 43 shows the semi-active control algorithm flowchart for Simulink/MatLab program. This control flow implements the multibody dynamic model block ("adams_sub" block) of MSC Adams for running co-simulation with the control scheme software plugin. The input to the "adams_sub" block is damping force, and the 3 outputs from the block are the seat displacement, x, floor-pan absolute velocity, $\dot{x}_0$, and the seat absolute velocity, $\dot{x}$. Considering the power limitation of the MR damper for semi-active skyhook control (Fig. 43), the maximum feedback

force to the “adams_sub” block was set to 15 kN using the “Saturation” block function.

The control scheme can be expressed as

$$Fd = \begin{cases} G2\dot{x}(\dot{x} - \dot{x}_0), & d_{seat} \geq d_L \\ (G1 + G2)\dot{x}(\dot{x} - \dot{x}_0), & d_{seat} < d_L \end{cases}. \quad (9)$$

The control gains, G1 and G2, are functions of passenger weight, and the gains for this study are summarized in Table 12 for the human body model.

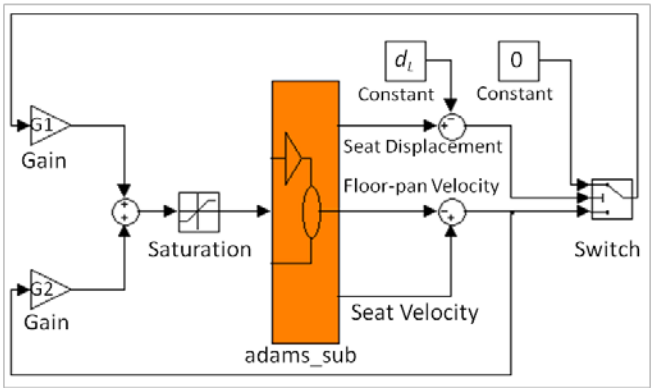

Fig. 43 Simulink control flow diagram for end-stop control

Table 12 Control parameters

Body model	Small (5th percentile) female	Medium (50th percentile) male	Large (95th percentile) male	Unit
G1	1	2	3	kN/ (m/s)
G2	0.01	0.05	0.3	kN/ (m/s)
d_L	335	335	335	mm

The biodynamic model (Fig. 39) and the rotorcraft floor model (Fig. 40) were combined and implemented in MSC Adams as shown in Fig. 44. An active control element was implemented and designed to generate force in between the floor-pan and seat. The nonlinear human biodynamic model was co-simulated with Simulink control scheme plugin as shown in Fig. 43. “Co-simulation” (cooperative simulation) is a simulation methodology that allows individual components to be simulated using different simulation tools running simultaneously and exchanging information in a collaborative manner. The nonlinear human body model in MSC Adams was generated in Simulink accessible code (.m-file and .mdl-file, “adams_sub” block in Fig. 43) through the Adams control module.

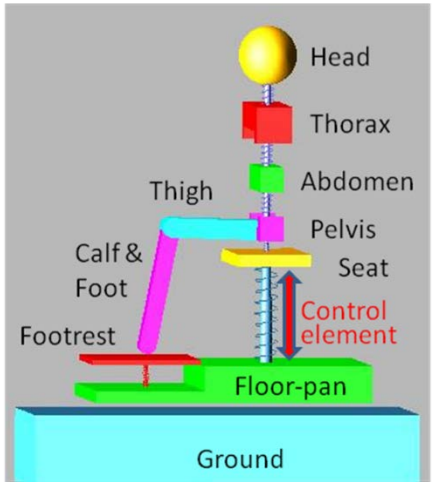

Fig. 44 A lumped-parameter seat-occupant model

Figures 45–47 show the simulation results for 3 cases, namely, 5th percentile, 50th percentile, and 95th percentile occupant models. Figure 45 show the reduction of lumbar load for 5th percentile analysis case between the baseline (passive EA with no control) and MREA with control. In Fig. 45, the peak lumbar load for the baseline case is 1,477 lbf (exceeds injury assessment reference values [IARV] limit), whereas the peak load for MREA with control analysis case is 926 lbf (<933 lbf IARV). Thus, it has been shown through analysis that by choosing an adaptive MREA with right type of control algorithm, it is possible to mitigate thoracic spinal injury (lumbar load is a measure of this injury) to a seated occupant in a rotorcraft vertical crash event. For the 50th percentile analysis case (Fig. 46), the peak lumbar load is reduced from 2,248 lbf (baseline) to 1,388 lbf (MREA with control) keeping the lumbar load well within the IARV limit for this severe crash scenario. For the 95th percentile occupant analysis case (Fig. 47), the peak lumbar load can be reduced from 2,342 to 1,748 lbf, which is well within the IARV limit. These analysis cases show that it is possible to optimize the adaptive MREA device with a proper control algorithm for the crash scenarios that are of interest to improve the safety and survivability in rotorcraft crashes.

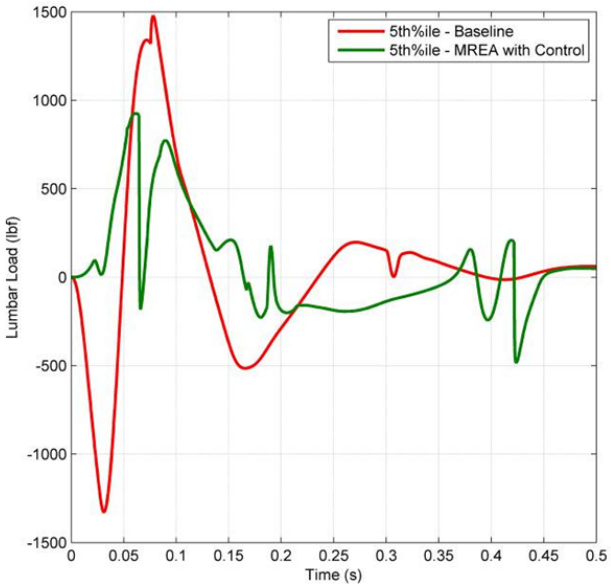

Peak Lumbar Load (Baseline) = 1477 lbf
Peak Lumbar Load (MREA w/Control) = 926 lbf
Lumbar Load - IARV Limit for 5th%ile = 933lbf

Fig. 45 Baseline vs. MREA with control: 5th percentile

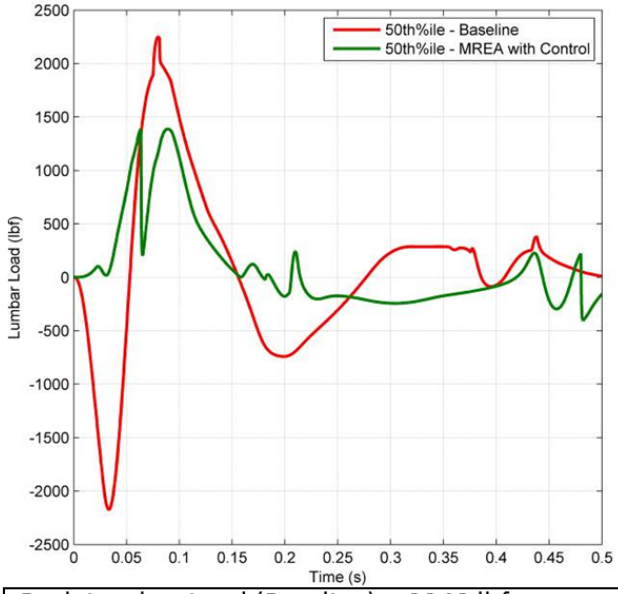

Peak Lumbar Load (Baseline) = 2248 lbf
Peak Lumbar Load (MREA w/Control) = 1388 lbf
Lumbar Load - IARV Limit for 50th%ile = 1395 lbf

Fig. 46 Baseline vs. MREA with control: 50th percentile

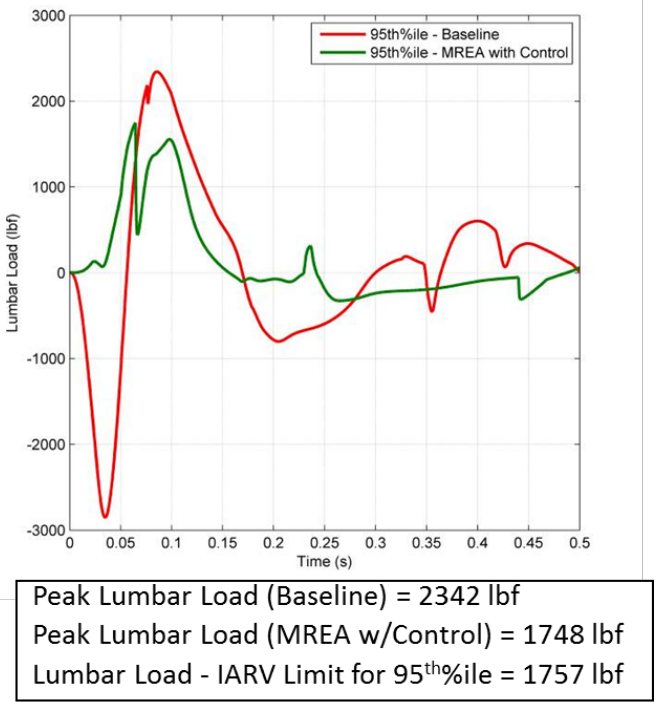

Fig. 47 Baseline vs. MREA with control: 95th percentile

3.2 Objective 2: Design and Fabricate a Test Seat for Integrating Novel EAs

The performance metric for this task was to design a test seat with structural stresses less than yield strength of chosen materials for load conditions per MIL-STD-58095A[1]. Per the analyses conducted and presented in this section, these objectives were successfully met.

3.2.1 Task (a): Seat Design

3.2.1.1 Integration Design Trade Studies

The period of performance for Techno-Sciences Inc.'s (now InnoVital Systems) contract to conduct test seat design studies began on 7 March 2014. At that point, the program team commenced trade studies for seat design architecture with the following goals:

1) Easily integrated with the rotary MREA system without sacrificing performance or causing additional unwanted dynamics in a crash event

2) Structurally adequate to handle multiple pure vertical crash tests for EA evaluation

3) Seat bucket mass must be within reasonable range of existing fielded designs, such that the existing MREA force levels are sufficient
4) 5-point restraint
5) Similar occupant positioning to fielded seats
6) Minimized development and fabrication cost
7) Can be integrated with a conventional EA device for comparative testing

The project team evaluated multiple seat design concepts as well as multiple existing fielded seats against these design goals. As a result of this study, the project team determined that the best solution to satisfy these goals is to leverage components from an existing fielded seat design, specifically the S7000 series of helicopter crew seats from BAE Protection Systems. This series of seats is currently fielded in several variants of military helicopters, including the MH-60R, MH-60S, UH60M, and UH60A/L, with slight variations in armoring and features for each. Based upon prior related programs, the team had several scrapped components of these seats that could be leveraged into the test seat design. In particular, the project team had access to multiple sets of major components associated with the MH-60R crew seats. Figure 48 shows the computer-aided design model for this MH-60R seat. The advantage of using this seat design as a base for the test seat design is that it is proven in both the field and in the laboratory to withstand multiple pure-vertical impacts, inherently maintains the restraint and occupant positioning of the field, and can be tested in original equipment manufacturer (OEM) configuration for comparative testing. By leveraging an already designed and proven seat as well as components that were already in-house, development and fabrication costs were significantly minimized.

Fig. 48 MH-60R seat manufactured by BAE Protection Systems (formerly Simula, Inc.), front isometric view

To evaluate the ease of MREA integration, it was first necessary to describe the relevant load paths for the OEM configuration of this seat. Figure 49 shows a rear view of this seat design. The seat bucket is outfitted with 4 linear bearings (shown in red) that slide alone 2 vertical guide tubes (blue) and provide lateral constraint while enabling a vertical degree of freedom. Fixed load (inversion tube) EAs (shown in green) connect from the lower rear of the stroking seat bucket via a seat height adjustment mechanism (purple) to the top of the guide tubes. As such, in a crash event, the downward inertial force of the stroking seat bucket and occupant masses are reacted through an upward reaction force provided by the EAs, which, in turn, provide a downward compression force on the guide tubes as indicated by the arrows in Fig. 49.

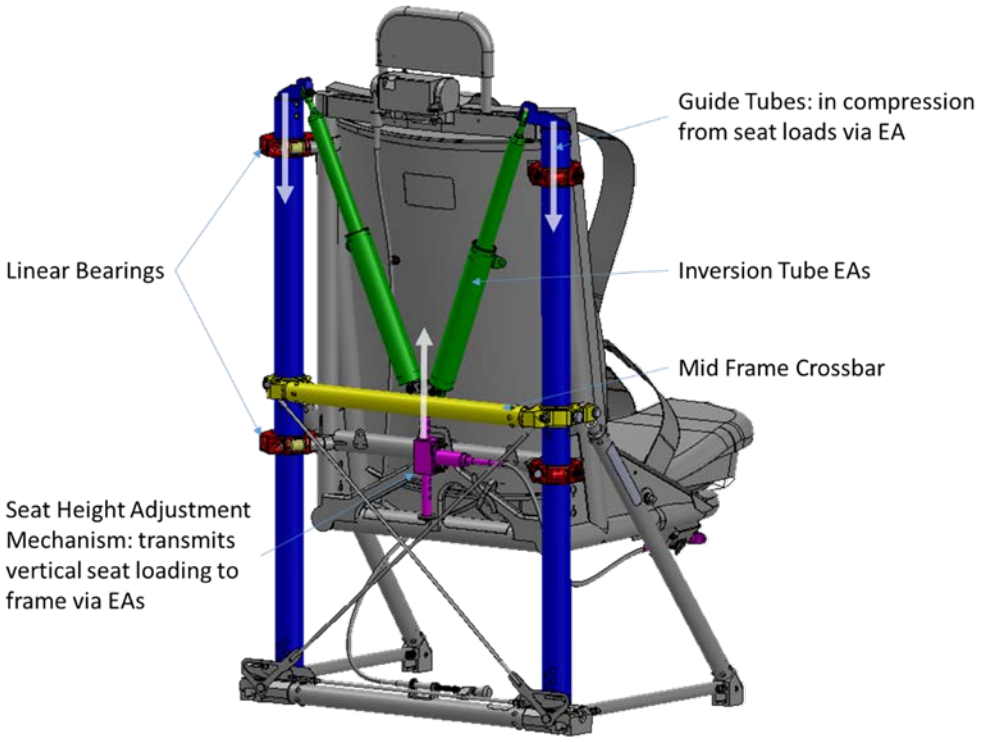

Fig. 49 MH-60R seat rear view, highlighting EA load path

Upon inspection of this design, the project team determined that the rotary MREA design could be integrated in this seat to continue to take advantage of these already proven load paths. As shown in Fig. 50, the seat height adjustment mechanism (purple in Fig. 49), which is the load path between the seat bucket and the EAs, is removed and a gear rack is connected to this point, thus preserving the loading connection to the seat bucket. The gear rack extends upward with its opposing end supported by the upper cross frame of the seat bucket. The rotary MREA is then placed just above the lower connection of the gear rack and is connected to the nonstroking seat frame by replacing the original seat's midframe crossbar (shown in yellow in Fig. 49). As notionally shown in Fig. 50, this middle crossbar can be replaced with a robust design that can support the MREA. By doing so, the EA load puts the vertical guide tubes in compression similar to the OEM configuration. While the compressive load on the guide tubes is at a lower point on the guide tubes, this should be more stable from a buckling perspective.

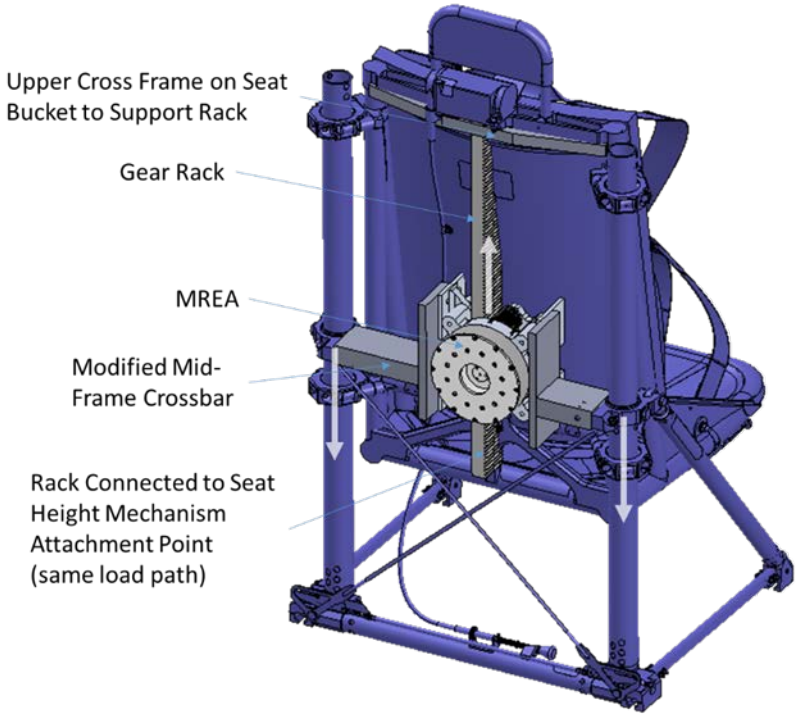

Fig. 50 MH-60R seat showing preliminary MREA integration

Due to the few modifications required for this integration concept, detailed design and structural analysis effort was significantly minimized. Primary areas remaining for structural analysis were 1) the midframe crossbar design, 2) the midcrossbar connection to vertical guide tubes, and 3) the connections of the rack to the seat bucket. These detailed designs and structural analyses were conducted in the subsequent reporting period.

3.2.1.2 Detailed Design and Structural Analysis

Figure 51 illustrates the detailed design of the MREA integration into this seat. The gear rack extends upward with its opposing end supported by the upper cross frame of the seat bucket. The rotary MREA is then placed just above the lower connection of the gear rack and is connected to the nonstroking seat frame by replacing the original seat's midcrossbar.

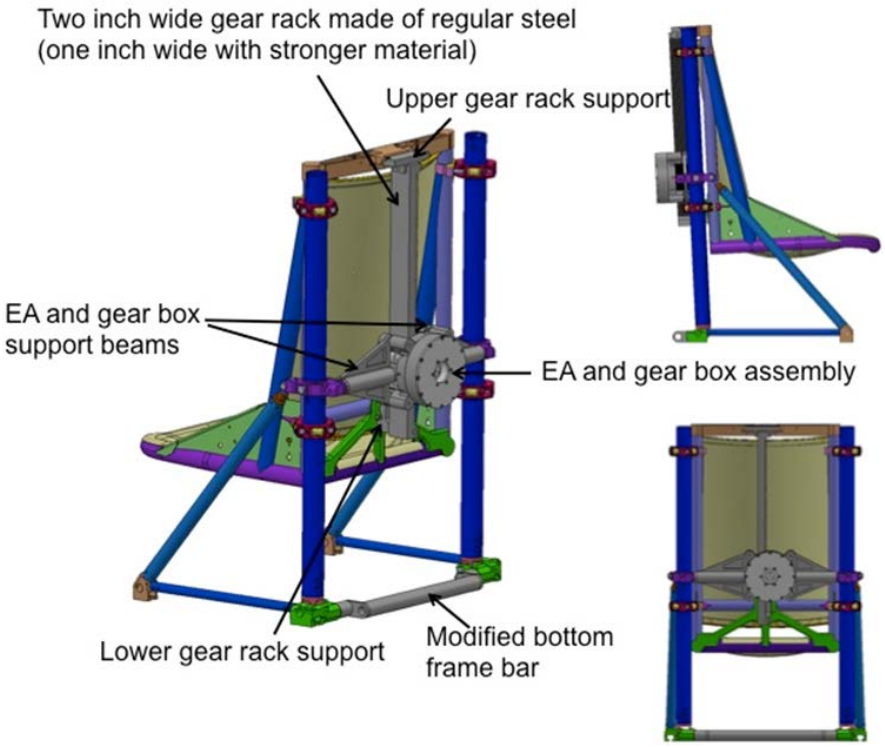

Fig. 51 Detailed design for integrating MREA into MH-60R seat

To evaluate the strength of the designed seat components, FEM analysis was conducted at the component level. The FEM model of the EA support structures is shown in Fig. 52. In this FEM analysis, the EA structure was simplified by removing all gear components and internal components in the MREA. The assumed force of 4,000 lb was applied to the EA through a simplified center pinion, and the collars at both ends of the assembly were assumed fixed. It shows that the safety factor of all areas is above 1 even the materials used in the simulation was regular aluminum alloy. The most critical area is in the collar area near the root of the support beam structure. However, the actual collar is made of stronger aluminum alloy such as 7075-T6, and this will increase the safety factor by 20% more.

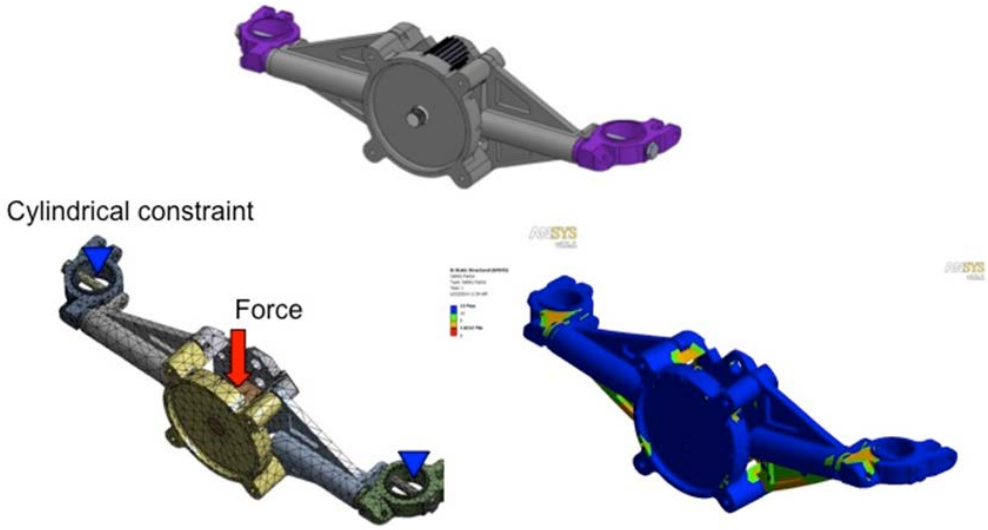

Fig. 52 FEM analysis of EA supporting structures

The strength of the gear rack and its support component was evaluated as shown in Fig. 53. In this simulation, the force of 4,000 lb was equally distributed in the gear-engaged area, and the gear rack support was assumed fixed at the connection holes. The gear rack material was assumed to be regular structural steel, and the lower and upper gear rack supports were assumed to be regular aluminum alloy. As shown in Fig. 53, the safety factor of the whole assembly is above 1.4 and the maximum deformation of the gear rack is only 0.007 inch.

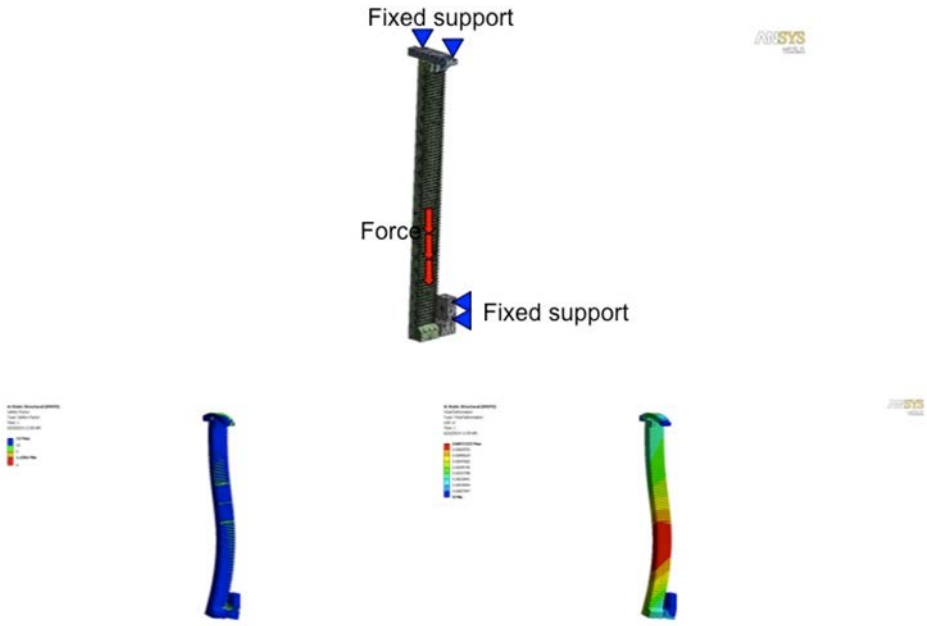

Fig. 53 FEM analysis of gear rack and its support

To ensure the strength of the seat structure was not compromised by the integration of new components, FEM simulation was conducted on the whole seat structure. In this analysis, the Joint Aircraft Survivability Program (JASP) seat structure was simplified by removing all unnecessary connecting components, gears, internal components of the EA and back panel of the seat, and by replacing the roller bearings with simplified sliding blocks. In addition, all contact surfaces in the FEM model were assumed linear (i.e., either bonded or no separation). The simplified JASP seat structure is shown in Fig. 54. The meshed model and corresponding FEM analysis results are shown in Fig. 55. In the FEM evaluation, the stroking force of 4,500 lbf (20 g's for 95th male occupant) was evenly distributed on the seat pan and the base frame was fixed. The safety factor of major load-sharing structure of the seat is above 1, confirming that the design modifications have not compromised the seat structure. The simulation does show some local contact stresses over the limit on the new integration components, which are results of simplifications in the FEM modeling that leads to excessive loading to the center pinion. However, since these components have already been determined structurally adequate in the previously detailed component analysis, these local stresses can be disregarded.

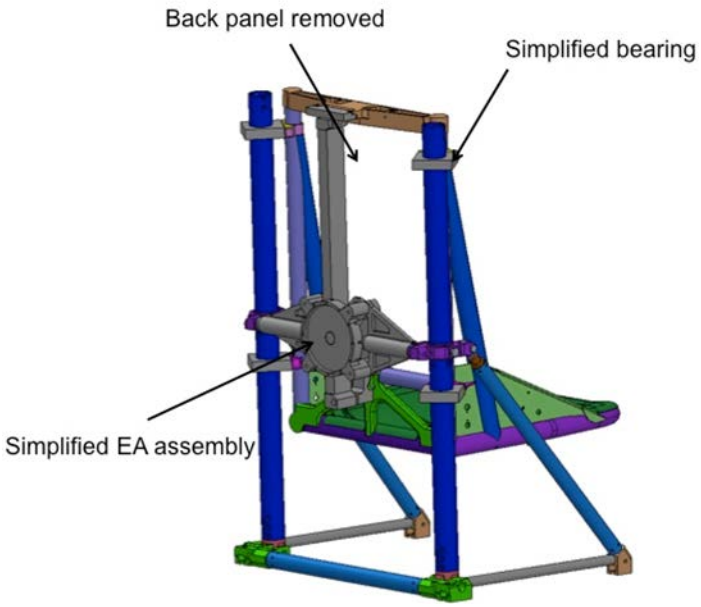

Fig. 54 Simplified JASP seat structure for FEM evaluation

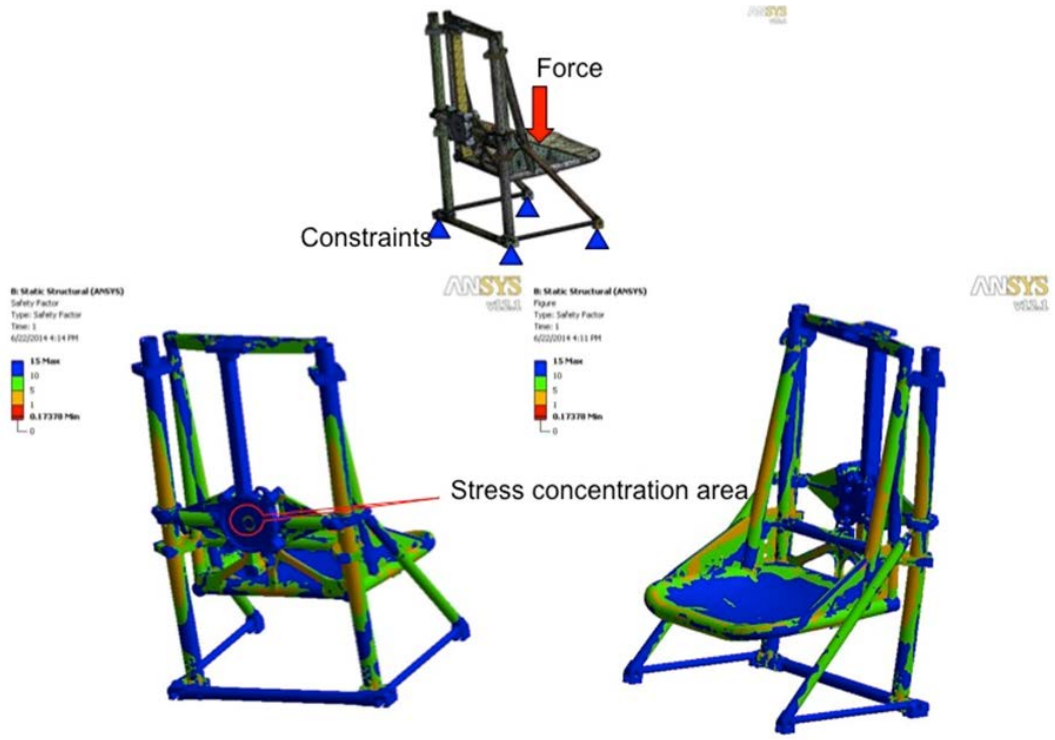

Fig. 55 FEM analysis of JASP seat structure

3.2.2 Task (b): Seat Fabrication

The JASP seat was designed based on the structure of the MH-60R seat frame and the original components in the EA's load path were replaced with redesigned parts to integrate the MREA into the seat without compromising the strength of the whole system (Fig. 56). The major components (i.e., the left and right support tubes) are made of Aluminum 6061-T6 and are used to fix the MREA to the seat vertical columns. To save time and cost, the gear rack was made of standard low-strength C1018 steel such that the width of the rack was 2 inches to ensure strength. A gear rack of high-strength (17-4 PH) stainless steel, for example, would have a face width of 1 inch and the weight of half that for a production system. For the purposes of cost savings in this phase, a custom rack was not fabricated. In addition, the upper and lower connectors were made of 7075-T6 and were used to attach the gear rack to the seat pan structure.

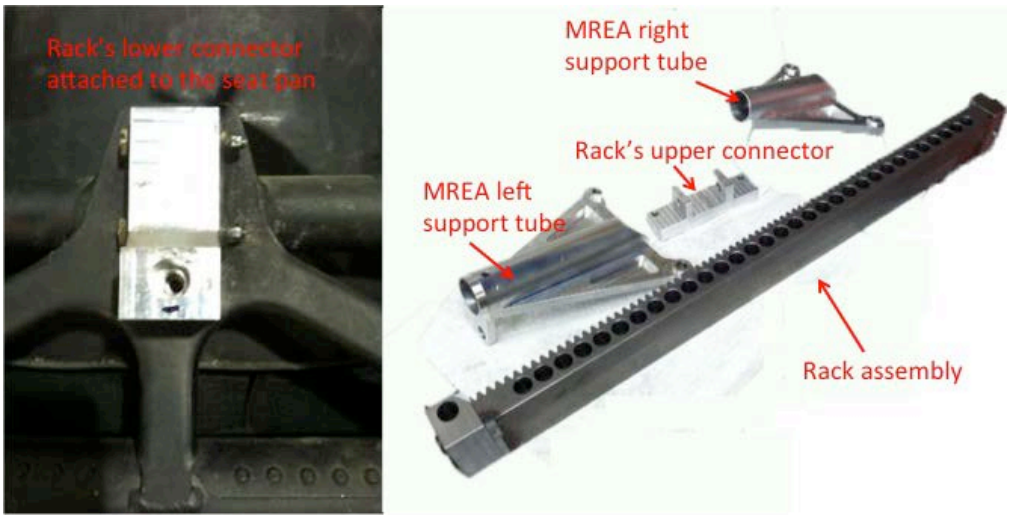

Fig. 56 Manufactured seat components for integration MREA

The iron bird test seat was assembled as shown in Figs. 57 and 58. In the seat assembly, the gear rack was attached to the seat pan structure using the rack connectors. Then, the MREA was installed in the middle position of the seat structure and attached to the seat columns using 2 support tubes. Finally, the gearbox assembly was installed by meshing the center pinion of the MREA to the gear rack through idler and reversing gears. With this configuration, the linear stroking motion of the seat pan can be transformed into the rotational motion of the pinion such that the rotary vane MREA can provide controllable damping force. One of the advantages of using the fail-safe MREA is that the seat position can be held still with the field-off condition but the seat position can be easily and continuously adjusted by applying negative current to reduce the MREA force nearly to zero. As such, the seat height adjust mechanism can be removed for additional weight savings.

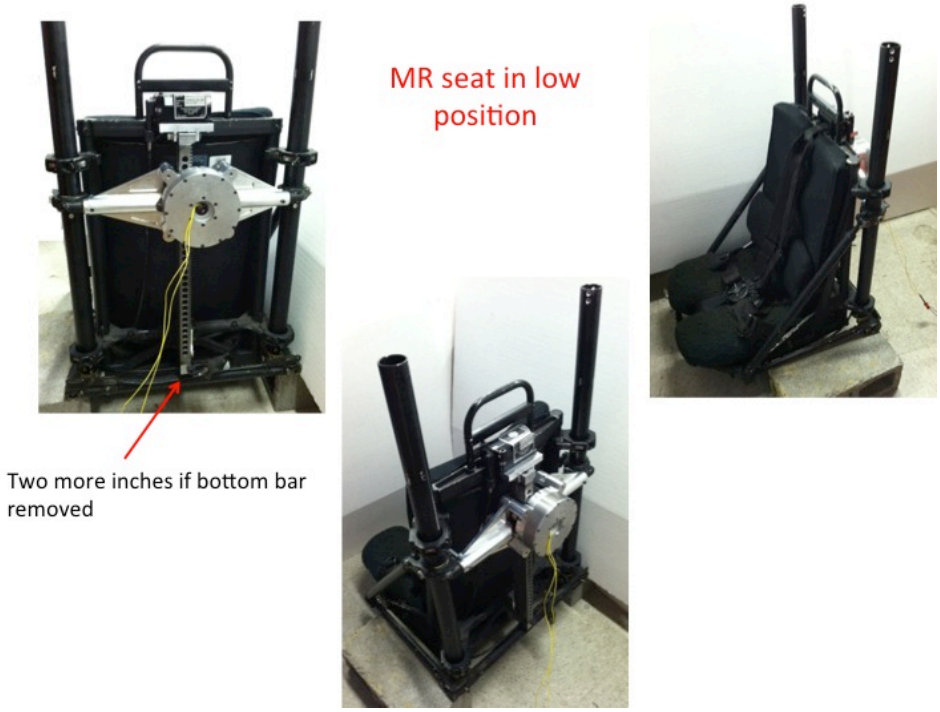

Fig. 57 Iron bird test seat with MREA: lower position

Fig. 58 Iron bird test seat with MREA: high position

In total, the MREA integrated as shown adds a net of 10 lb to the MH-60R seat. With a custom, high-strength gear rack, that weight penalty will reduce to 7 lb. Further engineering to integrate the gear rack as a structural member of the seat may prove to eliminate MREA weight penalty altogether.

4 FY2015 Accomplishments

The objectives for FY15 were to

1) Develop and integrate adaptive control for MREA and MFEA.
2) Conduct system-level full-scale dynamic testing to evaluate system performance.

Techno-Sciences, Inc. (now InnoVital Systems, Inc.), was responsible for integration of adaptive controller as well as dynamic testing. ARL-VTD was responsible for incorporating adaptive control algorithms into system-level modeling and simulation for optimizing the control algorithm prior to testing as well as test/model correlation.

4.1 Objective 1: Integration of Adaptive Control

4.1.1 Task (a): Performance Predictions from System-Level Modeling and Simulation

In the first quarter of FY15, studies on optimal passive seat were developed using a linear 2 degree-of-freedom model shown in Fig. 59. The objective of this study was to determine the optimal passive seat damper parameters, k_s and b_s, to enhance the performance of semi-active seat damper. This is a new control design methodology[14] using a Lyapunov-based approach. The linearized equations of motion of the system of Fig. 59 are

$$\dot{\mathbf{x}} = \mathbf{A}\mathbf{x} + \mathbf{L}\dot{z}_r \tag{10}$$

$$J = \lim_{T\to\infty} \frac{1}{T} E\left[\int_0^T \mathbf{x}^{\mathbf{T}} Q\mathbf{x} dt\right] = Trace\left[L\Xi L^T P\right], \tag{11}$$

where P is a solution of the following Lyapunov equation: $PA + A^T P = -Q$.

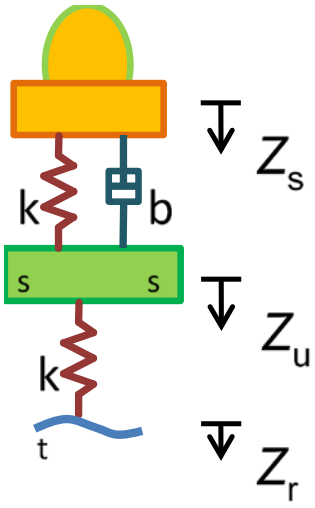

Fig. 59 Model of passive seat damper

After the calculation, the optimal k_s* and b_s* are as follows:

$$k_s^* = -\frac{m_s^2 k_t^2 \rho_2 - 2m_s m_u k_t (m_s + m_u)\rho_3 - m_s k_t^2 (m_s + 2m_u)\rho_4}{2((m_s + m_u)k_t^2 + k_t (m_s + m_u)^2 (\rho_2 + \rho_4) + (m_s + m_u)^3 \rho_3)}. \quad (12)$$

$$\left(b_s^*(k_s)\right)^2 = \frac{Num(k_s)}{kt(k_t^2 + (\rho_2 + \rho_4)(m_s + m_u)k_t + \rho_2 (m_s + m_u)^2)}. \quad (13)$$

$$\begin{aligned} Num(k_s) = {} & (m_s + m_u)k_t^2 k_s^2 + \rho_1 m_s^2 k_t^2 (m_s + m_u) + \rho_2 k_t k_s ((m_s + m_u)^2 k_s + m_s^2 k_t) \\ & + \rho_3 ((m_s + m_u)^3 k_s^2 + m_s m_u k_t (m_s k_t - 2(m_s + m_u)k_s)) \\ & + \rho_4 ((m_s + m_u)^2 k_t k_s^2 + m_s k_t^2 (m_s (k_t - k_s) - 2m_u k_s)) \end{aligned}. \quad (14)$$

Figure 60 shows the impulse velocity response of the passenger seat before and after the optimization.

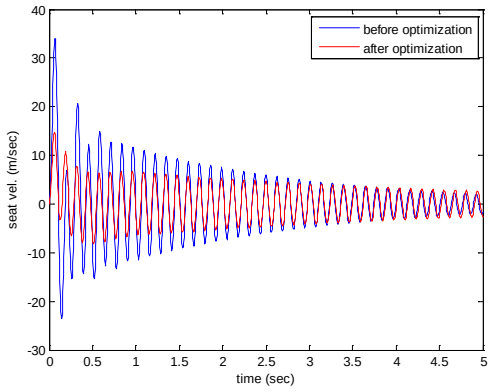

Fig. 60 Impulse response of seat: 1) before optimization (k_s = 53 kN/m, b_s =1.1 kNm/s) (blue curve) and 2) after optimization (k_s =4.98 kN/m, b_s =0.846 kNm/s) (red curve)

The project team also compared the simulation results of lumber load and control input during a helicopter crash situation for end-stop control and optimal control cases. Figure 61a shows the human body-seat interaction model in Adams software, Fig. 61b shows the lumber response comparison during the crash situation, and Fig. 61c shows the control input comparison for end-stop and optimal control. Although the lumber load responses are very similar each other, the optimal control shows much lower control input. We can deduce that the optimal model-based control is more effective than the case of end-stop control.

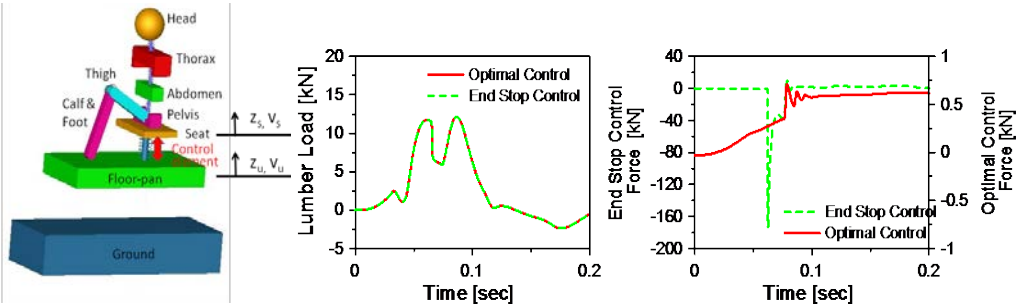

(a) Human body-seat interaction model (ADAMS)

(b) Lumber Load Simulation

(c) Control Input Simulation

Fig. 61 Adams-MatLab/Simulink co-simulation result comparison for end-stop control and optimal control

A friction EA using a self-contained hybrid electrohydraulic actuator was proposed. In this study, the feasibility of the hybrid actuator as an EA for crashworthy seats was evaluated. A simplified time-domain model was used to predict the characteristics of the actuator and EA. The effect of the pumping frequency and area ratio between the actuator and pumping pistons on the EA force and the time lag was elaborated. Some preliminary conclusions were made regarding the development of the EA using the hybrid actuator.

The proposed self-contained hybrid actuator-based EA is shown schematically in Fig. 62. In this configuration, an electrohydraulic actuator is used to pressurize the hydraulic fluid with small amplitude but high-frequency bidirectional stroke, and a hydraulic cylinder is separated by a piston into a high-pressure chamber and a low-pressure chamber. The fluid in the high-pressure chamber can be pressurized by the actuator, and an accumulator is attached to the lower-pressure chamber to maintain a constant low pressure. Two passive unidirectional reed valves are used to allow the pump to compress the fluid in the driving side of the cylinder and allow the accumulator to compensate the fluid loss in the pumping chamber. The piston in the cylinder is driven by the pressure difference across the piston such that a compression force is applied to the guide rail. Smart materials such as Terfenol-D or piezoelectric PMN-PT (lead magnesium niobate/lead titanate) can be used for

the electrohydraulic pump, and the high-frequency pumping action along with a valve system is an effective way to overcome the problem of small displacements from those smart materials. Although it is theoretically attractive to use the electrohydraulic actuator to produce controllable friction force, practical limitations such as fluid inertia, viscosity, compressibility, active material loss mechanism, and even valve dynamics can adversely reduce the efficiency of this approach. To validate the concept, a preliminary feasibility study is necessary before a real system is designed.

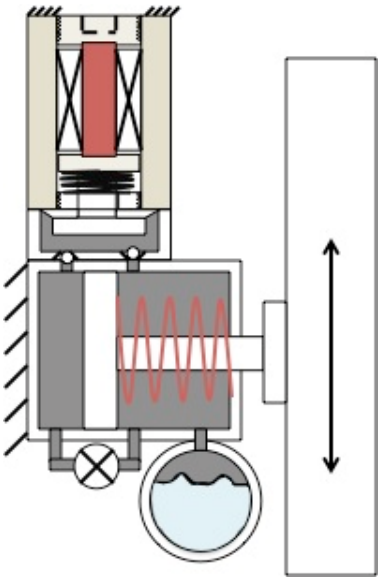

Fig. 62 Schematic drawing of hybrid actuator-based energy

Based on the comprehensive study of hybrid MS hydraulic actuators conducted by Chaudhuri et al.,[14] a simplified time-domain model was used to evaluate the behavior of the proposed system. In particular, the fluid inertia, viscosity, and compressibility combined with valve dynamics were included in the model. The relevant equations of the model are listed as follows:

$$M_a\ddot{x}_a + C_a\dot{x}_a + \left(K_d + K_s + K_a\right)x_a = K_a L_a B - P_{ch}A_{ch} \tag{15}$$

$$\dot{P}_{ch} = \beta\frac{\rho_{ch}A_{ch}\dot{x}_a - \dot{M}_{out} + \dot{M}_{in}}{\rho_{ch}A_{ch}\left(L_{ch} - x_a\right)} \tag{16}$$

$$\dot{P}_h = \beta\frac{\dot{M}_{out}}{\rho_h A_l x_l} \tag{17}$$

$$\dot{P}_{acc} = \beta_{air}\frac{-\dot{M}_{in}}{A_l\left(L_l - x_l\right)} \tag{18}$$

$$P_{ch} - P_h = \left(R_v L_v + R_t L_t\right)\dot{M}_{out} + \left(\frac{L_v}{A_v} + \frac{L_t}{A_t}\right)\ddot{M}_{out} + \frac{1}{2}\rho_{ch}\frac{K_v}{r_{out}}\left(\frac{\dot{M}_{out}}{\rho_{ch}A_v}\right) \quad (19)$$

$$P_{acc} - P_{ch} = \left(R_v L_v + R_t L_t\right)\dot{M}_{in} + \left(\frac{L_v}{A_v} + \frac{L_t}{A_t}\right)\ddot{M}_{in} + \frac{1}{2}\rho_{acc}\frac{K_v}{r_{in}}\left(\frac{\dot{M}_{in}}{\rho_{acc}A_v}\right) \quad (20)$$

$$\ddot{r}_{out} + 2\xi\omega_n\dot{r}_{out} + \omega_n^2 r_{out} = r \quad (21)$$

$$\ddot{r}_{in} + 2\xi\omega_n\dot{r}_{in} + \omega_n^2 r_{in} = r_c \quad (22)$$

In this simplified model, the fluid compressibility in the fluid passage and low-pressure chamber is neglected, fluid minor loss is only considered in the reed valve region, and the effect of the power amplifier is not considered. Equation 15 describes the dynamics of the pumping mass coupled with the material properties of the actuator, in which *B* is the field-dependent strain of the active material. Equations 16–18 are the pressure change rates in the pumping chamber, high-pressure chamber of the cylinder, and accumulator, respectively. Equations 19 and 20 determine the pressure difference between the pumping chamber and both chambers of the cylinder. Equations 21 and 22 describe the dynamics of the reed valve.

To validate the model, the simplified model in Eqs. 15–22 is modified to calculate displacement of the cylinder shaft by integrating the piston inertia into the model and removing the blocking rail guide. The simulation results are compared to the Chaudhuri's[14] results. The calculation is conducted using similar material properties and geometry size. One of the simulation examples using the model is shown in Fig. 63, and apparently the simulated result is close to the results shown in Chaudhuri et al.[14]

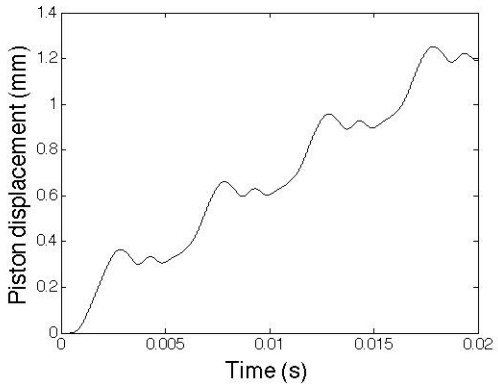

Fig. 63 Piston displacement of output shaft driven by 2-inch-long Terfenol rod at 200 Hz

Then, using the similar model parameters, this model is used to calculate the block force as the shaft is retrained by the rail guide. The simulated results are shown in Fig. 64, in which the valve dynamics, fluid inertia, compressibility, and viscosity are not considered in the ideal system while the real system includes the effect of the fluid and valve. This calculation is based on a 200-Hz pumping motion and 50-psi accumulator pressure. As shown in Fig. 64a, the block force in both ideal and real systems can reach 190 lb using an actuation piston of 0.75 inch in diameter, and this force is nearly 10 times higher than the block force (20 lb) estimated using the experimental velocity-load curve as shown in Chaudhuri et al.[14] Nonlinear effect near zero velocity and leakage in the system may lead to the discrepancy. Thus, the simulation model probably can overpredict the block force. In addition, it takes 38 ms for the ideal system and 75 ms for the real system to reach the full force level. If the natural frequency of the reed valve is reduced by 50%, the time delay becomes much longer than the one using the valve with higher natural frequency. As such, the performance of the electrohydraulic EA can be greatly affected by the dynamics of the valve system. The simulated reed valve opening, pressure variation, and strain level in the active material are shown in Fig. 64b, c and d, respectively.

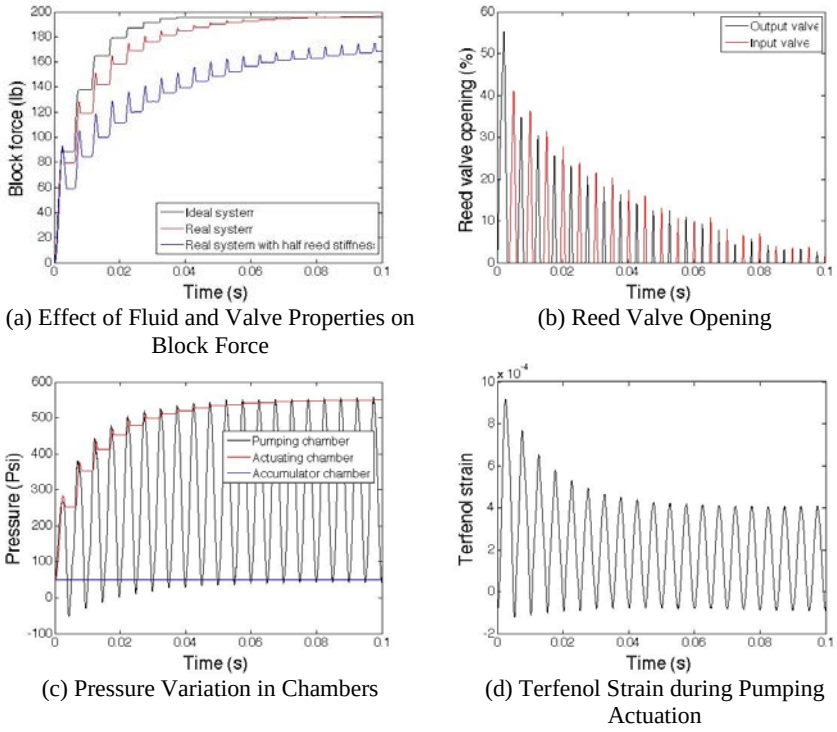

(a) Effect of Fluid and Valve Properties on Block Force

(b) Reed Valve Opening

(c) Pressure Variation in Chambers

(d) Terfenol Strain during Pumping Actuation

Fig. 64 Behavior of electrohydraulic EA using 200-Hz pumping frequency and 50-psi accumulator pressure

Using the simulation model, the block force as a function of the applied field on the active material is shown in Fig. 65, in which the pumping frequency is 200 Hz and the accumulator pressure is 50 psi. The block force can be varied with the application of different excitation levels and the time lag can be decreased as the force level is lower. Since the required EA force for a crashworthy seat is as high as 3,000 lb, the actuation piston diameter is increased to 3 inches, and the corresponding block force is calculated using the same Terfenol rod, pumping frequency, and accumulator pressure (Fig. 66). Apparently, the comparable force level can be reached using a larger actuation piston area, but the time required to reach the required force level is more than 200 ms. The other option to increase block force is to use larger active material, but this option is also limited by the capacity of a high-frequency power amplifier. The effect of the pumping frequency on the block force does not significantly affect the amplitude and time lag of the block force (Fig. 67). The effect of the accumulator pressure is shown in Fig. 68. Since the increase of the accumulator pressure can increase the bulk modulus of the fluid, the block force level in a higher accumulator pressure can reach the similar force much faster (i.e., from 75 to 18 ms) than the EA using a lower accumulator pressure.

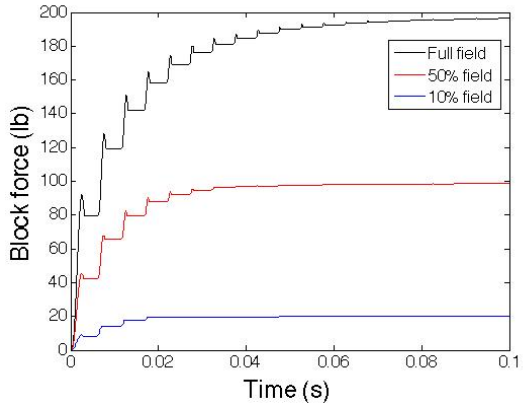

Fig. 65 Block force variation as a function of applied field

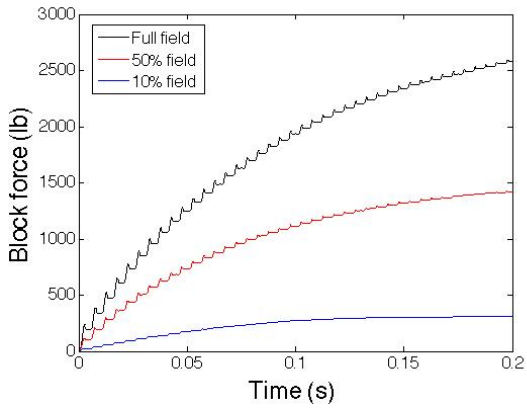

Fig. 66 Calculated block force with actuation piston of 3 inches in diameter

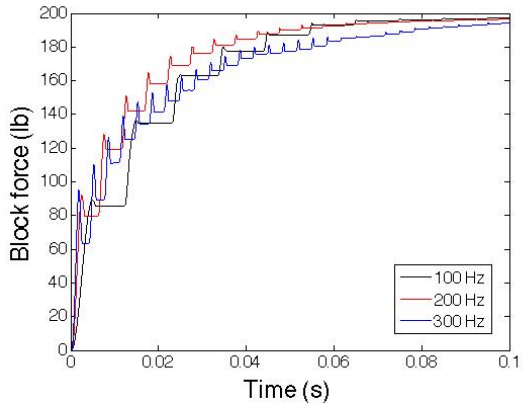

Fig. 67 Effect of pumping frequency on block force

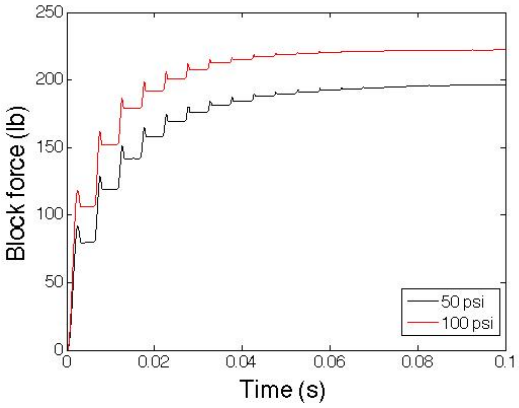

Fig. 68 Effect of accumulator pressure on block force

Based the simulation results, we can make several preliminary conclusions regarding the use of electrohydraulic actuator in an EA:

1) The self-contained electrohydraulic actuator can be used to change the compression force in a friction EA.

2) The required force level for a crashworthy seat can be obtained by using a larger piston diameter and/or larger active materials.

3) However, the control of the compression force using the electrohydraulic actuator in a crash event is difficult since the time lag for the actuator to reach the desired force level is usually in the level of tens or even hundreds of milliseconds.

4) The dynamics of the reed valve is critical for improving the performance of the electrohydraulic actuator.

The time lag of the force could be reduced with the increase of the accumulator pressure and bulk modulus of the fluid, but the effect of the pumping frequency is not significant.

The project team conducted simulation of human body response during helicopter crash situation for original damper, optimal passive damper, and optimal control of the damper cases and compared the lumber load of those cases. Figure 69a shows the human body-seat interaction model in Adams software, Fig. 69b is the block diagram of active control for MatLab/Simulink program, and Fig. 69c shows a simulation result. The original damper showed a higher lumber load at the first peak. The optimized passive damper weakened the stiffness and damping coefficient, resulting in a lower lumber load at the first peak; however, the second peak shoots up due to the secondary rebound of the seat. The optimal control of

the seat damper makes the first and second peak even. The lumber load from the optimal control is very similar with the result from the prior semi-active end-stop control result.

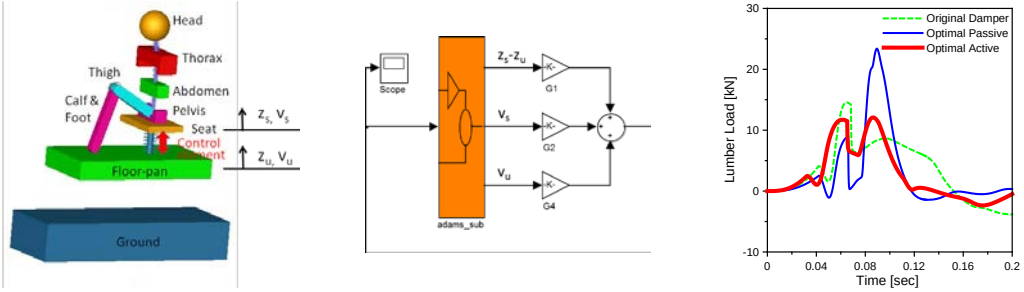

(a) Human body-seat interaction model (ADAMS)

(b) Block diagram for optimal control

(c) Co-simulation result

Fig. 69 Adams-MatLab/Simulink co-simulation control flow diagram for optimal control and a control simulation result

The project team conducted detailed simulations with finite element crash dummy models to predict the human body response during helicopter crash events for the cases of passive damper and adaptive controlled damper. The occupant lumbar loads were compared for the 2 types of damper cases. Figure 70 shows the detailed finite element seat-occupant system-level model that was previously developed. Figure 71 shows the adaptive EA load-stroke profile that was used for analysis. For the case of 50th percentile male, the permanent magnet design in the fail-safe adaptive damper would provide the required fixed EA force for the maximum vertical crash sink rate of 42 ft/s (dV). A feedback controller developed for this project would enable a variable EA load-stroke profile that is continuously adjustable. It provides a feedback controlled damper load based on occupant weight, crash severity, and available seat stroke. Figure 72 shows the dynamic seat stroke and lumbar force responses for 5th percentile female Hybrid III ATD and 95th percentile Hybrid III ATD models. Overall, the model predicts it is feasible to keep the lumbar forces within the IARVs for all the 3 occupant cases (5th percentile female, 50th percentile male and 95th percentile male) with the adaptive rotary fail-safe magnetorheological energy absorber (FSMREA) load-stroke profiles as shown in Fig. 71.

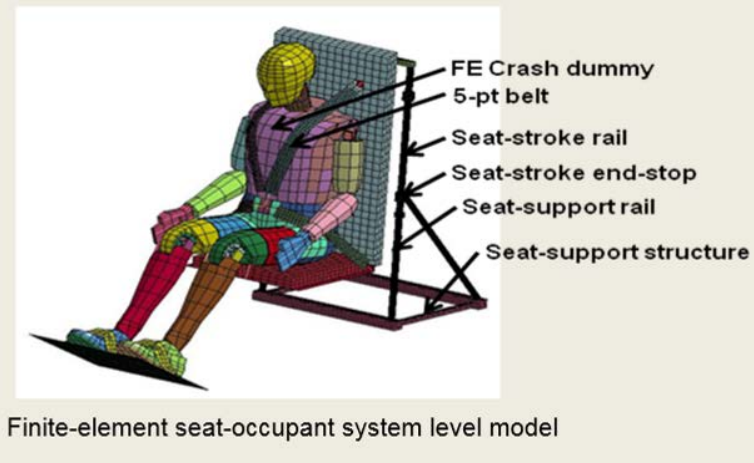

Fig. 70 Finite element seat-occupant model

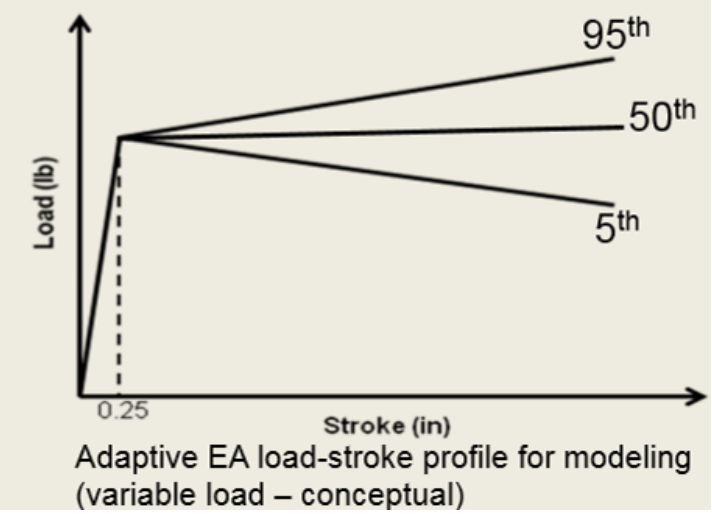

Fig. 71 Adaptive EA load-stroke profile for modeling (for 50th percentile male, the fixed-load level EA is adjusted using permanent magnet design in the rotary FSMREA developed for this project)

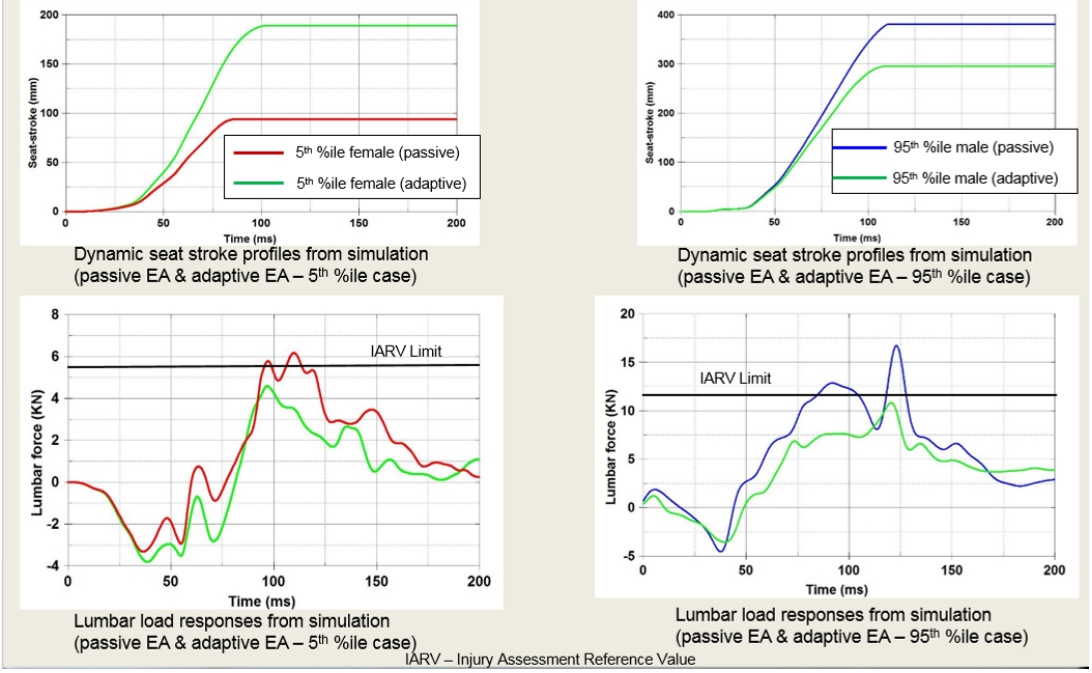

Fig. 72 Dynamic seat stroke and lumbar force profiles during crash simulation (for passive and adaptive EA cases)

4.1.2 Task (b): Control Electronics Development

4.1.2.1 Hardware and Software Design

Upon completion of electronics hardware design, InnoVital Systems fabricated and assembled the printed circuit board (PCB) for the integrated control electronics. Figure 73 shows the fabricated PCB with major items identified. Power input on the left side of the board is filtered to protect the circuit from voltage transients associated with vehicle power (MIL-STD-704[15]). After being regulated down to working voltages for the various components, the lines are filtered for electromagnetic interface. A digital signal processor reads sensor signals from on-board micromechanical systems accelerometers as well as an external sensor (displacement or force). Using these measurements, the control algorithm determines the desired applied electrical current to the MREA and outputs a pulse-width modulation (PWM) signal via the H-bridge circuit to the MREA. Embedded software code has been developed for reading sensor inputs and outputting PWM signals for processing control algorithms. In addition to this, the team has completed mechanical packaging of the PCB as shown in Figs. 74 and 75. The control algorithm flowchart is shown in Fig. 76.

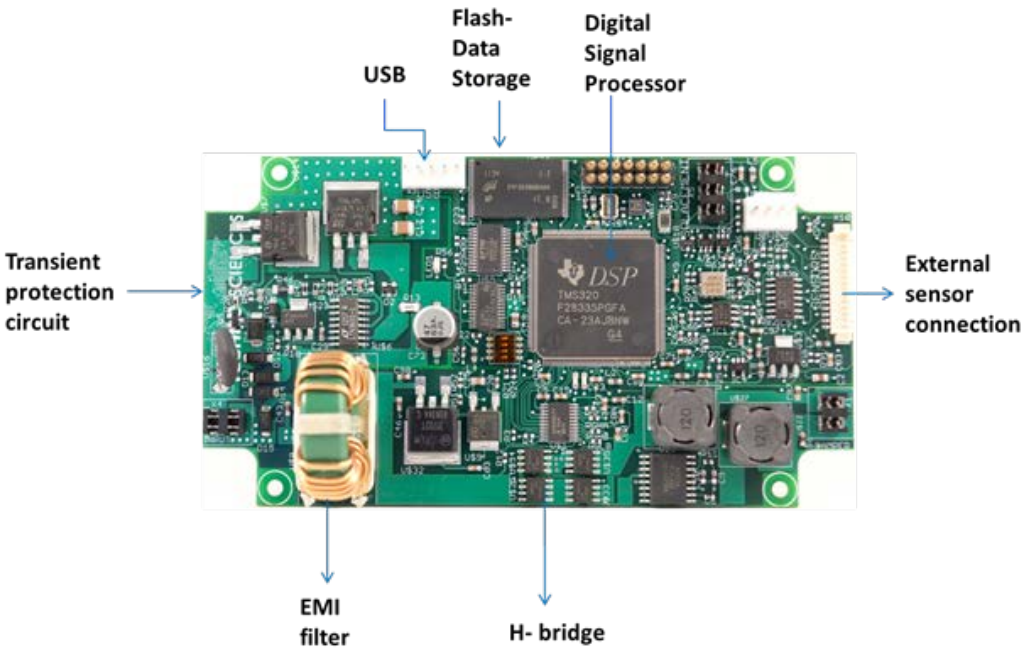

Fig. 73 PCB for integrated control electronics

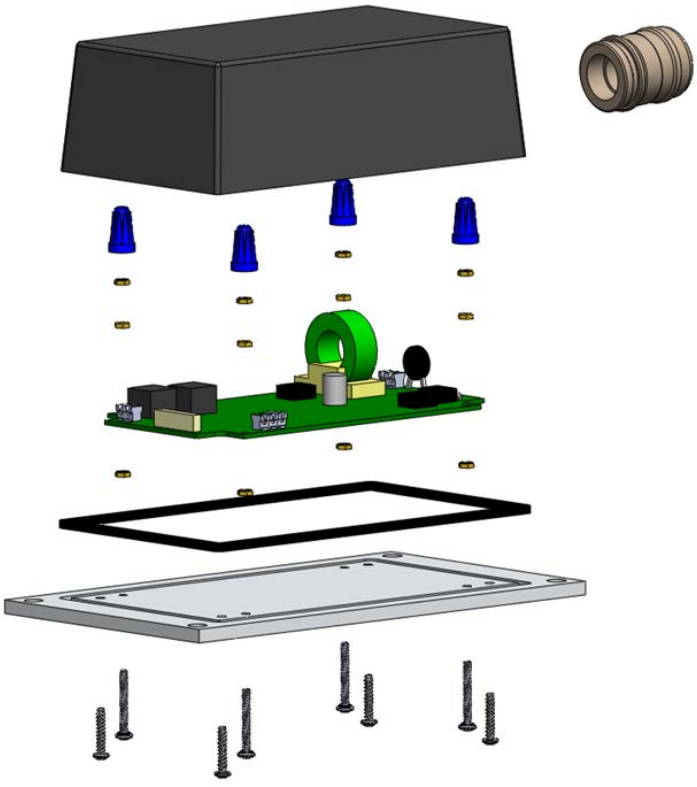

Fig. 74 Exploded view of integrated control electronics mechanical packaging

Fig. 75 PCB integrated into mechanical packaging

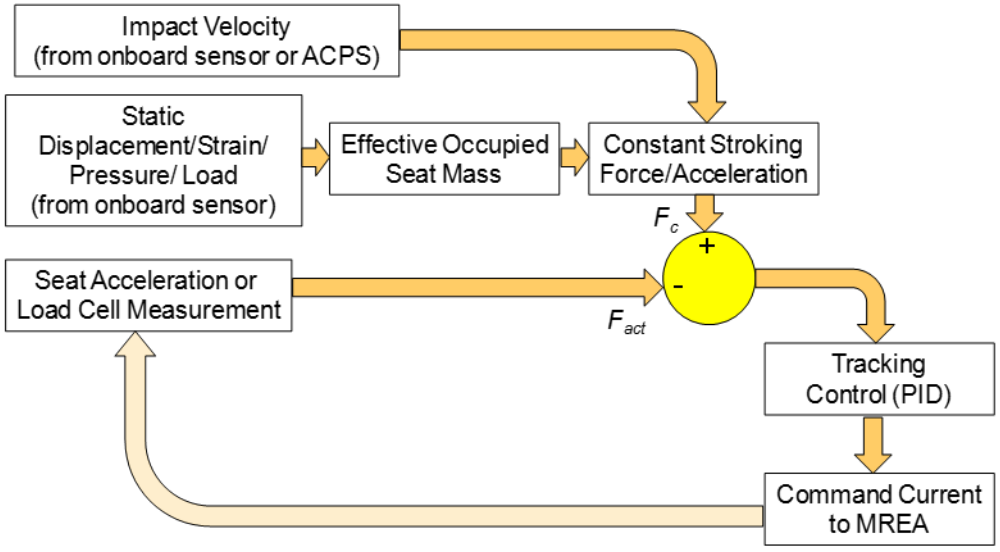

Fig. 76 Control algorithm flowchart

4.1.2.2 Seat Integration

The team has designed a mounting bracket for attaching the control electronics module to the test seat for full-scale testing. Detailed design drawings have been developed and the bracket has been fabricated by a local machine shop.

4.2 Objective 2: Full-Scale Dynamic Testing

Under this objective, the program team planned and conducted full-scale dynamic tests to demonstrate ASEA performance. The primary performance metric was lumbar compressive load with target values lower than conventional EA (passive) seat for all load cases. A further goal was to comply with injury criteria as stipulated in Full Spectrum Crashworthiness Criteria published by AMRDEC/AATD: Lumbar load limits of 933 lb for Hybrid III 5th percentile small female; 1,395 lb for Hybrid III 50th percentile male; and 1,757 lb for 95th percentile large male.

To begin this effort, the team developed a test plan for full-scale sled testing with a goal of demonstrating the ASEA performance against a fixed load EA across a range of impact velocities and occupant sizes. The test plan is included as Appendix A and accompanying Appendixes B–F and consists of 10 pure vertical dynamics tests, half of which are with the seat in a baseline configuration (fixed load EA for reference data) and half of which are with the ASEA. ASEA tests were conducted first in increasing levels of severity to maximize the number of tests before a potential hardware failure. Should the full set of baseline tests not be able to be conducted (due to hardware failure, etc.), results from Richards and Podob[16] were to be used as reference values. Testing was originally planned to take place at MGA Research in Manassas, Virginia. However, MGA Research was unable to provide these services due to limitations of their facility. As an alternate, Naval Air Warfare Center Aircraft Division's (NAWCAD's) Horizontal Accelerator (HA) Laboratory was engaged.

Testing at NAWCAD's HA Laboratory commenced on the week of 7 December 2015. The first test was conducted with a 50th percentile male ATD and a crash velocity of 21 ft/s. Figures 77 and 78 show the pre- and posttest photos of the seat, respectively, for test no. 1. Figures 79 and 80 show the lumbar load the seat stroke response for test no.1. The peak lumbar load was recorded to be 891 lb, which is well within the aforementioned lumbar load limits and 35% lower than the value of 1,372 lb in a published study for the baseline seat.[4] Moreover, the ASEA-retrofit seat only used 3.0 inches of stroke, which is 10% lower than the baseline seat. As such, the ASEA significantly improved crash safety and was more stroke efficient.

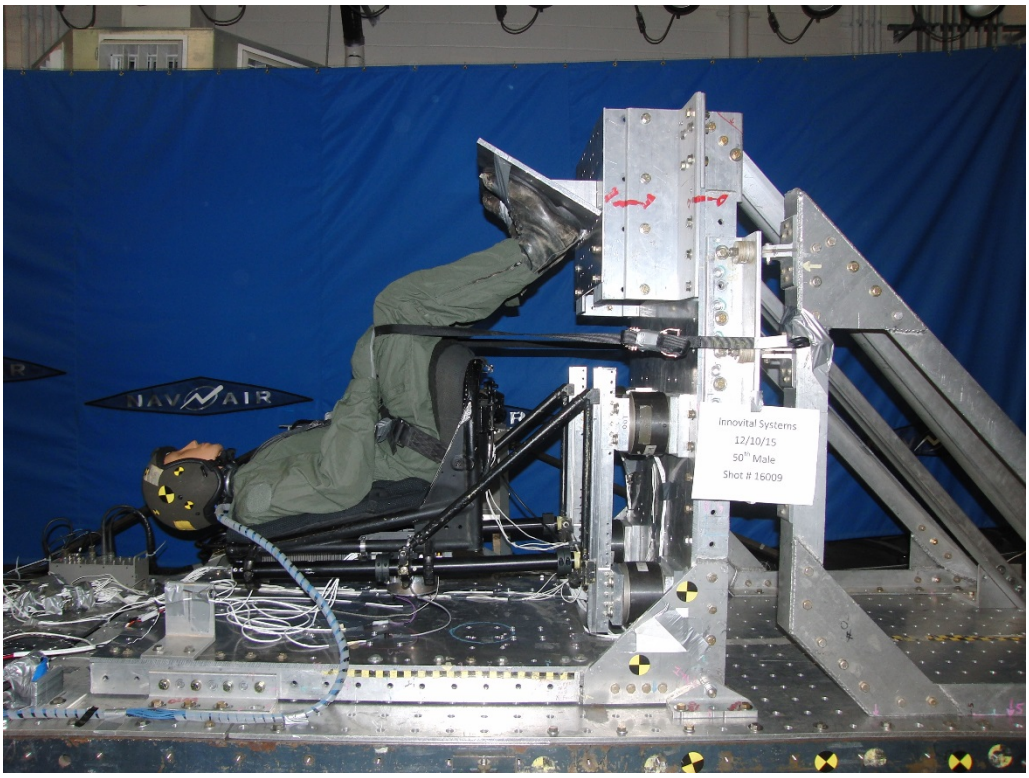

Fig. 77 Pretest photo for test no. 1, 50th percentile male occupant and 21 ft/s crash velocity

Fig. 78 Posttest photo for test no. 1, 50th percentile male occupant and 21 ft/s crash velocity

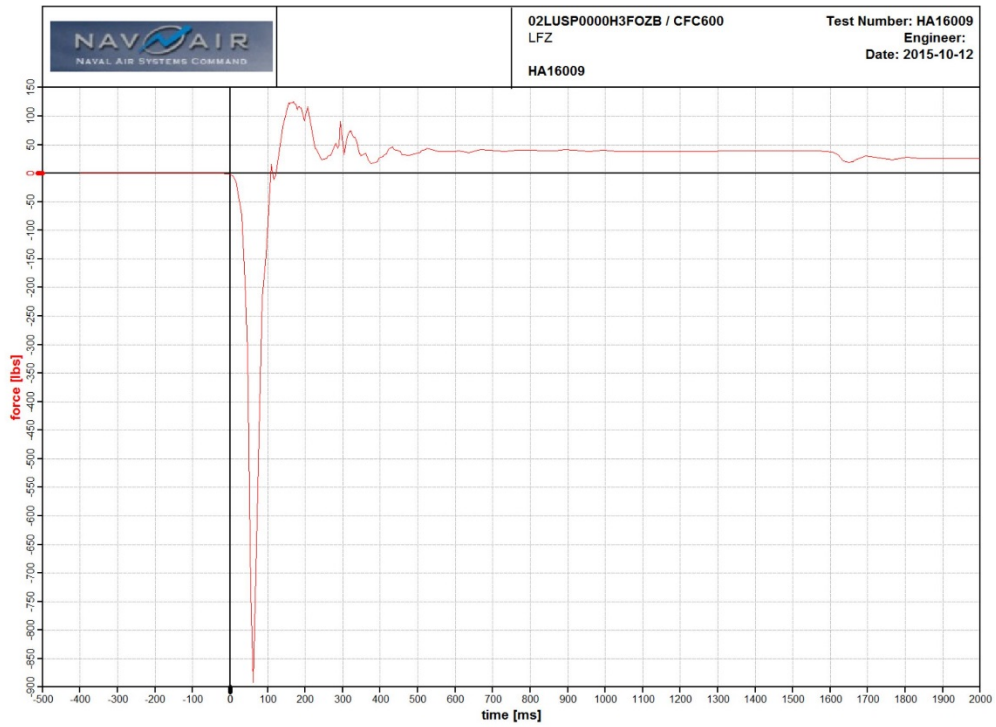

Fig. 79 Lumbar compressive load for test no. 1, 50th percentile male and 21 ft/s crash velocity

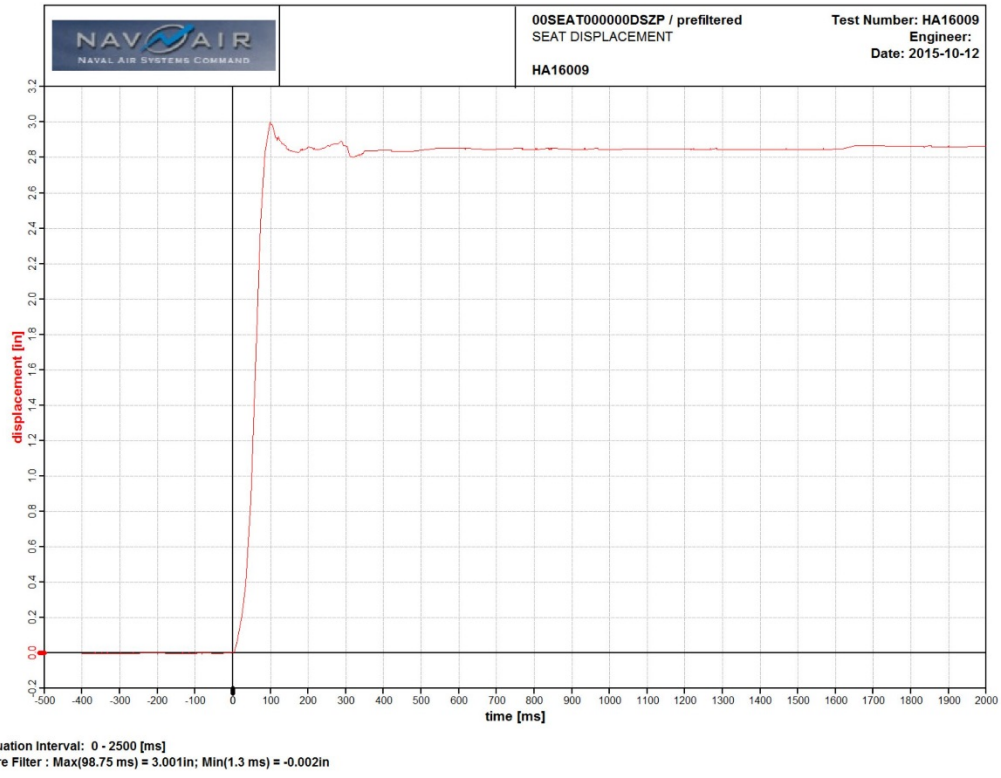

Fig. 80 Seat stroke for test no. 1, 50th percentile male and 21 ft/s crash velocity

The second test was then conducted with a 50th percentile male ATD and crash velocity of 34 ft/s. Figures 81 and 82 show the pre- and posttest photos, respectively, for test no. 2. Figures 83 and Fig. 84 show the lumbar load the seat stroke response for test no. 2. The peak lumbar load was recorded as 1,773 lb, which is slightly higher than the aforementioned lumbar load limits and 32% lower than the value of 2,610 lb in a published study for the baseline seat.[4] Moreover, the ASEA-retrofit seat only used 3.8 inches of stroke, which is 61% lower than the baseline seat. As such, the ASEA significantly improved crash safety and was more stroke efficient. The project team believes that further controller tuning would enable the ASEA to use more of the available seat stroke and further reduce lumbar loads.

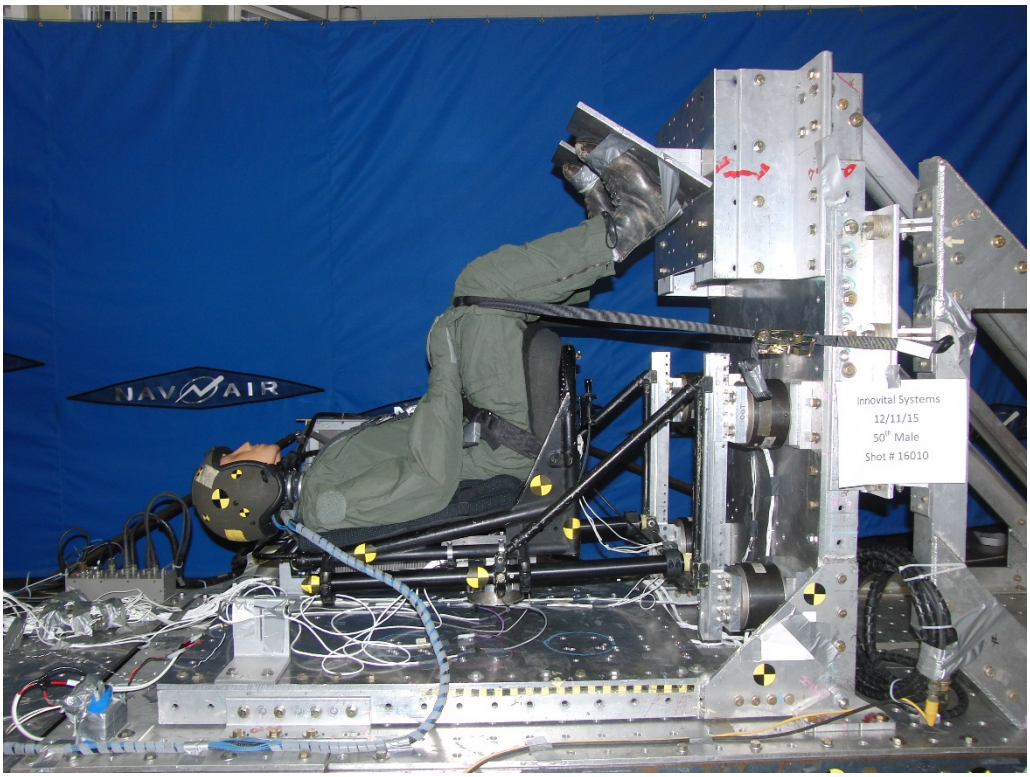

Fig. 81 Pretest photo for test no. 2, 50th percentile male occupant and 34 ft/s crash velocity

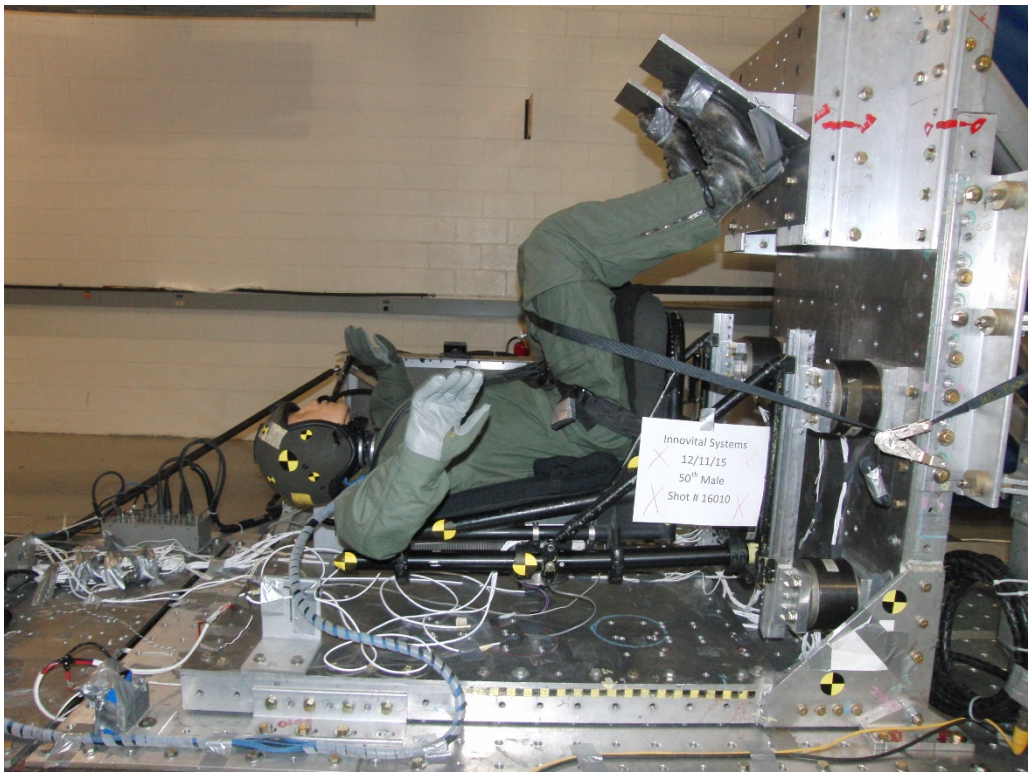

Fig. 82 Posttest photo for test no. 2, 50th percentile male occupant and 34 ft/s crash velocity

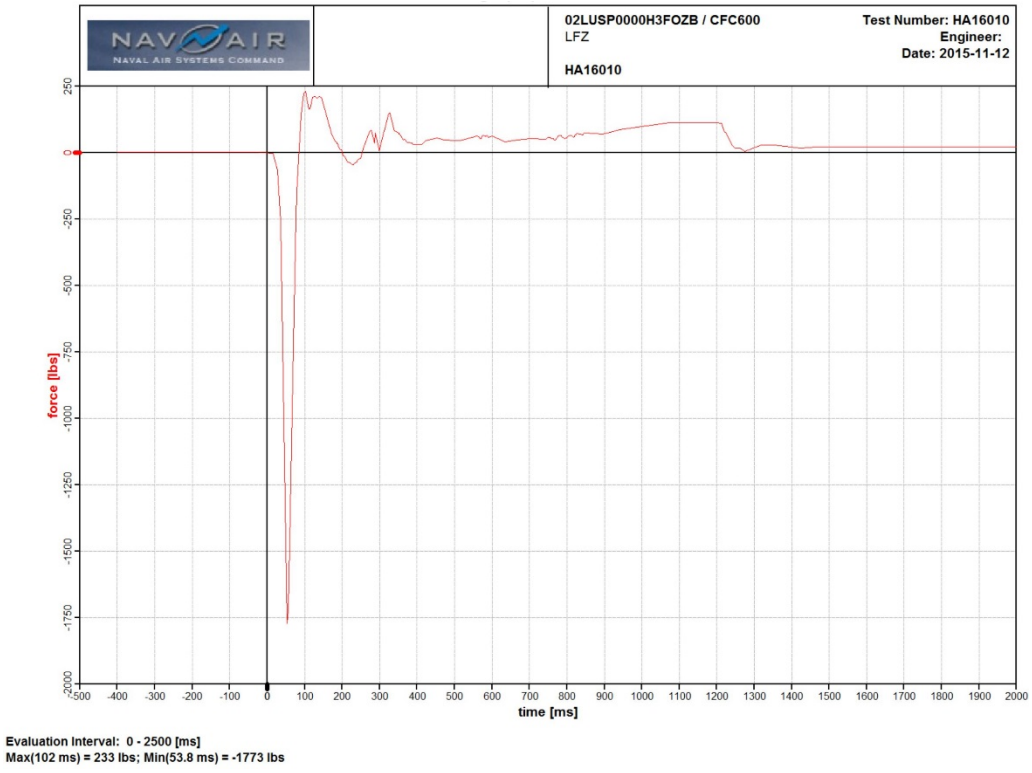

Fig. 83 Lumbar compressive load for test no. 2, 50th percentile male and 34 ft/s crash velocity

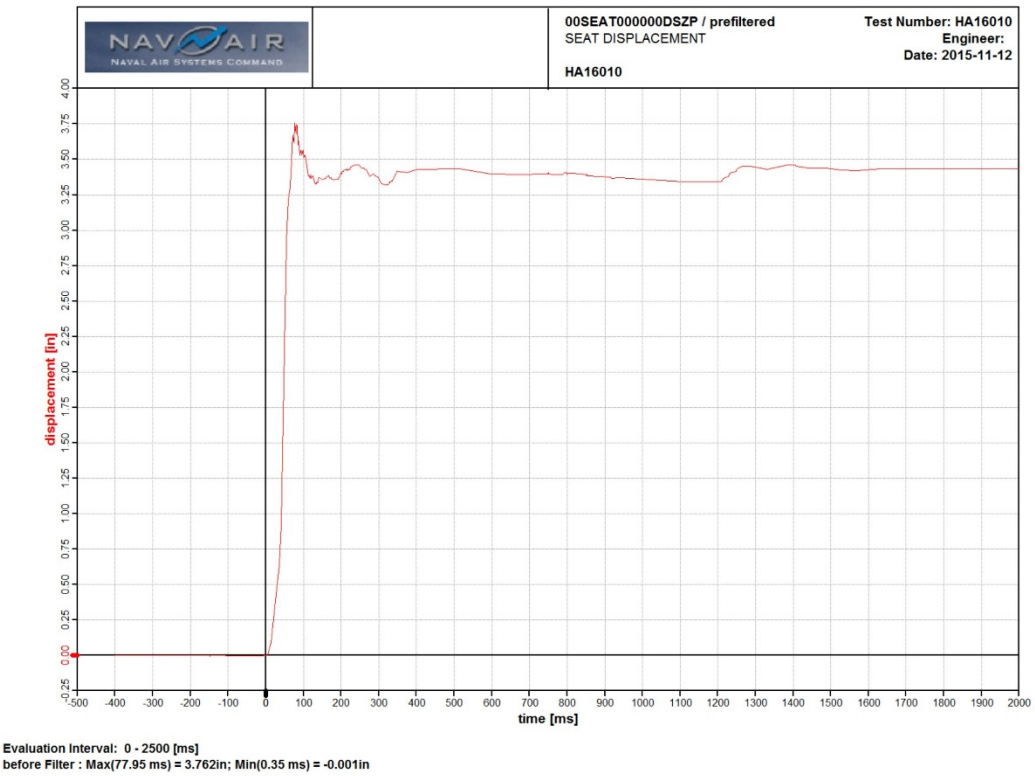

Fig. 84 Seat stroke for test no. 2, 50th percentile male and 34 ft/s crash velocity

The third test conducted was with a 50th percentile male ATD and crash velocity of 42 ft/s. In this test, a structural seat failure occurred. Figures 85 and 86 show the pre- and posttest photos for test no. 3, respectively. As shown in Figs. 87 and 88, in this testing, the top crossbar and headrest completely detached from the seat pan. This failure started with the failure of a load cell to monitor the MREA loads, which redirected the load path in an unplanned fashion. Due to this structural failure, no usable data were collected from this test.

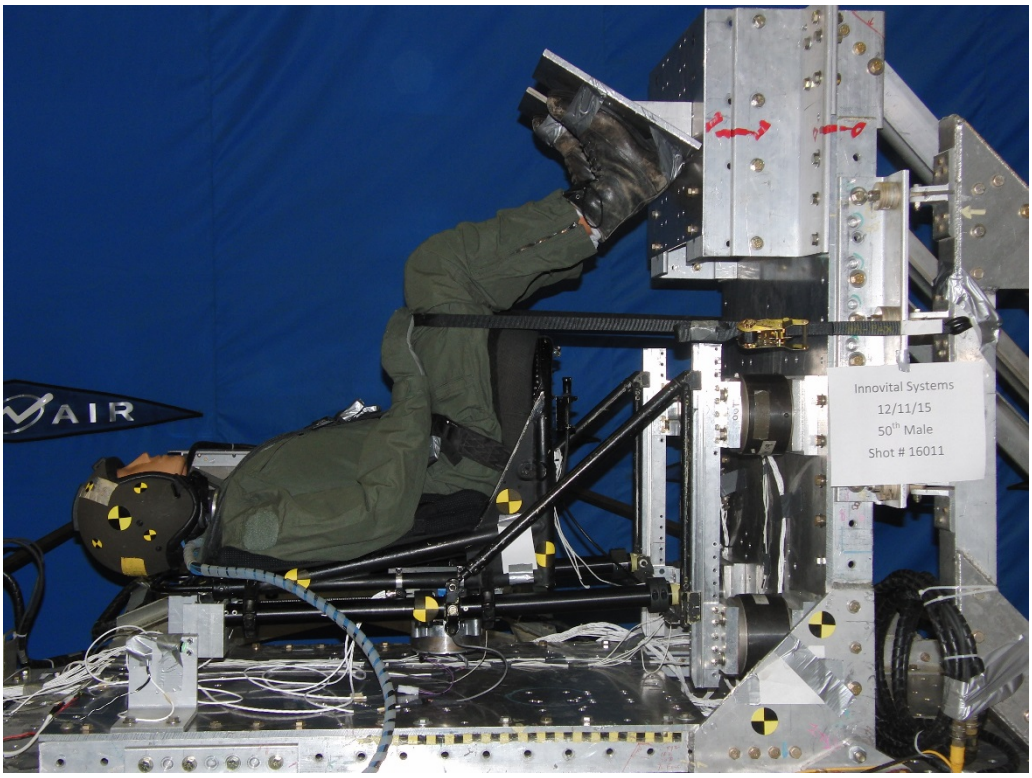

Fig. 85 Pretest photo for test no. 3, 50th percentile male occupant and 42 ft/s crash velocity

Fig. 86 Posttest photo for test no. 3, 50th percentile male occupant and 42 ft/s crash velocity

Fig. 87 Posttest photo for test no. 3 showing top crossbar broken off of seat back

Fig. 88 Posttest photo for test no. 3 showing top crossbar and headrest completely free from seat back

The team then repaired the seat with spare parts and conducted test no. 4, a retest of the test no. 3 conditions. Figures 89 and 90 show the pre- and posttest photos for test no. 3, respectively. As shown in Figs. 91 and 92, in this testing, the diagonal seat pan support cracked. This failure was likely due to the nonstroking seat frame being stiffer with the MREA than for the baseline seat. Because the nonstroking seat frame did not flex as much as in the baseline configuration, greater load was transferred to the seat pan, causing it to fail. Due to this structural failure, no usable data were collected from this test. Moreover, because there were no further seat pan spares to use, testing was halted prematurely. While the full test series was not able to be completed, the results obtained from the first 2 tests clearly show great promise for the MREA technology and met the program objectives of demonstrating lower lumbar loads as compared to conventional EAs.

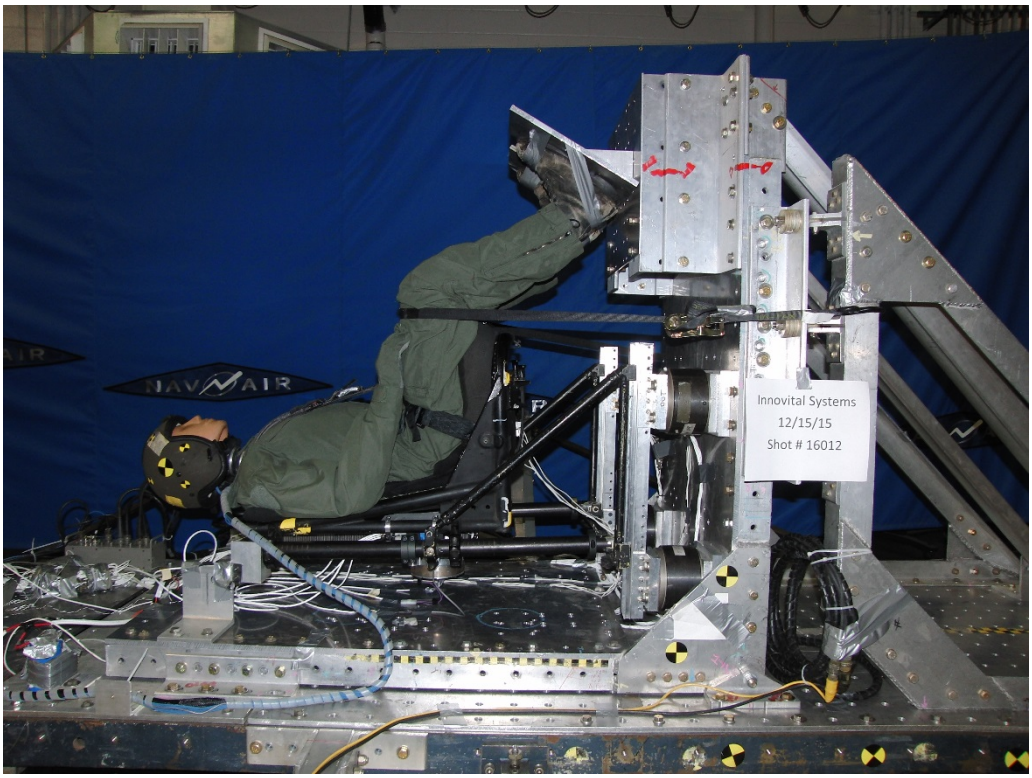

Fig. 89 Pretest photo for test no. 4, 50th percentile male occupant and 42 ft/s crash velocity

Fig. 90 Posttest photo for test no.4, 50th percentile male occupant and 42 ft/s crash velocity

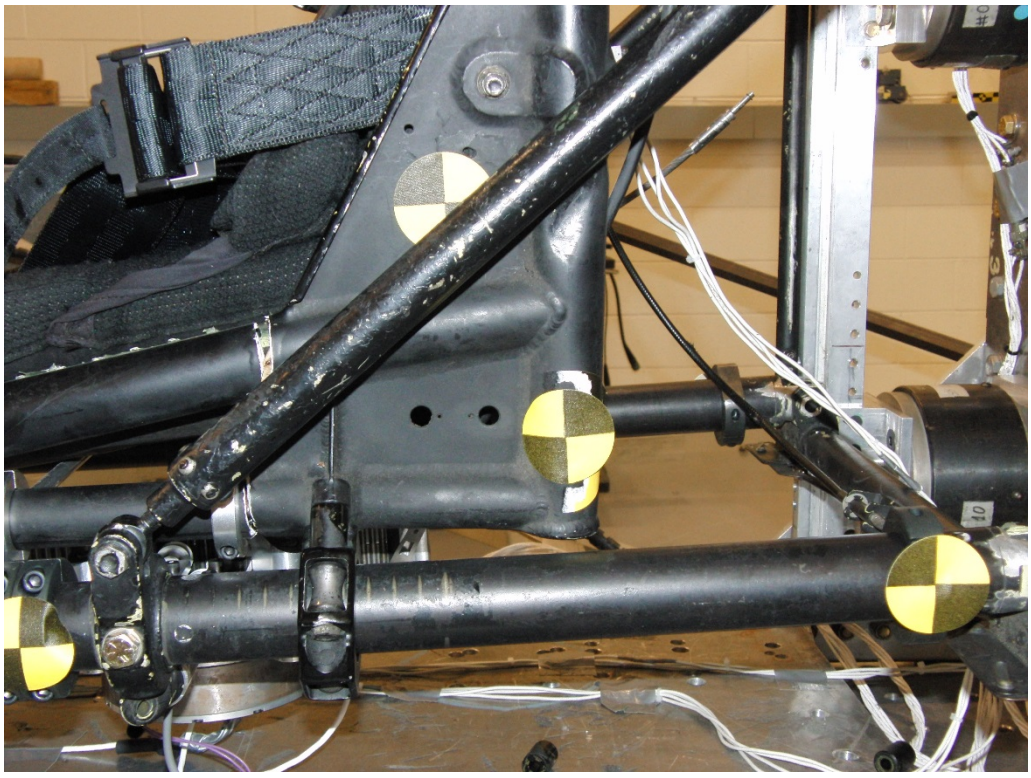

Fig. 91 Posttest photo for test no. 4 showing broken seat pan

Fig. 92 Posttest photo for test no. 4 showing close-up of broken seat pan

4.3 Objective 3: Final Report Preparation and Completion

The submittal and publication of this final report in Defense Technical Information Center Survivability/Vulnerability Information Analysis Center marks the successful completion of this objective and of this program.

5. Conclusions and Recommendations

This final report has documented the technical progress on the Adaptive Seat Energy Absorbers for Enhanced Crash Safety program sponsored by JASPO project number V-13-02. The period of performance of this effort was from 1 October 2012 through 29 February 2016.

This research program was intended to design, assemble, and test both at a component and assembly level, ASEA technology to retrofit a rotorcraft crew seat. The final product of this program was intended to be a prototype ASEA system that has been evaluated for enhanced crash safety performance. In the first year of the program, 2 ASEA technologies, an MREA and MFEA, were designed and evaluated at a component level. Only the MREA was found to meet program objectives and was therefore down-selected for the remainder of the program. In the second year of the program, the MREA was successfully retrofitted into an MH-

60R seat. In parallel with this, modeling and simulation was conducted to evaluate adaptive control algorithms. Then, in the third year of the program, the MREA was integrated with control electronics for enacting adaptive control algorithms and further simulations were conducted. Full-scale dynamic crash testing was planned to evaluate the ASEA technology across a range of crash velocities and occupant weights. The first 2 tests conducted showed great promise for the ASEA technology, with compressive lumbar loads measured to be more than 32% lower than published data for the baseline MH-60R seat with conventional EAs. Moreover, the ASEA used substantially less stroke than the baseline seat, showing that the ASEA can be much more efficient. Unfortunately, however, structural failures on the seat prevented the full matrix of dynamic tests from being conducted.

Given the promise shown in these initial dynamic tests and the fact that further tuning of the adaptive control algorithm will likely improve performance, the project team recommends continuation of investment into the ASEA technology. Seat integration and structural issues can be addressed and new seat hardware can be purchased such that the testing series can be completed. As an alternative, a simplified SDOF test setup may be constructed to evaluate the ASEA technology in a more cost-effective manner.

6. References

1. MIL-S-58095A: Seat system: crash-resistant, non-ejection, aircrew, general specification for. Washington (DC): Army Aviation Systems Command (US); 1986 Jan 31.

2. Desjardins SP, Zimmerman RE, Bolukbasi AO, Merritt NA. Aircraft crash survival design guide vol. IV – aircraft seats, restraints, litters, and cockpit/cabin delethalization. Fort Eustis (VA): Aviation Applied Technology Directorate; 1989. USAAVSCOM Technical Report No.: 89-D-22D. p. 45–58, 83–109, and 165.

3. JSSG-2010-7. Crew systems crash protection handbook. Wright-Patterson AFB (OH): Department of Defense; 1998 Oct 30.

4. Etrema Products, Inc. Terfenol-D physical properties. Ames (IA): Etrema Products, Inc. http://www.etrema.com/terfenol-d/.

5. Crandall SH, Dahl NC, Lardner TJ. An introduction to the mechanics of solid, second edition with SI units. New York (NY): McGraw-Hill; 1978.

6. Boileau PÉ, Rakheja S. Whole-body vertical biodynamic response characteristics of the seated vehicle driver, measurement and model development. International Journal of Industrial Ergonomics. 1998;22:449–472.

7. Herman IP. Physics of the human body. New York (NY): Springer-Verlag Berlin Heidelberg; 2007. p. 16–17.

8. Ciarlet PG. Handbook of numerical analysis, volume 12: Computational models for the human body: special volume. Amsterdam (Netherlands): Elsevier; 2004. p. 392.

9. Manseau J, Keown M. Development of an assessment methodology for lower leg injuries resulting from anti-vehicular blast landmines. In: Gilchrist MD, editor. IUTAM symposium on impact biomechanics: from fundamental insights to applications. Dordrecht (The Netherlands): Springer; 2005. p. 33–40.

10. Cikajlo I, Matjačić Z. The influence of boot stiffness on gait kinematics and kinetics during stance phase. Ergonomics. 2007;50(12):2171–2182.

11. Yoo JH, Murugan M, Le D. Development of a lumped-parameter occupant injury assessment model for vehicular blast effects simulation. Proceedings of the ASME 2012 Conference on Smart Materials, Adaptive Structures and Intelligent Systems; 2012 Sep 19–21; Stone Mountain, GA.

12. Liang C-C, Chiang C-F. A study on biodynamic models of seated human subjects exposed to vertical vibration. International Journal of Industrial Ergonomics. 2006;36:869–890.

13. Wu X, Griffin MJ. A semi-active control policy to reduce the occurrence and severity of end-stop impacts in a suspension seat with an electrorheological fluid damper. Journal of Sound and Vibration. 1997;203(5):781–793.

14. Chaudhuri A, Yoo JH, Wereley NM. Design, test and model of a hybrid magnetostrictive hydraulic actuator. Smart Materials and Structures. 2009;18(8):1–21.

15. MIL-STD-704F. Aircraft electric power characteristics. Lakehurst (NJ): Naval Air Systems Command. 2004 Mar 12.

16. Richards M, Podob R. Development of an advanced energy absorber. Presented at: 35th Annual SAFE Symposium, 1997 Sep 8–10; Phoenix, AZ.

INTENTIONALLY LEFT BLANK.

Appendix A. Test Plan

A.1 Test Objectives

The objective of this program is to demonstrate an integrated adaptive energy attenuation system utilizing a novel fail-safe magnetorheological energy absorber (FSMREA) for rotorcraft seats. By using electronically controllable magnetorheological (MR) fluid and onboard control electronics, the FSMREA will automatically adapt to occupant weight and crash severity to minimize occupant injury. The purpose of this research and development program is to demonstrate FSMREAs for enhanced crash protection using a modified helicopter crew seat ("test seat") as a test bed.

A series of high-speed horizontal sled tests simulating pure vertical crash loading will be conducted using the test seat with the integrated FSMREA system. The objective of the high-speed testing is to demonstrate and assess energy attenuation performance of the FSMREA for varying high-impact velocity conditions and occupant weights.

A.2 Test Article

InnoVital Systems, Inc., will provide an FSMREA-equipped test seat and representative seat attachment hardware to the test facility. The test facility will provide anthropomorphic test devices (ATDs), gear (boots and helmet) to be worn by the ATD, as well as the horizontal sled test system, associated fixtures, and all instrumentation and data acquisition equipment. InnoVital will provide a spare FSMREA and spare parts for high-speed testing in case parts should fail during one of the test conditions.

A.2.1 FSMREA and Gearing System

The FSMREA Joint Aircraft Survivability Program (JASP) test seat system consists of 2 assemblies: the FSMREA and the rotary-to-linear gearing assembly. The FSMREA is attached to the gearing assembly by inserting the pinion into the center of the gearing assembly while simultaneously meshing the gear teeth and seating the auxiliary gear shafts and 2 support pins in their corresponding journal bearings and support holes, respectively, and securing 4 large hex head shoulder bolts and 4 smaller hex bolts (Figs. A-1 and A-2). The FSMREA is connected to the fixed seat base via the lateral mounting fixtures. The gear rack is connected to the vertically stroking seat by the upper and lower mounting fixtures. As the seat strokes vertically, the rack's motion turns the pinion shaft and rotates the shearing surfaces within the FSMREA. The fully integrated test seat is shown in Fig. A-3.

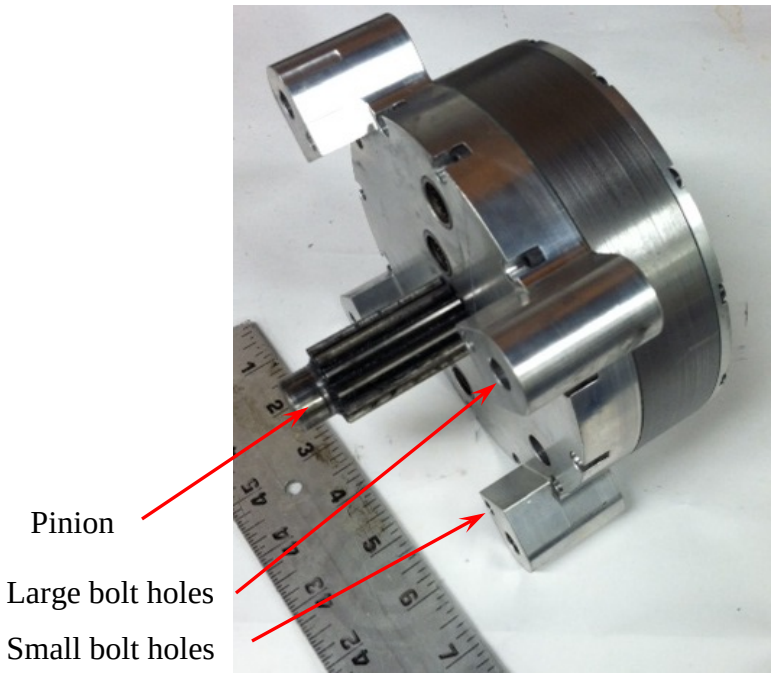

Fig. A-1 FSMREA with integrated pinion

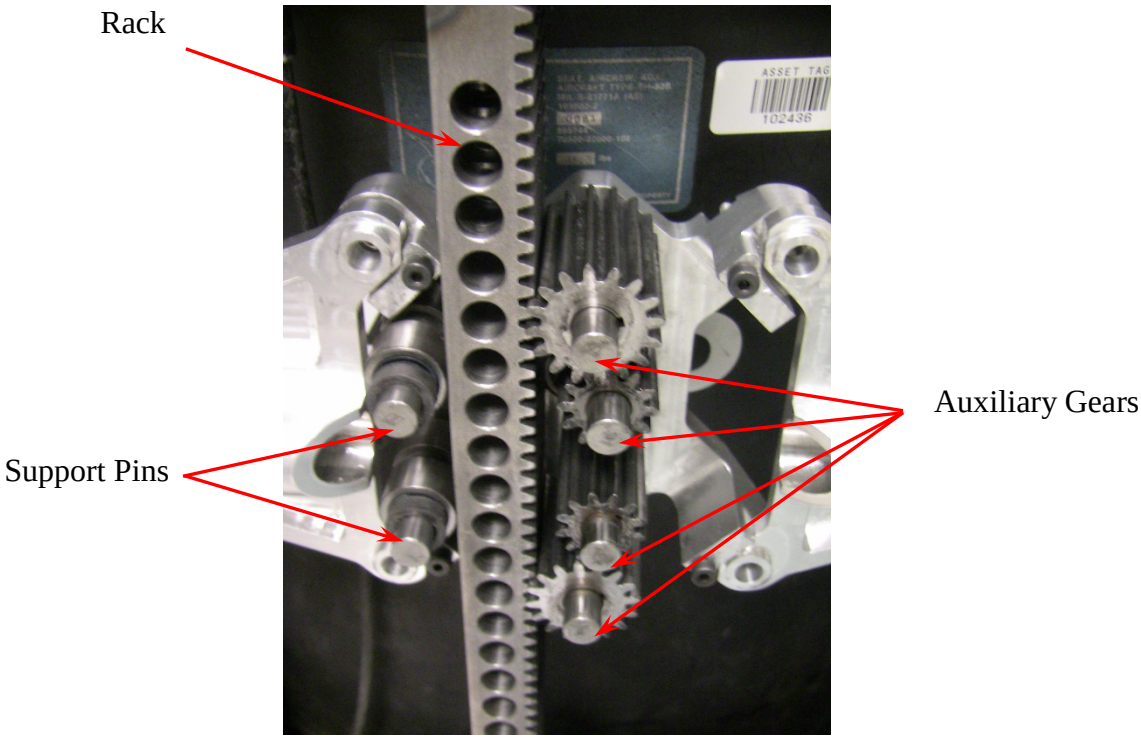

Fig. A-2 Linear-to-rotary gearing assembly

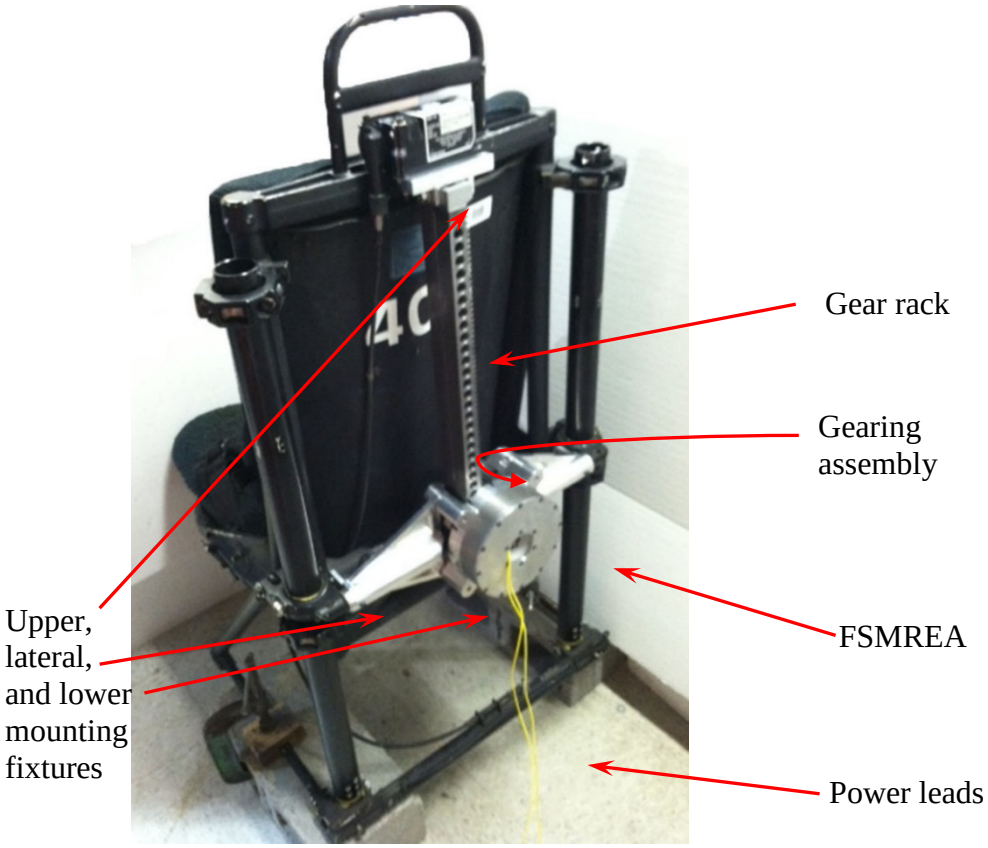

Fig. A-3 JASP seat configuration

A.2.2 Integrated Control Electronics

A single integrated control electronics unit has been developed for the FSMREA to provide stand-alone control. This electronics hardware is composed of 2 main components: the main controller board and the secondary DC-to-DC converter board. The main controller board encompasses a microprocessor, micromechanical systems accelerometers, and power conditioning circuitry, as well as an input for acquiring data from a linear positioning system and/or load cell, as required. The main component of the secondary board is the DC-DC converter, which helps bring down the high-input voltage supplied to the power conditioning circuitry to supply power to the low-voltage circuit electronics. The fully assembled control electronics hardware to be installed on the test seat is shown in Fig. A-4. The test seat will be delivered with the electronics hardware unit installed.

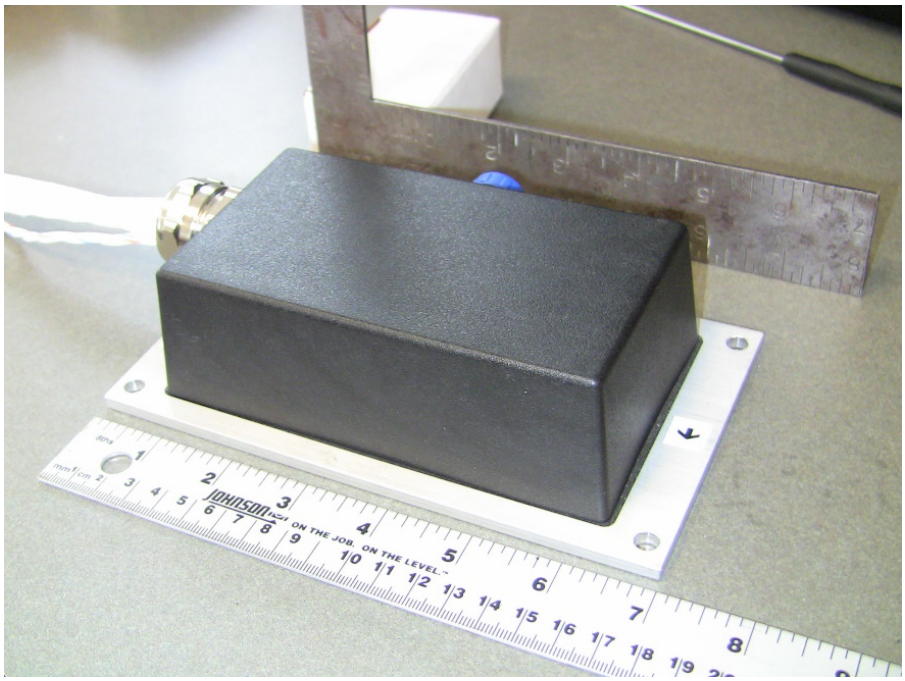

Fig. A-4 FSMREA control electronics box

A.3 Dynamic Testing

In this effort, pure vertical axis seat tests will be conducted using the high-speed horizontal sled at the test facility. This testing will be performed to validate the added benefits of the FSMREA system in minimizing occupant injury during a crash event. In this testing, the test seat with integrated FSMREA shall be evaluated for its ability to automatically adapt to occupant weight and crash severity to minimize occupant injury. Human tolerance criteria for the test seat configured with the FSMREA will be compared with that of the test seat configured with the baseline energy absorber (EA) as well as published data.

Among the human tolerance criteria that are used to evaluate the performance of the FSMREA system will be whole body acceleration (measured at the seat pan), pelvic vertical accelerations, lumbar compressive loads, chest accelerations, head acceleration, and upper-neck forces and moments. Data gathered will be used to support the calculation of probability of injury indexes such as Neck Injury Criteria (Nij), and Head Injury Criteria (HIC).

The test seat will be attached to the test sled by means of the T-rail tracks and U-brackets shown in Fig. A-5. Details and drawings of these fixtures are shown in Appendix B.

Fig. A-5 Seat attachment to mounting tracks

A.3.1 Sensor and Data Acquisition System

The JASP test seat integrated with FSMREA will be installed onto the horizontal sled testing equipment at test facility. To record accelerations of interest, triaxial accelerometers will be mounted to the base of the sled to record input motion, the underside seat pan at the buttock reference point (BRP) per the Aircraft Crash Survival Design Guide,[1] as well as to the pelvis, chest, and head of the ATD (Fig. A-6). Accelerometers shall be hard-mounted to the surface of interest such that there are no secondary dynamics associated with mounting condition (i.e., no double-sided tape). In addition to this, the Aerospace Hybrid-III ATD will be outfitted with both a 6-axis upper neck load cell (for measuring Nij criteria) as well as a lumbar load cell. Appendix C summarizes the data channels, type of data, and their respective axis of measurements that are recorded to evaluate the injury assessment criterion. If available, restraint tensiometers shall be incorporated nearest to the seat attachment point as possible to measure restraint loading. In addition, high-speed video shall be provided showing both the rear and side views of the seat.

[1] Johnson NB, Robertson SH. Crash survival design guide TR 71-22, volume V, aircraft postcrash survival. Fort Eustis (VA): Army Applied Technology Laboratory (US); 1980 Jan. Report No.: USARTL-TR-79-22E.

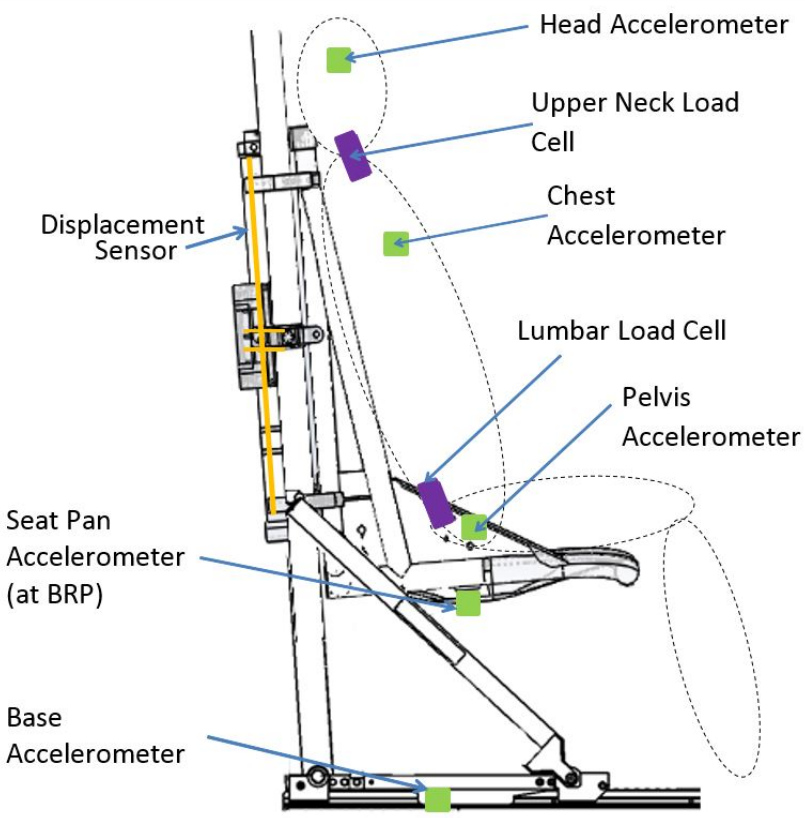

Fig. A-6 High-speed testing sensor configuration

Particularly for the seat pan accelerometer mounting, the accelerometer needs to be mounted at the BRP, which is 5.5 inches forward of the neutral seat reference point **(**NSRP) (see definitions in the following bullets). Additionally, the seat pan accelerometer shall be mounted such that the accelerometer's coordinate system is aligned with the seat coordinate system (i.e., flat with respect to base frame).

- Seat reference point (SRP): The seat reference point is the intersection of the seat back tangent line and the seat bottom tangent line.
- Neutral seat reference point (NSRP): The neutral seat reference point is the seat reference point with the seat in the nominal midposition of the seat adjustment range. This seat position will place the 50th percentile (seated height) man with his eye in the design eye position.
- Buttock reference point (BRP): The buttock reference point is the most forward limit of the bottom tangent line and represents the body pressure points located 5.5 inches forward of the seat reference point. This represents the area of the lowest seat cushion compression under a static vertical load of 1 g's.

Test instrumentation shall meet SAEJ211[2] conformance. The following information shall be provided by the sled testing facility.

- Type/model of transducer, calibration sheet, and transducer datasheet
- Methods of attaching sensors
- Data rates

All sensor data will be recorded and filtered in accordance with a SAEJ211/1 instrumentation system. Data will be provided in tabular and plotted format. At least 2 high-speed color imagers will also be used to visually capture the sled tests. Pre- and posttest still images will be provided for each test.

A.3.2 Dynamic Crash Sled Testing

Dynamic testing shall be performed to validate the vertical energy absorption performance of the seat with the FSMREA system installed. The tests are intended to demonstrate the system's ability to adapt to a range of occupant weights and crash severities, with occupants ranging from 5th percentile female to 95th percentile male and crash sink rates ranging from 21 to 42 ft/s. Figure A-7 shows the seat test orientation and the definition of test pulse parameters. Table A-1 contains the recommended test matrix. These dynamic tests will utilize a 50th percentile aerospace Hybrid-III ATD with straight spine, a 95th percentile aerospace Hybrid-III ATD, and either a 5th percentile female aerospace Hybrid-III ATD or a 50th percentile aerospace Hybrid-III with both arms removed at the shoulder joints to simulate a 5th percentile dummy weight per MIL-S-58095A[3] Section 4.7.4. See Appendix D for required total ATD weights. In Table A-1, tests 1–3 are intended to show adaptability to crash sink rate (dV), while maintaining pulse durations consistent with MIL-STD-58095A. The intention is that the FSMREA will further reduce or eliminate spinal injury risk in lower impact energy conditions versus conventional EAs. Test 1 and test 2 are representative of one-quarter and one-half the impact energy of MIL-STD-58095A, respectively, while test 3 represents full MIL-STD-58095A vertical impact energy. Tests 4 and 5 show that the FSMREA has the capability to minimize effective limit load for a range of occupants, from the ungeared 5th female to the geared 95th male—both to full MIL-STD-58095A vertical impact conditions. Tests 6–10 repeat tests 1–5, but with the seat in its baseline EA configuration.

[2] SAE J211/1. Instrumentation for impact test, part 1, electronic instrumentation. Warrendale (PA): Society of Automotive Engineers, Inc. 2007 May 4.

[3] MIL-S-58095A. Seat system: crash-resistant, non-ejection, aircrew, general specification for. Washington (DC): Army Aviation Systems Command (US);1986 Jan 31.

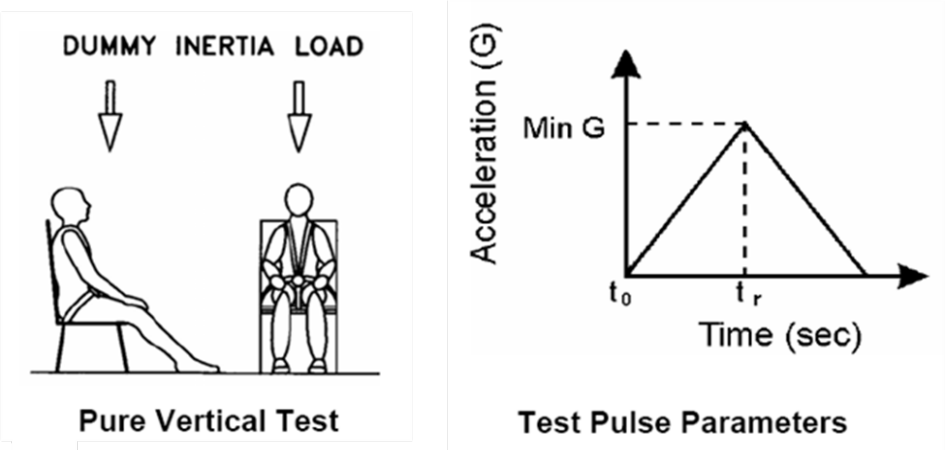

Fig. A-7 Dynamic test parameters

Table A-1 Dynamic test matrix and requirements

Test no.	EA configuration	ATD	Test pulse requirement				
			t_{rmin} (s)	t_{rmax} (s)	G_{min} (g's)	G_{max} (g's)	dV_{min} (ft/s)
1	FSMREA	50th Male	0.036	0.051	18	25	21
2		50th Male			38	42	34
3		50th Male			46	51	42
4		5th Female			46	51	42
5		95th Male			46	51	42
6	Baseline	50th Male			18	25	21
7		50th Male			38	42	34
8		50th Male			46	51	42
9		5th Female			46	51	42
10		95th Male			46	51	42

These sled tests will be performed using the Sled Test Checklist (Appendix E) provided by InnoVital.

The following test conditions shall apply to dynamic testing:

- The initial seat height adjustment shall be set in the mid-position for all tests per MIL-S-58095A[3].
- For all tests, the ATD's feet shall be secured in a representative anti-torque pedal position (MIL-S-58095A). The heels will be placed approximately 21 inches forward of the forward seat mounting location and at floor level for the 50th male ATD. The resulting shin angle for the 50th male ATD will be measured, and approximately this same shin angle will be maintained throughout the dynamic test for all ATDs by adjusting the heel distance accordingly. Both left and right upper arms shall run parallel to the sides of the upper torso, while the lower arms, bent at the elbow, shall rest on top of the upper leg.

- Static compression of the FSMREA system and seat cushions shall be simulated by cinching straps or bands over the lap of the ATD.

The following criteria must be met to render the dynamic test acceptable:

- Test dynamic pulse is to be evaluated to the criteria defined in TR 71-22[1]. Any test with an input crash pulse that does not conform to Table A-1 will be considered a "no-test". The crash pulse data shall include peak deceleration in g's, pulse duration, pulse rise time, and impact velocity, and will be validated per Fig. A-7 and Table A-1. Appendix F details a crash pulse validation table that compares pulse requirements to actual measured values for all tests.
- Ensure all instrumentation data was captured per Appendix C; otherwise, it will be considered a "no-test".

The following parameters shall be compared with recommended levels, EA configurations, and values presented in Richards and Podob[4]:

- Dynamic test per MIL-S-058095A[3]: The seat pan acceleration measured shall not exceed 23 g's for more than 0.025 s, when measured in accordance with a SAEJ211/1,[2] Class 60 instrumentation system. The time duration shall be additive, in a cumulative manner, for all acceleration excursions exceeding 23 g's.
- Lumbar load limits: The peak spinal compression load, when measured in accordance with a SAEJ211/1 Class 60 instrumentation system, shall be compared to Full Spectrum Crashworthiness Criteria Program recommended loads of 933, 1,395, and 1,757 lb for the 5th percentile female, and 50th and 95th percentile male aerospace Hybrid III ATD, respectively.
- Nij criteria per Full Spectrum Crashworthiness guidelines: The resulting Nij as calculated from recorded data shall be compared with the tolerance threshold recommended value of 0.5.

The testing is expected to be completed within 1 week from the start of testing. After completion of the test, a detailed test report will be prepared and submitted to InnoVital Systems, Inc., for review.

[4] Richards M, Podob R. Development of an advanced energy absorber. Presented at: 35th Annual SAFE Symposium, 1997 Sep 8–10; Phoenix, AZ.

A.4 Summary

This test plan has been developed for the purposes of testing and evaluating the performance of the FSMREA system in mitigating occupant injury for varying occupant mass and crash severity. This tactical FSMREA system is integrated into the JASP test seat, and crash performance will be evaluated to ensure that the system integration and control algorithm are working properly.

A.5 References

The references used in the body of this document take precedence in the event of a conflict between text of this document and the cited references. All references to "the contractor" shall refer to the FSMREA manufacturer/supplier, InnoVital Systems, Inc.

INTENTIONALLY LEFT BLANK.

Appendix B. Floor Mounting Detail

This appendix appears in its original form, without editorial change.

Approved for public release; distribution is unlimited.

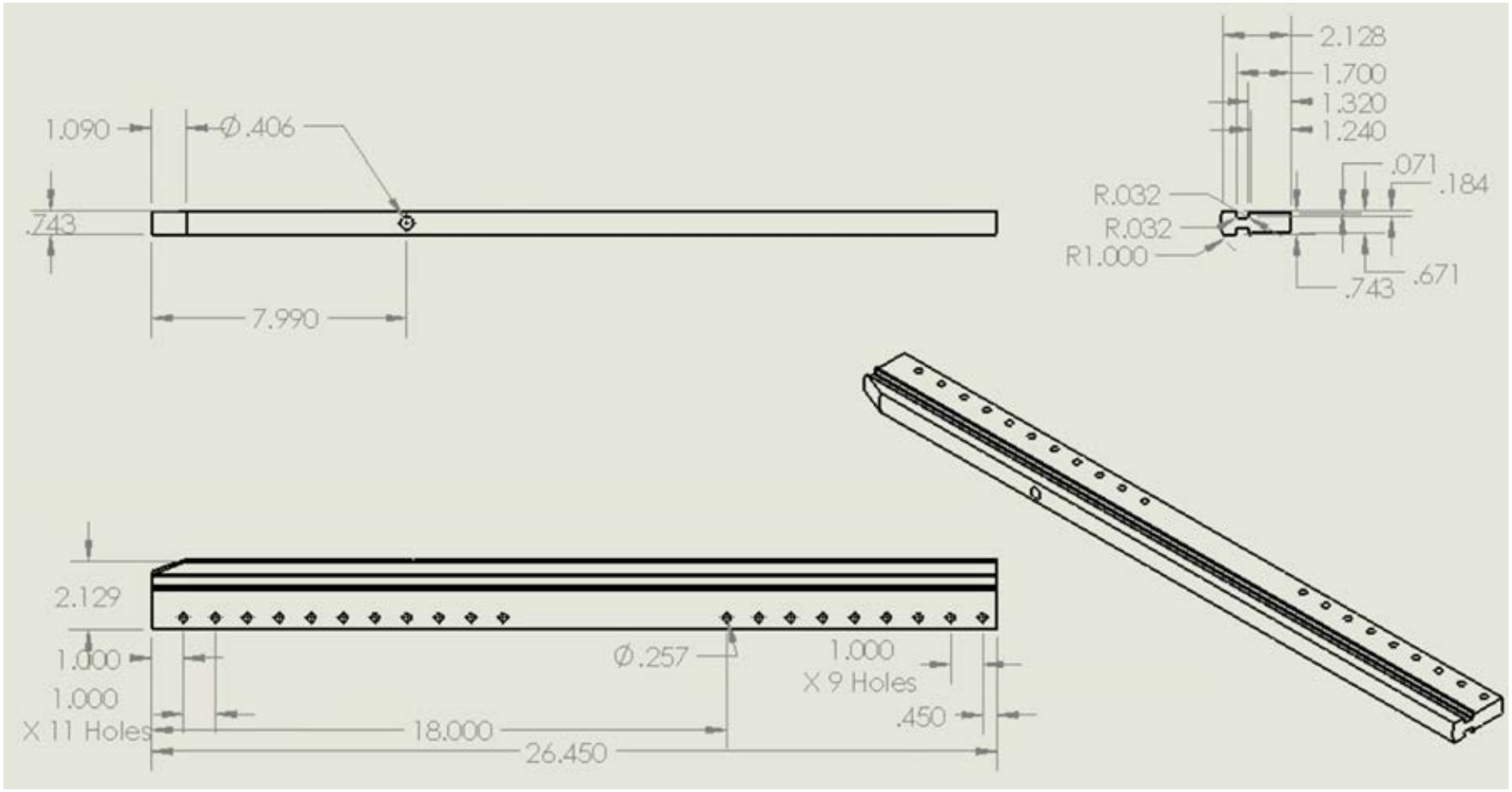

Fig. B-1 T-rail tracks (units in inches): Quantity 2

Approved for public release; distribution is unlimited.

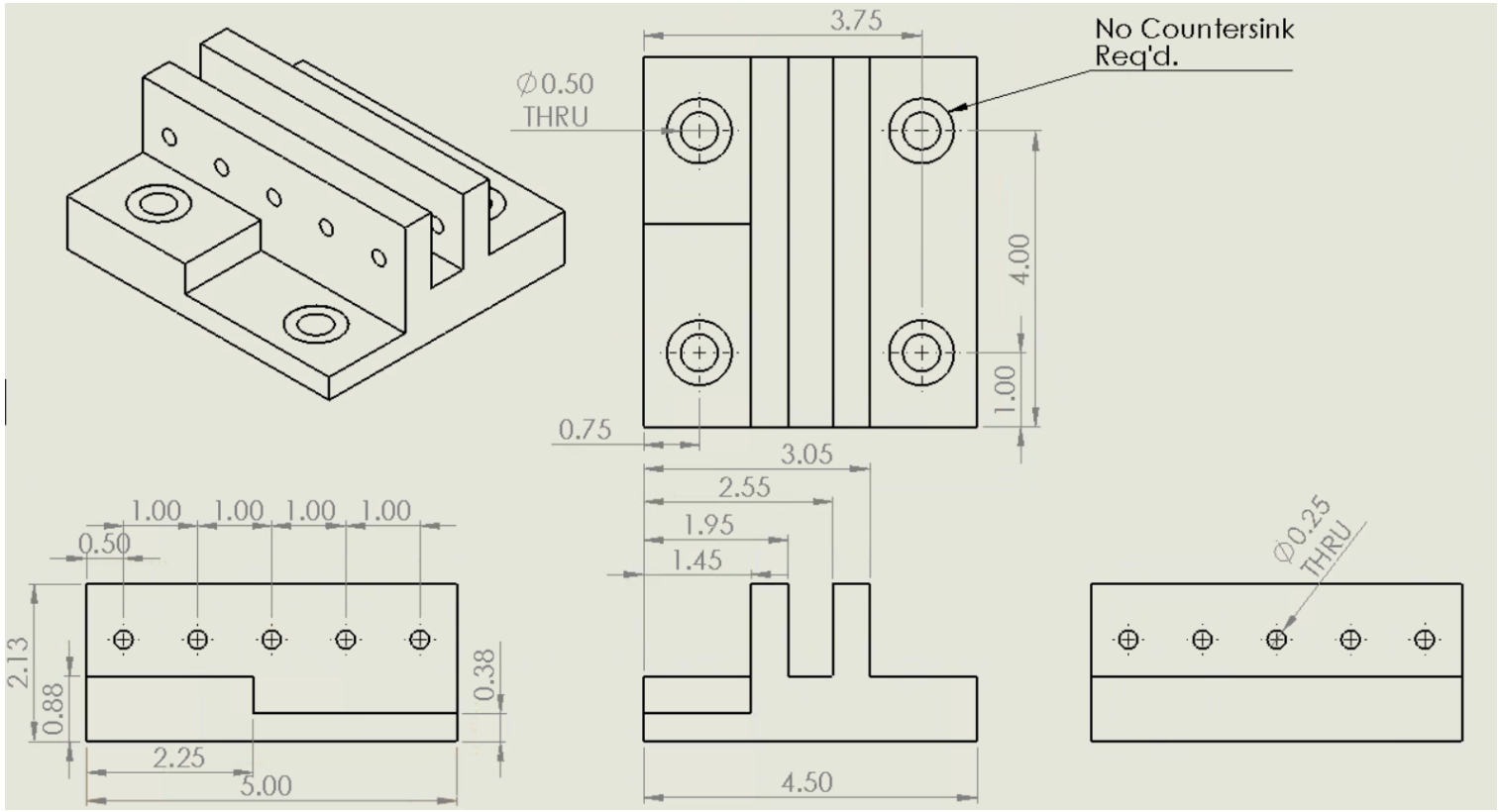

Fig. B-2 U-brackets (units in inches): Quantity 4

INTENTIONALLY LEFT BLANK.

Appendix C. Sensor, Data Type, and Corresponding Injury Assessment Criteria

This appendix appears in its original form, without editorial change.

Approved for public release; distribution is unlimited.

Appendix C. Sensor, Data Type and Corresponding Injury Assessment Criteria

Channel No.	Sensor type	Direction	Location	Data type	Criteria & Reference
1	Tri-axial accelerometer	X	Base	Acceleration	for information only
2		Y			for information only
3		Z			MIL-S-58095A
4	Tri-axial accelerometer	X	seat pan at BRP	Acceleration	for information only
5		Y			for information only
6		Z			not greater than 23G for more than 25ms per MIL-S-58095A
7	Accelerometer	Z	seat pan at BRP	Acceleration (backup)	not greater than 23G for more than 25ms per MIL-S-58095A
8	Spring Potentiometer	Z	floor to seat pan	Displacement	for information only
9	Tri-axial accelerometer	X	ATD Pelvis	Acceleration	for information only
10		Z			for information only
11	Tri-axial accelerometer	X	ATD Chest	Acceleration	resultant not greater than 60G for more than 3 ms per FMVSS 208
12		Z			
13	6-axis load cell	X	Lumbar	Force & Moment	for information only
14		Y			for information only
15		Z			933 lb, 1,395 lb, & 1,757 lb, respectively for 5th, 50th, & 95th ATD per recommendations from Full Spectrum Crashworthiness Criteria Program
16		Mx			for information only
17		My			for information only
18	6-axis load cell	X	Upper neck	Force & Moment	Nij < 0.5 per FSC Guidelines
19		Z			
20		MY			
21	Tri-axial accelerometer	X	Head	Acceleration	HIC_{15} < 700 per FSC Guidelines
22		Y			
23		Z			
24	High-Speed Video	n/a	Rear View	Video	for information only
25	High-Speed Video	n/a	Side View	Video	for information only

Appendix D. Anthropomorphic Test Device Total Weight Requirements

This appendix appears in its original form, without editorial change.

ATD	Gear	Total Weight with Gear (lb)
5th Female	Boots & Helmet	111
50th Male	Boots & Helmet	179
95th Male	Boots & Helmet	228

Appendix E. High-Speed Sled Test Checklist

This appendix appears in its original form, without editorial change.

Date: _____ **Test Number:**_____

Test Engineer: _____

Test Description: _____

PRE-TEST CHECKLIST

1. ATD / Instrumentation
   - ☐ A. Record ATD size: _____/ nude weight:_____
   - ☐ B. Record ATD serial number: _____
   - ☐ C. ATD and instrumentation build up complete
   - ☐ D. Confirm sign conventions on instrumentation

2. ATD
   - ☐ A. ATD flight gear recorded in Table E1
   - ☐ B. Total ATD weight with gear matches requirements of Appendix D.

Table E1: Flight Gear

Flight Gear Description	Type	Size / Weight
Boots		
Flight Suit		
Helmet		
Vest		

3. Installation
   - ☐ A. Version ____, total seat weight:_____
   - ☐ B. Test Seat installed on text fixture
   - ☐ C. Seat height adjusted to proper position
   - ☐ D. All bolts, seat adjustment lockpins, and connecting hardware is tight and secure
   - ☐ E. ATD is seated in the Test Seat in full aft position with buttocks back against seat back.

4. ATD / Instrumentation
   - ☐ A. ATD lap belts fastened and tightened, safety strap is secured. Adjust lap belt tension so that the belt is snug on the ATD but two fingers may still be inserted between the ATD and the belt.
   - ☐ B. ATD shoulder restraints fastened and tightened.
   - ☐ C. Set restraint inertia reel to auto-lock mode.
   - ☐ D. Mark the initial location of the restraint with a grease pencil to ensure any slippage that may occur during the test can be measured.
   - ☐ E. ATD hands unrestrained with both left and right upper arms running parallel to the sides of the upper torso, while the lower arms, bent at the elbow, shall rest on top of the upper leg.
   - ☐ F. Static compression of the Test Seat and seat cushions by cinching straps over the lap of the ATD.
   - ☐ G. ATD legs unrestrained in representative antitorque pedal positions spaced from seat per test plan shown in Section A.3.2 of Appendix A.
   - ☐ H. Record shin angle_____ and heel-to-seat distance _____
   - ☐ I. Position ATD knees with approximately 4 inches of space between them.
   - ☐ J. Targets properly positioned on seat, test fixture, and ATD
   - ☐ K. Install the linear transducers to measure the bucket stroke parallel to the guide tubes.

☐ L. Check the operation of the high speed video cameras and lighting.
☐ M. Confirm instrumentation per Appendix C is turned on to record, including high speed video
☐ N. Instrumentation checked out
☐ O. Inspect all exposed instrumentation cabling to ensure no damage will occur during sled test
☐ P. Make sure all orientations and polarities are correct for the ATD and the test article.
☐ Q. Make sure ATD is snugly fixed in seat.

Date: _____ **Test Number:**_____

Test Engineer: _____

Test Description: _____

5. Test Article Inspection

☐ A. Ensure pre-test photos are taken per table E2

At a minimum the following will be photographed: Overall photos of the position of installed seat and seated occupant showing the position on the fixture and occupant positioning.

Table E2: Photograph List

Focus				**Angle**
Test Fixture Setup	Seat Pan Orientation G_{xy} w/ ATD	Torso	Test Article	Straight on
Test Fixture Setup	Seat Pan Orientation G_{xy} w/ ATD	Torso	Test Article	45 deg left
Test Fixture Setup	Seat Pan Orientation G_{xy} w/ ATD	Torso	Test Article	90 deg right
Test Fixture Setup	Seat Pan Orientation G_{xy} w/ ATD	Torso	Test Article	45 deg right
Test Fixture Setup	Seat Pan Orientation G_{xy} w/ ATD	Torso	Test Article	90 deg left

6. Ready to test

☐ A. Conduct test per test sequence identified in **Error! Reference source not found.**. Test condition no.:_____

☐ B. Test Engineer _____
Signature

☐ C. InnoVital Engineer _____
Signature

Date: _____ **Test Number:**_____

Test Engineer: _____

Test Description: _____

POST-TEST CHECKLIST

1. Test Article Inspection
   ☐ A. Ensure post-test photos are taken per Table E2 in addition to any noted failures or anomalies:
   ☐ B. Record notable damages and failures: _____
   ☐ C. Record restraint slippage: L:_____R:_____

2. Data
   ☐ A. Ensure all instrumentation data captured per Appendix C
   ☐ B. Complete crash pulse validation table of Appendix F. If t_r, G_{peak}, & dV not within requirements of Appendix F, "no test" will be determined and will must be repeated.
   ☐ C. Record key peak values in Table E3 for quick evaluation before each next test and identify any other notable values_____

Table E3: Key Peak Values

Channel No.	Sensor type	Direction	Location	Peak Values
3	Accelerometer	Z	Base	
6	Accelerometer	Z	Seat Pan	
11	Accelerometer	Resultant	Chest	
16	Load Cell	Z	Lumbar	

6. Acceptable Test
   ☐ A. Test Engineer _____ Signature

   ☐ B. InnoVital Engineer _____ Signature

Appendix F. Crash Pulse Validation Table

Test no.	Occupant weight	Test pulse data			Test pulse requirement				
		t_r (s)	G_{peak} (g's)	dV (ft/s)	t_{rmin} (s)	t_{rmax} (s)	G_{min} (g's)	G_{max} (g's)	dV_{min} (ft/s)
1	50th Male	. . .	. . .	. . .	0.036	0.051	18	25	21
2	50th Male	. . .	. . .	. . .	0.036	0.051	38	42	34
3	50th Male	. . .	. . .	. . .	0.036	0.051	46	51	42
5	5th Female	. . .	. . .	. . .	0.036	0.051	46	51	42
6	95th Male	. . .	. . .	. . .	0.036	0.051	46	51	42

Approved for public release; distribution is unlimited.

List of Symbols, Abbreviations, and Acronyms

AATD	US Army Aviation Applied Technology Directorate
ARL	US Army Research Laboratory
ASEA	adaptive seat energy absorber
ATD	anthropomorphic test device
BRP	buttock reference point
DC	direct current
DPM	driving-point mechanical
EA	energy absorber
FEM	finite element method
FSMREA	fail-safe magnetorheological energy absorber
FY	fiscal year
HA	Horizontal Accelerator
HIC	head injury criteria
IARV	injury assessment reference value
ID	inner diameter
IM	impedance
JASP	Joint Aircraft Survivability Program
JASPO	Joint Aircraft Survivability Program Office
MFEA	magnetostrictive friction energy absorber
MR	magnetorheological
MREA	magnetorheological energy absorber
MS	magnetostrictive
NAWCAD	Naval Air Warfare Center Aircraft Division
Nij	neck injury criteria
NSRP	neutral seat reference point

OEM	original equipment manufacturer
PCD	printed circuit board
PWM	pulse-width modulation
SDOF	single-degree-of-freedom
SLAD	Survivability/Lethality Analysis Directorate
SOW	statement of work
SRP	seat reference point
STH	seat-to-head
TR	transmissibility
VTD	Vehicle Technology Directorate

1 (PDF) DEFENSE TECHNICAL INFORMATION CTR DTIC OCA

2 (PDF) DIRECTOR US ARMY RESEARCH LAB RDRL CIO L IMAL HRA MAIL & RECORDS MGMT

1 (PDF) GOVT PRINTG OFC A MALHOTRA

1 (PDF) JASP OFFICE CAPT K BRANHAM

1 (PDF) INNOVITALSYSTEMS G HIEMENZ

1 (PDF) UNIVERSITY OF MARYLAND, COLLEGE PARK N M WERELEY

4 (PDF) DIR USARL RDRL VT LTC K MORGAN RDRL VTM J YOO DY LE RDRL VTP M MURUGAN

INTENTIONALLY LEFT BLANK.